Electrical Properties of Self-assembled Metal-Molecular Networks: Modelling, Experiment and Applications

by

Eberechukwu Victoria Amadi
B. Sc., Covenant University, 2016

A Thesis Submitted in Partial Fulfillment
of the Requirements for the Degree of

MASTER OF APPLIED SCIENCE

in the Department of Electrical and Computer Engineering

Supervisory Committee

Electrical Properties of Self-assembled Metal-Molecular Networks: Modelling, Experiment and Applications

by

Eberechukwu Victoria Amadi
B. Sc., Covenant University, 2016

Supervisory Committee

Dr. Chris Papadopoulos, (Department of Electrical and Computer Engineering)
Supervisor

Dr. Alexandre Brolo, (Department of Chemistry)
Outside Member

Abstract

Supervisory Committee

Dr. Chris Papadopoulos, (Department of Electrical and Computer Engineering)
Supervisor

Dr. Alexandre Brolo, (Department of Chemistry)
Outside Member

Complementing electronic components with molecular analogs is a promising alternative to further miniaturization of conventional silicon electronic devices in the quest to achieve functional molecular nanoscale circuit elements. To this end, molecular units have been widely investigated to evaluate their suitability for future nanoelectronic circuit applications. Previous work has typically either focused on tightly packed layers of dithiol molecule-encapsulated gold nanoparticles or small oligomeric structures comprised of nanoparticles linked by a few dithiol molecules. In this thesis, we study the electrical and electronic properties of metal-molecular networks having an intermediate number of dithiol molecules both theoretically and experimentally.

Electronic transport through self-assembled networks with tunable thiol molecule: gold nanoparticle ratios (ranging from 1:1 to 50:1) is studied using two-terminal electrical characterization techniques. The tunability of the electrical properties (e.g., resistance, current etc.) of the molecular networks on modifying the thiol molecule: gold nanoparticle ratios and/or type of molecule used was observed. Specifically, the current in the molecular networks studied typically decreased with increasing molecule: AuNP. For example, in gold-benzenedithiol molecular networks with approximately the same length-to-width ratios, current at low bias, 0.3 V, was found to decrease from the μA range in 1:1 ratio

samples to the nA range in 50:1 samples. Additionally, many gold-benzenedithiol molecular networks which had linear *I-V* characteristics at low biases displayed nonlinearities in their *I-V*s at higher biases. In such cases, the nonlinearities in the *I-V*s at higher biases became more pronounced with increasing molecule: AuNP ratio. For example, in a control sample, consisting of only gold nanoparticles, linear *I-V* behaviour was observed, while the 50:1 gold-benzenedithiol molecular network displayed NDR with a measured peak-to-valley ratio of approximately 1.52. A linear resistor circuit model provided accurate approximations of the low bias *I-V* behaviour of the molecular networks.

Experimental studies were complemented with first principles density functional theory-based simulations of the molecular networks. Linear chains and branched networks of interconnected benzenedithiol molecules and Au_6 clusters were the systems of interest in this study. Calculated current-voltage characteristics of the metal-molecular networks exhibited nonlinearities and rectification with negative differential resistance (NDR) peaks that became more pronounced with increasing chain length of the linear chains. Peak-to-valley current NDR ratios as large as ~ 500 and rectification ratios of ~ 10 (0.25 V) were shown for linear and branched circuit elements, respectively, illustrating how charge transport through molecular-scale devices could be controlled with precision by modifying the structure and geometry of molecule-nanoparticle networks. Observed nonlinearities (e.g., NDR, hysteresis, and rectification) in the *I-V*s of the self-assembled metal-molecular networks studied highlight their potential for application as circuit elements in future nanoelectronic devices and circuits, including memory, logic, switching and sensing. Additionally, the device level physical randomness and imperfections induced during fabrication of the metal-molecular networks, as well as the variability of the resistance of

the networks on modifying the molecule: gold nanoparticle ratios can be applied for generating random binary sequences.

Table of Contents

List of Tables

List of Figures

List of Abbreviations

Abbreviation	Meaning
AFM	Atomic force microscope
BDMT	Benzenedimethanethiol
BDT	Benzenedithiol
BOX	Buried oxide layer
CMOS	Complementary metal-oxide-semiconductor
CNT	Carbon nanotube
CNTFET	Carbon nanotube FET
CP-AFM	Conducting-probe AFM
CV	Cyclic voltammetry
DFT	Density-functional theory
DFT-NEGF	Density Functional Non-equilibrium Green's Function
DNP	Double numerical basis set with polarization
DOS	Density of states
DZP	Polarized double-zeta
FD-SOI	Fully-depleted silicon-on-insulator
FET	Field effect transistor
GAA	Gate-all-around
GAA-NWFET	Gate-All-Around nanowire field effect transistor
GGA	Generalized gradient approximation
HOMO	Highest occupied molecular *orbital*
HDT	Hexanedithiol
IC	Integrated circuit
IPA	Isopropyl alcohol
IRDS	International Roadmap for Devices and Systems
ITRS	International Technology Roadmap for Semiconductors
LB	Langmuir-Blodgett
LDA	Local density approximation
LDOS	Local density of states
LUMO	Lowest unoccupied molecular *orbital*

MBE	Molecular beam epitaxy
MCBJ	Mechanically controlled break junction
MO	Molecular orbital
MOSFET	Metallic oxide semiconductor field effect transistor
MPSH	Molecular projected self-consistent Hamiltonian
MWCNT	Multi-walled carbon nanotube
NDR	Negative differential resistance
NDT	Nonanedithiol
NEGF	Non-equilibrium green's function
NEM	Nano-Electro-Mechanical switch
NFGTM	Nano-floating gate transistor memory
NIST	National Institute of Standards and Technology
NW	Nanowire
NWFET	Nanowire field effect transistor
ODT	Octanedithiol
PBE	Perdew, Burke and Erzenhof
PDMS	Polydimethylsiloxane
PDOS	Projected density of states
PVR	Peak-to-valley ratio
RTD	Resonant tunneling diode
SAM	Self-assembled monolayer
SCE	Short channel effects
SCF	Self-consistent field method
SERS	Surface-enhanced Raman scattering
SET	Single electron transistor
SIESTA	Spanish Initiative for Electronic Simulations with Thousands of Atoms
SOI	Silicon-on-insulator
SPM	Scanning probe microscope
STM	Scanning tunneling microscope
SWCNT	Single-walled CNT
TDO	Thiopene dioxide
TEM	Transmission electron microscope
TFET	Tunnel field effect transistor
TTF-TCNQ	Tetrathiafulvalene-tetracyanoquinodimehtane
QM	Quantum mechanical

Acknowledgments

I would like to express my greatest gratitude to my supervisor, Dr. Chris Papadopoulos, for his guidance and support throughout my program of study. Without his tireless supervision and effort, my program would not have been as fulfilling and rewarding.

I am also thankful to Dr. Alexandre Brolo for the time and effort spent being a member of my supervisory committee and for providing valuable suggestions.

Special thanks to my friends and fellow researchers at the Nanoscale Research Laboratory: Anusha, Raju, and Tristan, for their help and support in the lab.

Finally, my deepest gratitude to my family for their constant support and encouragement during my graduate program.

Chapter 1 Introduction

1.1 Introduction to nanotechnology and nanoelectronics

"Nanotechnology" is a broad term encompassing processes and methods that lead to the fabrication, manipulation and characterization of structures, and materials with nanometer dimensions (1 to 100 nm). While the field of nanotechnology has seen tremendous growth in the last fifty years, functional nanostructures and nanomaterials have existed in biological systems for billions of years [1].

Several scientists have made attempts to explain phenomena related to nanosized materials. Robert Boyle, in a publication from 1661 [2], suggested that tiny particles of matter combine to form clusters which are not easily dissipated. Additionally, Michael Faraday, in 1857, published a paper where he attempted to explain the concept of optical scattering by metal particles in church windows [3]. Similarly, Gustav Mie, in 1908, provided an explanation for the dependence of the colour of stained glass on the metal size and type, but most notable among discussions related to nanomaterials was a lecture given by Richard Feynman in 1959 [4], in which he speculated on the potential of nanosized materials, and the possibility of etching lines few atoms wide using electrons.

In addition to the early theoretical studies, various experimental studies related to nanomaterials were conducted in the 1950s and 1960s. To name a few; alkali metal nanoparticles were fabricated by vaporizing metals and letting them condense on substrates, and two-dimensional quantum wells were made using bottom-up epitaxial growth techniques in the 1970s.

Although the field of nanotechnology experienced some progress in the 1950s and 1960s, a notable increase in research activity began in the 1980s with the invention of effective methods of fabricating and characterizing nanostructures. Specifically, the invention of electron beam lithography prompted unprecedented growth in the nanotechnology industry.

In contrast to the top-down lithographic methods of fabricating nanostructures, studies were made on fabricating nanostructures using bottom-up methods like self-assembly.

The 1980s also saw the invention of high-resolution microscopy techniques, which provided scientists with important tools for the effective characterisation and manipulation of nanostructures [1].

The history of electronics dates back to the invention of vacuum tubes by Thomas Edison in 1883. Vacuum tubes served as switches and amplifiers in early computers, however, they were impractical because of their size, weight, and high power consumption, and were rapidly phased out with the invention of the first point-contact transistor in 1947 [5] (Figure 1.1 (a)). The first junction transistor is shown in Figure 1.1 (b). Early transistors were made using germanium (Ge), however, the abundance and low cost of silicon (Si) as well as progress in silicon purification research, led to it becoming the preferred raw material for manufacturing electronic devices from the 1960s.

In the 1960s, computers comprised of thousands of transistors, and the need for compact lightweight systems, led to the invention of the integrated circuit (IC) independently by Jack Kilby in 1958 (Figure 1.1 (c)) and Robert Noyce in 1959 [1] (Figure 1.1 (d)). Kilby's IC was fabricated by connecting multiple components using gold wires on a silicon chip, while Noyce used vapor-deposited metal connections between various components.

Improvements in IC technology were catalyzed by the invention of metallic oxide semiconductor field effect transistors (MOSFETs) [6] and the microprocessor [5].

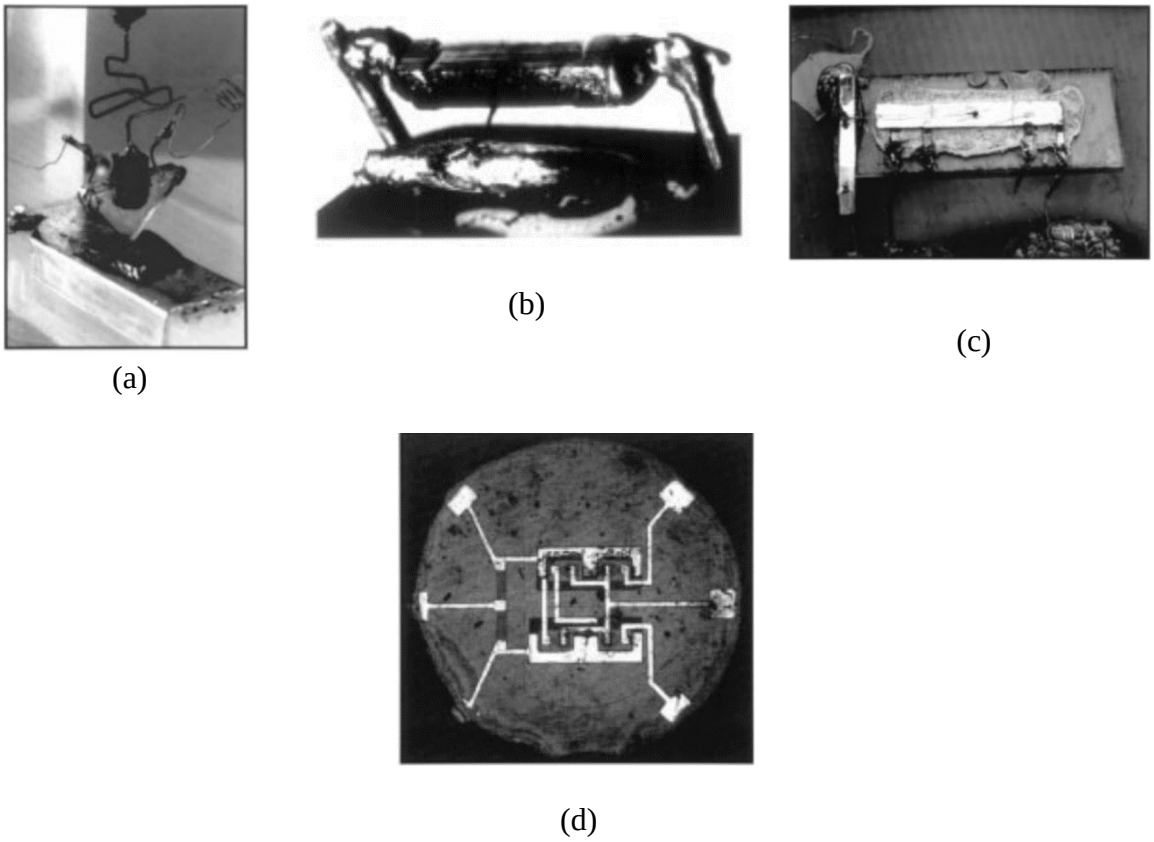

(a) (b) (c) (d)

Figure 1. 1 (a) The first point-contact transistor; (b) first junction transistor; (c) the first integrated circuit; (d) the first monolithic integrated circuit (adapted from Ref. 5).

MOSFET technology has evolved tremendously from the first MOSFET with a 25 μm-long channel fabricated in 1960 to the new generation MOSFETs with gate lengths less than 10 nm. This continued scaling down of the gate has made it possible to have ICs with millions of transistors and much improved circuit performances than earlier ICs.

With continued scaling of gate lengths and oxide thicknesses below 100 nm in MOSFETs on planar bulk silicon substrates, short channel effects (SCE) became more pronounced [7]. Hence, in order to improve the performance of scaled MOSFET devices on planar two-

dimensional bulk Si substrates, various strain techniques and the use of high-K hafnium dielectrics were employed in fabricating them. The transmission electron micrograph (TEM) of Intel's 45 nm MOSFET fabricated using strain techniques and high-K dielectrics is shown in Figure 1.2 [7].

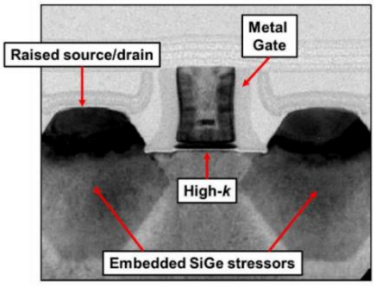

Figure 1. 2 Cross-sectional transmission electron micrograph of Intel's 45nm node p-channel MOSFET (adapted from Ref. 7).

Additionally, in order to reduce excessive SCE, advanced MOSFET structures with non-planar geometries were also implemented. The two main advanced MOSFET structures are the fully-depleted silicon-on-insulator (FD-SOI) MOSFETs and FinFETs [8].

The FD-SOI MOSFETs (Figure 1.3) are built directly on top of an oxide layer (SiO_2) and have fully depleted silicon channels (very thin Si films of about 8 nm thick), and a buried oxide layer (BOX) between the channel and the substrate, thereby leading to reduced leakage currents [8].

The 3-D FET or FinFET (Figure 1.3) is built either on silicon-on-insulator (SOI) or bulk silicon substrates by etching a narrow silicon stripe, with the gate electrodes straddling the sidewalls of the silicon stripe, and has an almost fully depleted body, which in turn leads to low leakage currents. Intel was the first to implement the tri-gate FET design in manufacturing 22 nm transistors (Figure 1.4) [9].

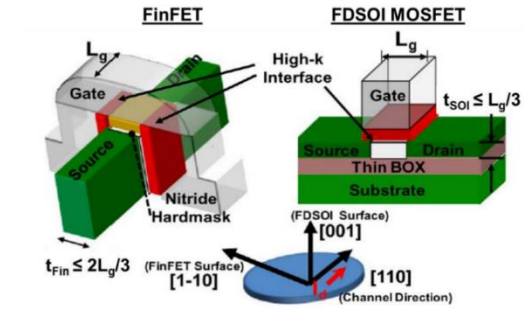

Figure 1. 3 Schematic view of the FinFET (left) and FDSOI MOSFET (right) (adapted from Ref. 8).

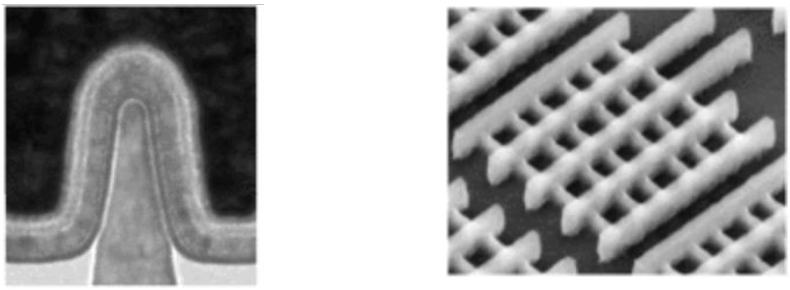

(a) (b)

Figure 1. 4 (a) Cross-sectional TEM image of 22 nm FET; (b) Tilted SEM of 22 nm tri-gate transistors (adapted from Ref. 9)

Since its advent in 1965, Moore's Law, which states that the component density and performance of integrated circuits will double every 18-24 months, has provided a useful roadmap for scaling down the sizes of MOSFETs (Figure 1.5) [10]. However, it is believed that Moore's law will no longer apply in the traditional sense beyond 2021, as gate lengths become less than 2 nm because of tunneling effects from source to drain, and resolution limits with conventional lithographic techniques [10], [11], [12].

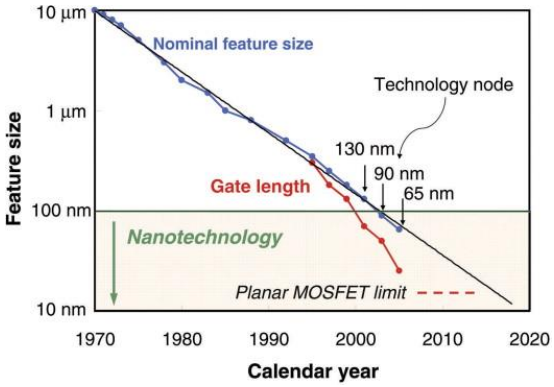

Figure 1. 5 Logic technology node and transistor gate length versus calendar year. (Published at the International Electron Devices Meeting.) (adapted from Ref. 10).

Additionally, the International Technology Roadmap for Semiconductors (ITRS), in one of its documents entitled, "Beyond CMOS", noted that Moore's law would not continue to apply to complementary metal-oxide-semiconductor (CMOS) silicon technology in the traditional sense of scaling down transistor gate lengths beyond 2021 [12]. Therefore, nanometer-scale alternatives (e.g. molecules and molecular units) to silicon nanoelectronics would be required to continue the trend of miniaturization of electronic components to a few nm or less with minimal short channel effects. Nanoelectronic devices such as Carbon Nanotube FETs (CNTFETs), Nano-Electro-Mechanical switches (NEMS), nanowire FETs (NWFETs) and single electron transistors, were recommended as the next generation of electronic devices for circuit applications [12].

The notion of finding alternatives or complementing conventional silicon nanoelectronics with different device architectures and materials was reiterated in the newer electronic devices roadmap (International Roadmap for Devices and Systems (IRDS)) [13]. In the "More Moore" document released as part of the 2020 IRDS Report, a transition to newer device architectures like Gate-All-Around transistors using nanowires (GAA-NWFETs) and 3D vertically stacked devices, was recommended as a means to continue the trend of

transistor scaling [13]. The projected evolution of transistor device architectures in the IRDS More Moore roadmap is as shown in Figure 1.6 below.

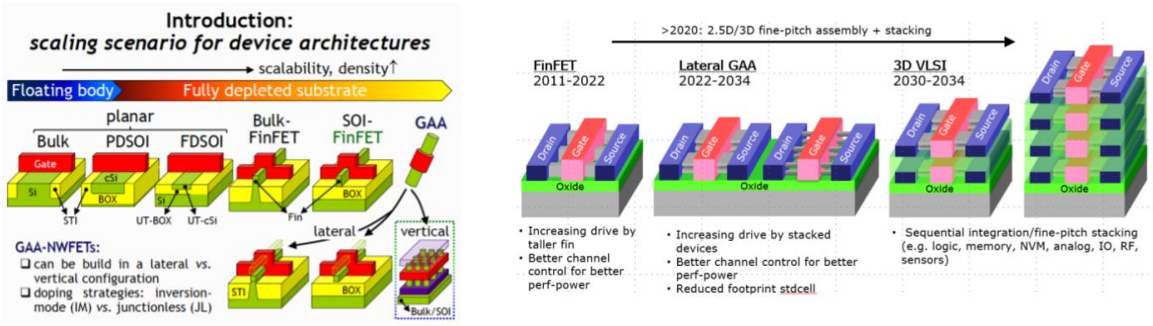

(a) (b)

Figure 1. 6 (a) Planar to GAA transition; (b) Evolution of device architectures in the IRDS More Moore roadmap (adapted from Ref. 13).

The "Beyond CMOS" document, released as part of the 2020 IRDS Report, also forecasted the development of novel logic switches such as Tunnel FETs (TFETs), SpinFETs, NEMS and Mott FETs, that might potentially replace and outperform silicon nanoelectronic devices [13].

1.2 Future trends in nanoelectronics

1.2.1 Alternative transistor materials

As mentioned earlier, nanometer-scale alternatives to silicon nanoelectronics would be required to continue the trend of miniaturization of electronic components like transistors. To this end, certain nanoscale materials like carbon nanotubes (CNTs) [14] and semiconductor nanowires [15] have been used as transistor channel materials.

CNTFETs are fabricated by depositing as-synthesized semiconducting carbon nanotubes from solution onto oxidized silicon wafers, which have been prepatterned with gold or

platinum electrodes [14]. The electrodes, which serve as the source and drain, are connected via the nanotube channel, and the doped silicon substrate serves as the gate [14]. Figure 1.7 shows a schematic of the earliest CNTFET, as well its band diagrams and *I*-*V* characteristics. Gate voltage modulation of the drain current, very low transconductance and high on-state resistances of the order of MΩ, were obtainable with the early CNTFETs [16].

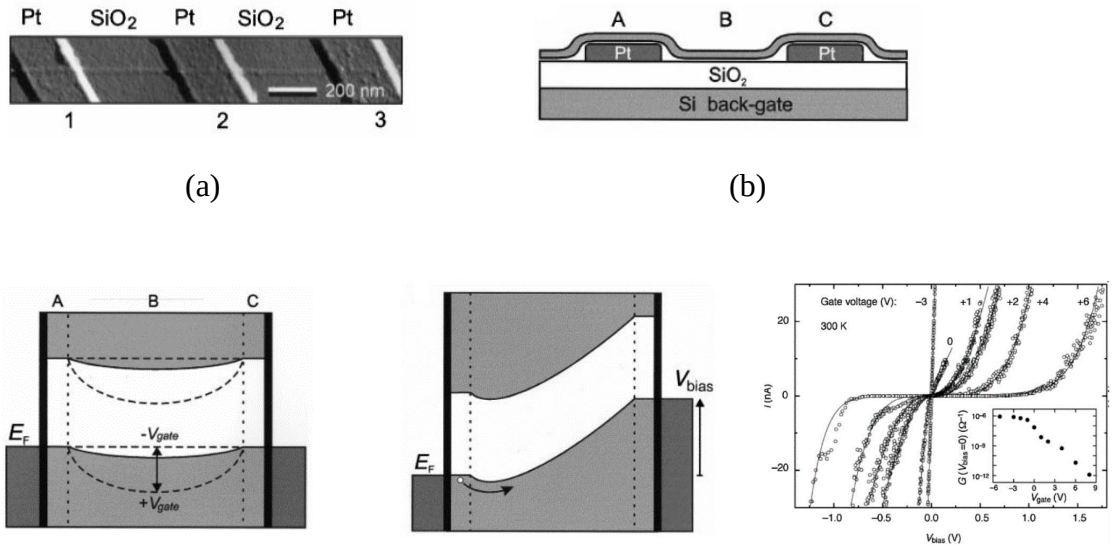

Figure 1. 7 (a) Tapping-mode atomic force microscope (AFM) image of an individual carbon nanotube on top of three Pt electrodes; (b) Schematic depiction of a CNTFET; (c) Suggested band diagram of the device; (d) Application of a bias voltage results in a suppression of the barrier; (e) *I*-*V* curves of the SWCNT-FET at room temperature. The inset shows the transfer characteristics of the device (adapted from Ref. 16).

CNTFETs are believed to function as Schottky-barrier transistors: in essence, the applied gate potential modulates the carrier density and transmission through the Schottky barriers at the contacts. Various architectures of CNTFETs, such as; top-gate, wrap-around gate

and back-gate CNTFETs were created in a bid to engineer effective CNTFETs with improved electrical characteristics [14].

Another nanoelectronic device with potential for future logic circuit applications is the NWFET [15]. Nanowires are desirable for fabricating electronic devices because they have highly controllable dimensions [15], and high carrier mobilities [15], [17], [18].

Figures 1.8 (a) shows the SEM image of a top-gated Indium arsenide (InAs) NWFET grown using molecular-beam epitaxy (MBE) [18]. The InAs nanowires (NWs) in the device have a diameter of 8.8 nm while the channel length is approximately 550 nm. Figure 1.8 (b) shows the linear relationship between source/drain current (I_{ds}) and the bias voltage (V_{ds}), indicating an ohmic contact to the InAs NW, while Figure 1.8 (c) shows the transfer characteristics of the device on a logarithmic scale, where V_{tg} is the top-gate voltage.

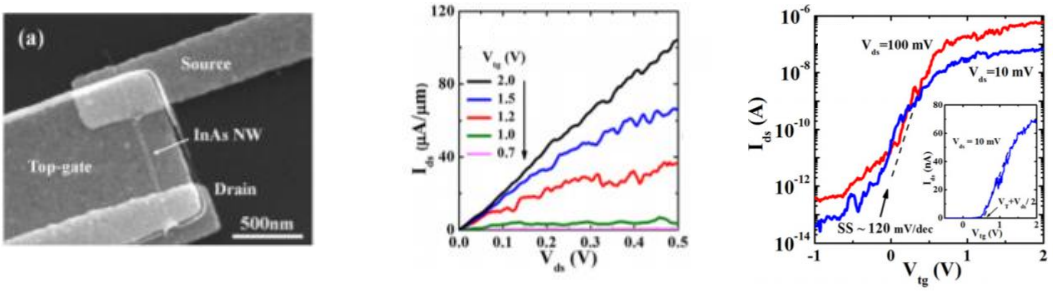

(a) (b) (c)

Figure 1. 8 (a) Top-view SEM image of a top-gate Indium arsenide (InAs) NWFET; (b) Output characteristics of the device on a linear scale; (c) Transfer characteristics of the device on a logarithmic scale. The inset is the transfer characteristics of the device on a linear scale showing n-type enhancement-mode operation with a threshold voltage V_T = 0.63V and V_{ds} = 10 mV (adapted from Ref. 18).

1.2.2 Nano-Electro-Mechanical switches/relays (NEMS)

The NEM relay or switch (Figure 1.9) uses the nanometer-scale mechanical motion of a movable electrode to make/break physical contact between two conductive electrodes to switch current on or off [19].

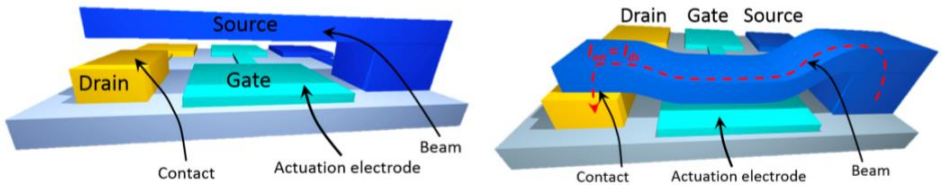

(a) (b)

Figure 1. 9 Illustration of an electrostatic 3T relay (a) as fabricated; (b) actuated into the ON state (adapted from Ref. 19).

Figure 1.10 below shows an image of an NEM relay comprising of three multi-walled carbon nanotubes (MWCNT) [20]. Applying a positive voltage above the threshold bias to either the drain or gate electrodes causes the drain CNT to bend towards the grounded source to form a contact and switch to the ON state [20], [21]. The *I-V* curve of the NEM relay (Figure 1.10 (d)) shows an abrupt switching behaviour, with SS ≈ 0, thereby allowing for a very small operating voltage swing (~ 10 mV) [20].

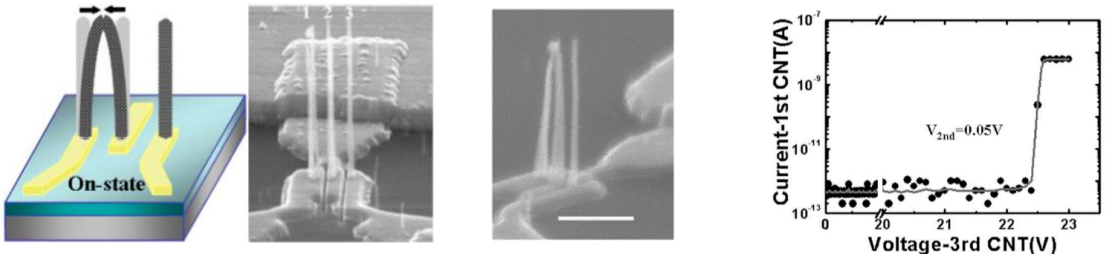

(a) (b) (c) (d)

Figure 1. 10 (a) Schematic illustration of the CNT-based NEM; (b) SEM image of NEM relay when OFF; (c) SEM image of NEM relay when ON; (d) *I-V* characteristics of switching action in an ambient environment. Scale bar corresponds to 1 μm. (adapted from Ref. 20).

NEM switches offer several advantages over their CMOS transistor counterparts for low-power logic applications such as; negligible leakage currents and operability with very small voltage signals for low dynamic power consumption [19].

1.2.3 Single-electron transistor (SET)

Another nanoscale electronic device which could potentially be useful in future electronic circuits is the single-electron transistor (SET) (Figure 1.11) [22].

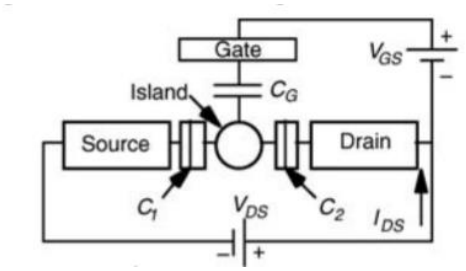

Figure 1. 11 Circuit diagram of the SET (adapted from Ref. 22).

The SET allows a single electron to tunnel from the source electrode onto the island and then to the drain electrode by a phenomenon called coulomb blockade [23]. The island is capacitively coupled to the gate electrode and the gate controls the tunneling current across the tunnel junctions. The drain-source voltage determines the energy of the electrons at the junction, and electrons will tunnel through the junctions if their energy is greater than the coulomb blockade [23].

Figures 1.12 (a) show the SEM images of an SET device made using 20 nm gold nanoparticles (Au NPs), gold nanorods (Au NRs) and electrodes. In the device, the AuNPs act as the island and they are connected to the source and drain electrodes using the Au NRs as electrical leads or tunneling junctions [24]. The NR-NP-NR junctions are first

synthesized by a self-assembly process in solution before contacting the nanorods using a lithographic process. The steps involved in formation of the device are shown in Figure 1.12 (b-f) [24].

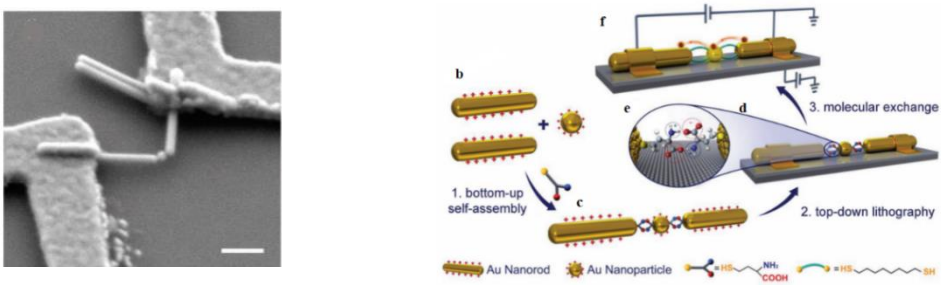

(a) (b-f)

Figure 1. 12 (a) SEM image of the SET (scale bar corresponds to 100 nm); (b-f) Methodology involved in making the SET device (adapted from Ref. 24).

Advances in the fields of nanotechnology and nanoelectronics have effectively made miniaturization of electronic components possible up to a certain extent; molecular electronics, a subset of nanoelectronics, is expected to take this miniaturization even further by enabling the fabrication of functional electronic devices using single molecules or an assembly of molecules**.** This could be advantageous in several ways: Quantum mechanical effects like ballistic conductance could make for more effective electronic components. Additionally, the bottom-up self-assembly approach, which is primarily the method of fabricating molecular structures is cheap and straightforward and allows for synthetic tailorability of the molecular structures' properties [25].

1.2.4 Molecular electronics

The field of molecular electronics began officially in the 1970s when various research groups began measuring electronic transport through molecular monolayers [25]. Since

then, various research groups have demonstrated the suitability of molecules and molecular units as electronic device components.

In 1971, Kuhn and Mann conducted conductivity measurements on Langmuir-Blodgett (LB) molecular films of cadmium salts of fatty acids sandwiched between metal electrodes, and the result showed that conductivity decreased exponentially with increasing length of the molecules [26].

In 1974, the idea of single-molecule electronics was proposed by Aviram and Ratner [27], when they noticed a correlation between charge-transfer salts like tetrathiafulvalene-tetracyanoquinodimehtane (TTF-TCNQ) and traditional semiconductor diodes. They believed that on the application of a positive bias above the threshold voltage, the electron-rich functional unit, TTF would act as a donor of electrons to the electron-poor unit, TCNQ via electron tunneling. The nonreversibility of internal tunneling for small applied fields yields the rectification properties of the molecule. The structure of the molecule and tunneling mechanisms of the proposed device are shown in Figure 1.13 [27].

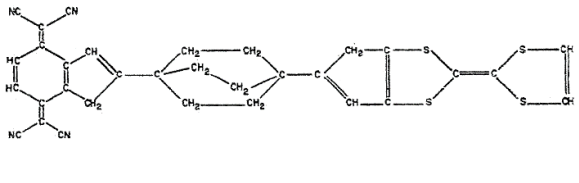

(a)

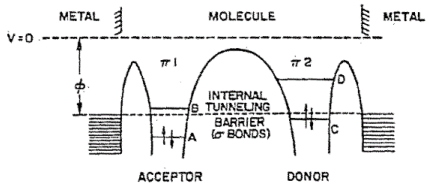

(b)

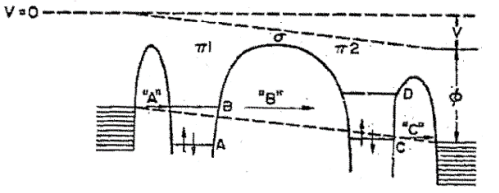

(c)

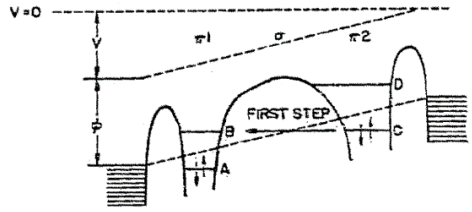

(d)

Figure 1. 13 (a) The rectifier molecule; (b) Schematic of the energy versus distance of the device. B and D are the affinity levels and A and C the highest occupied levels, of acceptor and donor, respectively; (c) Energy levels shift with applied voltage. “A”, “B”, and “C” are three tunneling processes; (d) Energy level shift with reverse applied voltage (adapted from Ref. 27).

Since then, the molecular diode/ rectifier has been demonstrated [28], [29].

Also, hysteresis and bistability have been demonstrated in certain molecular units thereby suggesting possible applications in memory and digital electronic devices [30].

Molecular computing devices have also been theorized [31] and demonstrated using molecules with switching properties [32].

The molecular transistor is another unique nanoelectronic circuit component that has been widely demonstrated [33], [34]. It is typically fabricated by connecting individual molecules to source and drain electrodes with a bottom-gate electrode attached [34].

Single molecules and molecular networks such as self-assembled monolayers (SAMs) and oligomers have been widely investigated for molecular electronics applications [35], [36], [37], [38]. SAMs are highly ordered two-dimensional molecular networks that form spontaneously on substrates [39], and are a ubiquitous topic in molecular electronics research due to their low cost and ease of fabrication [35], [36], [37], [38], [40].

The typical SAM structure is shown in Figure 1.14 (a) below. The headgroup of the SAM binds to the surface; the backbone, which usually comprises of an aromatic oligomer or

aliphatic chain, is responsible for molecular ordering, and the end or terminal group defines the surface energy, topography, and functionality of the SAM [40].

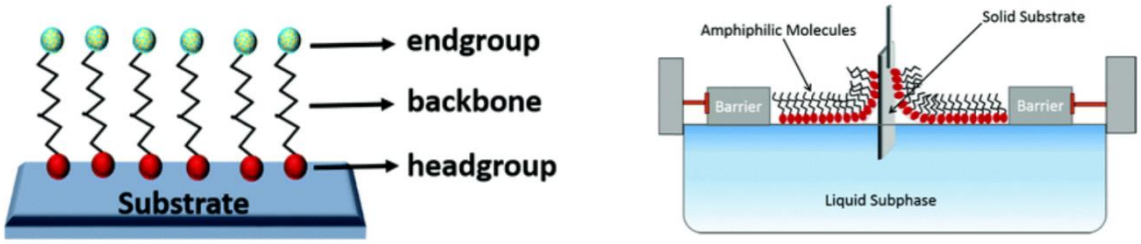

(a) (b)

Figure 1. 14 (a) Structure of a self-assembled monolayer; (b) Mechanism of Langmuir-Blodgett film formation on a solid substrate (adapted from Ref. 40).

To enhance their applicability in molecular (electronic) devices, SAMs are usually deposited on substrates using techniques like the Langmuir-Blodgett technique, dipping and vapor phase deposition.

In the Langmuir-Blodgett technique (Figure 1.14 (b)), the molecules are deposited in a container which holds the liquid subphase (water), such that the water-insoluble molecules spread out on the surface of the water to form a Langmuir monolayer. The monolayer can then be transferred to a solid substrate by dipping the substrate through the monolayer, while compressing the monolayer with barriers, and maintaining a constant surface pressure.

Two groups of SAMs are typically studied - SAMs of small molecules (thiols, silanes, etc.) and polymer SAMs (long chains of macromolecules). Of the former group, the SAMs formed using aliphatic and aromatic Sulphur-containing compounds (alkanethiols and benzenedithiol respectively) on gold surfaces have been most extensively studied because

they contain functional groups which react strongly with the gold surface to form SAMs with high density and uniformity. For forming SAMs using thiols on gold (Au(111)) surfaces, the headgroups of the SAM chemisorb on specific sites of the surface to form the ordered monolayer [39].

SAMs containing mixtures of gold nanoparticles (AuNPs) and thiol molecules deposited on solid substrates have also been extensively studied [41]. Figure 1.15 (a) shows a TEM image of a well-ordered SAM comprising of 5 nm diameter gold nanoparticles encapsulated by dodecanethiol molecules [41]. The 5 nm gold nanoparticles were mixed with dodecanethiol in ethanol to produce a colloidal suspension of alkanethiol encapsulated-gold nanoparticles. The colloidal suspension was then dropped on a water subphase to form thin nanoparticle films devoid of cracks at the center of the Petri dish, which were subsequently transferred to solid substrates (Figure 1.15 (a)). Figure 1.15 (b) shows a TEM image of AuNP networks comprising of alternating multilayer and monolayer rings, which was obtained for films formed at the edge of the Petri dish.

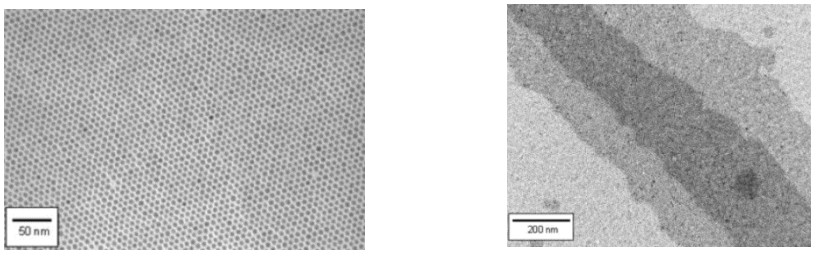

(a) (b)

Figure 1. 15 (a) TEM image of the AuNP-dodecanethiol film taken from the centre region of the Petri dish; (b) TEM image of the AuNP-dodecanethiol films taken from the edge of the Petri dish (adapted from Ref. 41).

Apart from the method of mixing AuNPs and thiolate molecules before depositing them on substrates, gold nanoparticle-(di)thiol SAMs are also commonly formed by first

immersing gold substrates in alkane(di)thiol solutions before dipping the substrates in AuNP suspensions [42], [43]. Dithiol molecules are of particular interest for these SAMs because both head- and end-groups are thiols (Figure 1.16), which allows for attachment to the Au(111) substrate and AuNPs. Figures 1.16 (a-b) show AFM images of AuNPs adsorbed to pre-formed (di)thiol SAMs.

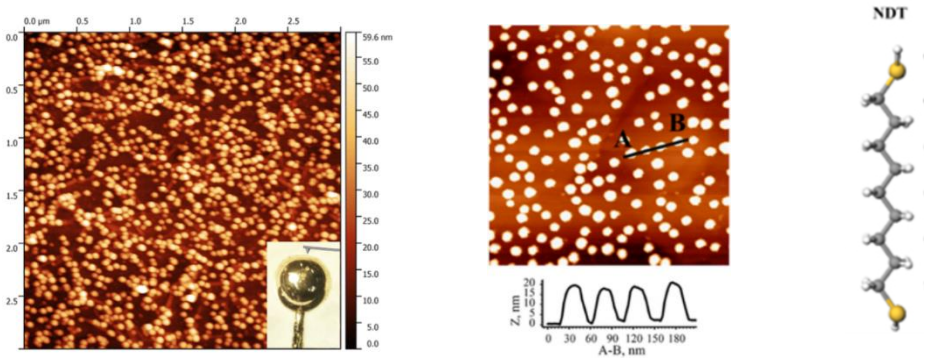

(a) (b) (c)

Figure 1. 16 (a) AFM image of a gold microsphere modified with 16-amino-1-hexadecanethiol followed by electrostatic adsorption of 30 nm AuNPs, inset shows a zoom-in image of the spherical gold microelectrode (microsphere) with 400 μm diameter, with the dithiol SAMs deposited on it (adapted from Ref. 42); (b) AFM images of AuNPs after immobilization by the thiol end-groups of the nonanedithiol (NDT) SAM, inset is a cross section along line AB (adapted from Ref. 42); (c) Chemical structure of nonanedithiol (adapted from Ref. 43).

Mixtures of AuNPs and thiols do not always self-assemble into uniform well-ordered networks or SAMs but sometimes form networks of AuNP nanoclusters linked by (di)thiol molecules called oligomers [44]. Figures 1.17 (a) and (b) show TEM images of 10 nm AuNPs mixed with hexa-ethylene-glycol dithiol (DT6) with different AuNP:DT6 ratios [44]. Smaller oligomers such as dimers, trimers, tetramers etc., can be formed when a few nanoparticles are bridged by molecules. Figure 1.17 (c) shows a TEM image of gold nanoparticle dimers linked by thiol molecules [45].

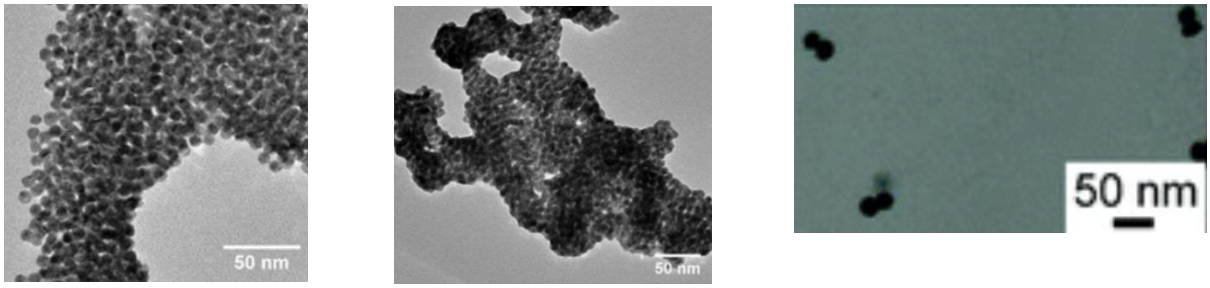

(a) (b) (c)

Figure 1. 17 (a) TEM image of dried 10 nm AuNPs mixed with DT6 at a molar ratio AuNP:DT6 of 1:850 (adapted from Ref. 44); (b) TEM image of dried 10 nm AuNPs mixed with DT6 at a molar ratio AuNP:DT6 of 1:8500 (adapted from Ref. 44); (c) TEM image of AuNP dimers linked by thiol ligands (adapted from Ref. 45).

Molecular electronics research was spurred on by the invention of tools and techniques (e.g., scanning probe microscopes (SPM) [46]) for imaging, measuring, and manipulating structures at the atomic scale. A scanning tunneling microscope (STM) image showing the observation of different configurations of an isolated organic molecule on a silicon surface is shown in Figure 1.18 (a) [47], while Figure 1.18 (b) shows an AFM image of a 12-layer 22-tricosenoic acid LB film deposited on silicon [48].

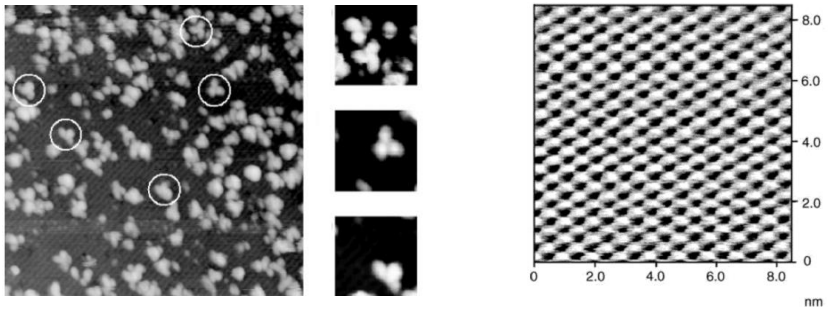

(a) (b)

Figure 1. 18 (a) Observation of different configurations of an isolated organic molecule on a silicon surface (adapted from Ref. 47); (b) AFM image of a 12-layer 22-tricosenoic acid LB film deposited on silicon (adapted from Ref. 48).

Another significant invention that benefitted molecular electronics research was the break junction, which consists primarily of two electrodes separated by a nanoconstriction, that could be used for measuring the conductance of a molecule.

Figure 1.19 shows the schematic of the mechanically controlled break junction (MCBJ) system [49]. The MCBJ sample is mounted on a three-point bending mechanism (Figure 1.19 (a)) and a bending force is applied to the bottom of the sample by a pushing rod (Figure 1.19 (b)), which elongates the metal bridge such that it breaks at its smallest constriction to create two separated electrodes. The distance between the electrodes can be controlled with sub-picometer accuracy by bending or relaxing the sample. The MCBJ synthesis process results in the formation of thin metal electrodes with a lateral constriction in between them (Figure 1.19 (c)) [49].

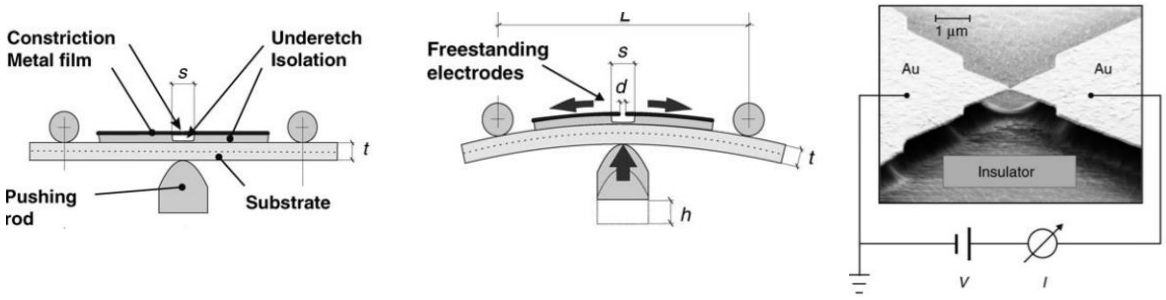

(a) (b) (c)

Figure 1. 19 (a) Schematic of the MCBJ sample mounted on the three-point bending mechanism; (b) The bending force applied to the bottom of the substrate breaks the metal bridge at its smallest constriction; (c) SEM image of an MCBJ sample (adapted from Ref. 49).

Another popular method of forming the metal-molecule contacts needed to probe molecules is by using gold nanoparticles (Au NPs) coated with alkanedithiol molecules dielectrophoretically trapped between two gold electrodes [50]. Jafri et al. conducted an

experiment using 5 nm AuNPs coated with ω-triphenylmethyl (trityl)-protected 1,8 octanedithiol (ODT) and 1,6-hexanedithiol (HDT) molecules trapped between two gold nanoelectrodes [50]. The schematic of the setup used for the experiment, microscope images, and *I-V*s of the alkanedithiol-Au NP networks are shown in Figure 1.20.

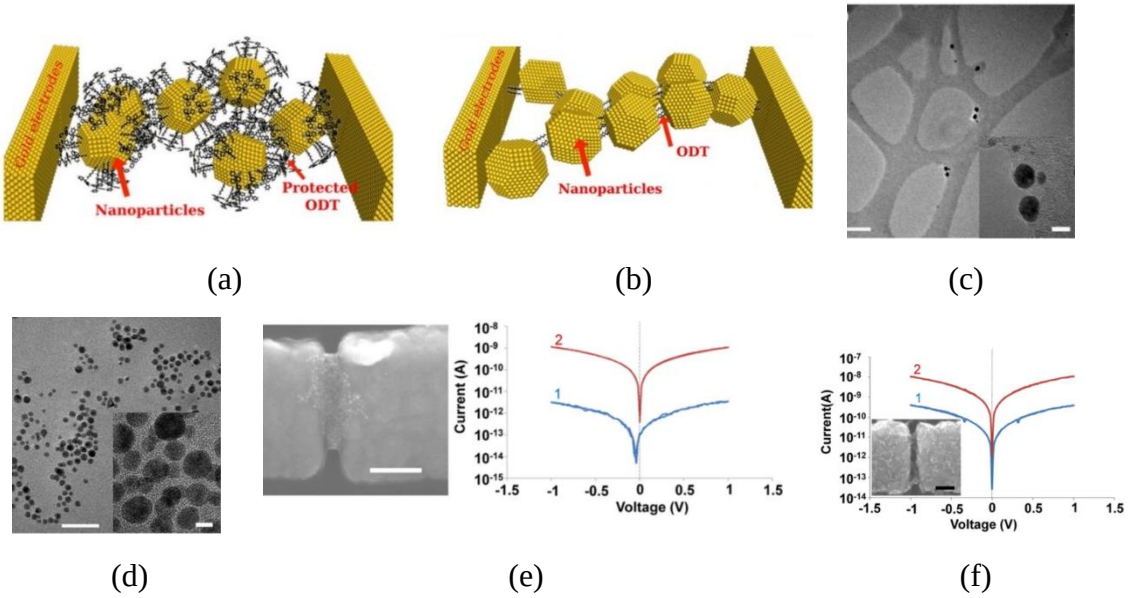

Figure 1. 20 (a) Schematic of ω-trityl protected 1,8-ODT-coated AuNPs; (b) Schematic of 1,8-ODT-coated AuNPs; (c) TEM images of trityl-protected 1,8-ODT coated AuNPs, scale bar: 20 nm (Inset: high resolution image with a scale bar of 5 nm); (d) TEM images of 1,8-ODT coated Au NPs, scale bar: 20 nm (Inset: high resolution image with scale bar of 5 nm); (e) SEM image of ω-trityl protected 1,8-ODT-coated AuNPs trapped between nanoelectrodes and *I-V* response of the same device after (1) trapping and (2) removal of trityl protective groups from 1,8-ODT; (f) *I-V* response of 1,6-HDT coated AuNPs (inset: SEM of resultant device, scale bar: 50 nm) after (1) trapping and (2) removal of trityl protective groups from 1,6-HDT (adapted from Ref. 50).

The electrical conductivity of molecular systems has been extensively studied by researchers to understand their electronic properties and provide possible routes for molecular electronic device fabrication [26], [51], [52]. Two theoretical approaches have

been widely used to model electronic transport through molecular systems bridged between metallic electrodes, namely, the Landauer method and the Non-equilibrium Green's Function (NEGF) method [53].

In the Landauer method, the system is partitioned into three regions: a central region that includes the molecule and a portion of the electrodes; and left and right electrodes, in equilibrium at some electrochemical potential, $\mu_{L,R}$.

Transport, in the Landauer method, is viewed as a scattering problem, in which an incident carrier flux from one of the leads is scattered by the central region and transmitted to the other lead, and current is proportional to the transmission coefficient.

$$I = \frac{2e}{\hbar}\int \frac{dE_i dE_f}{2\pi} T(E_i, E_f)[f_L(E_i)\left(1 - f_R\left(E_f\right)\right) - f_R(E_i)(1 - f_L\left(E_f\right))] \quad (1.1)$$

where I is the current, e is the elementary charge, ħ is planck's constant, $T(E_i, E_f)\ dE_f$ is the probability that an electron incident on the molecular target with energy, E_i will be transmitted with energy, E_f, $f_L(E)$ and $f_R(E)$ are the Fermi functions of the left and right leads.

The NEGF method includes the effects of inelastic scattering and electron-electron interactions under non-equilibrium conditions and gives a more general approach for solving the transport problem [53].

The Density Functional Theory (DFT) allows for the calculation of the properties of a molecular system based on a description of the positions and species of the individual atoms in the system.

The NEGF formalism, combined self-consistently with DFT (DFT-NEGF) is the most ubiquitous method of modelling electronic transport at the nanoscale [54]. The DFT is first used to obtain the Hamiltonian and electronic structure for the scattering region and then

the NEGF method is used to solve for the charge density, transmission and current of the molecular system [54].

A myriad of studies have been conducted on modelling the electronic transport properties of molecular systems, with the benzenedithiol (BDT) molecule being the model system used for investigating molecular transport junctions [55], [56], [57], [58], [59].

A DFT-NEGF study of the Au-BDT-Au molecular junction, with device configuration shown in Figure 1.21 (a), was conducted by Mao et al [59]. Figure 1.21 (b) presents the molecular energy spectrum projection of the BDT molecule in the junction [59]. The molecular projected self-consistent Hamiltonian (MPSH) of the BDT molecular junction (Figure 1.21 (b)) shows that the overlap between Sulphur atoms and the π orbital of the benzene ring moiety contributes to the highest occupied molecular orbital (HOMO) level [59].

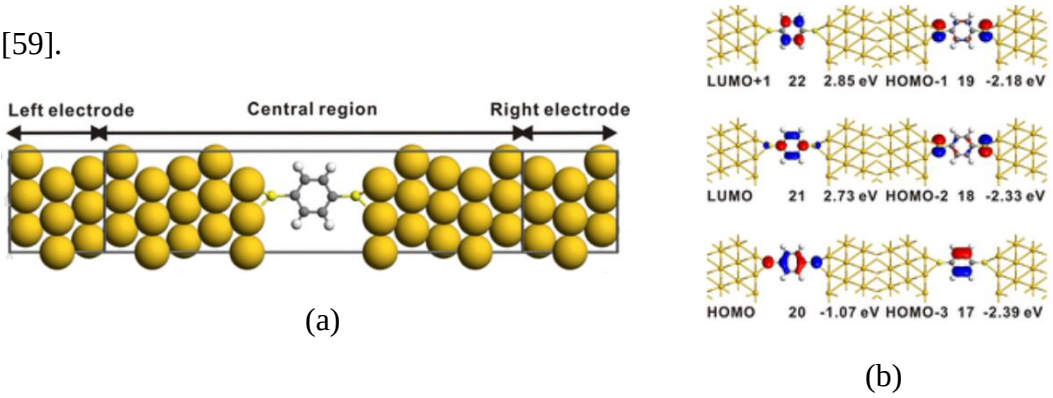

(a) (b)

Figure 1. 21 (a) Device configuration of Au-BDT-Au molecular junction consisting of the central region and left/right electrodes. Two S atoms of BDT adsorb at hollow sites of the Au electrodes; (b) Molecular energy spectrum projection of BDT, with isovalue surface set at 0.05 au (adapted from Ref. 59).

Conduction mechanisms in molecules are largely grouped into temperature-dependent and temperature-independent mechanisms [60]. Thermionic and hopping conduction are examples of thermally activated conduction mechanisms, and molecules which exhibit this form of conduction are usually superconducting at higher temperatures [60]. For example,

hopping conduction is believed to be the dominant conduction mechanism in CNTs [61] and pure CNT fibers have been shown to exhibit temperature-dependent *I-V* characteristics [62].

Fowler-Nordheim and direct tunneling are the primary temperature-independent conduction mechanisms [60]. The conduction mechanism in alkane(di)thiol molecules and SAMs coupled to gold electrodes is believed to be via non-resonant tunneling and this explains the length-dependent conductivity of alkane(di)thiol molecules where the chain length of the molecule is analogous to the tunneling barrier width [50]. It also explains the lack of temperature dependence of current observed in alkane(di)thiol molecules and SAMs [63], [64].

1.3 Overview of Thesis

The notion of alternating or complementing silicon nanoelectronics with molecular electronic devices has been proposed as a means to achieve functional deep nanoscale circuit elements [12]. The investigation of the use of single molecules and molecular networks as functional electronic components is a ubiquitous topic in electronics research, and molecular networks such as SAMs and oligomers have been extensively studied for possible circuit applications due to their ease of fabrication, low cost, and intrinsic size [50], [52], [65], [66].

Motivated by prior work on metal nanoparticle-molecular systems comprising of either bulk film SAMs or nanoparticle oligomers [35], [36], [37], [38], [45], this work contains studies of the electrical and electronic properties of nanoscale gold-dithiol molecular

networks with an intermediate number of dithiol molecules, conducted both theoretically and experimentally. The effects of varying the dithiol molecule to gold nanoparticle concentration and/or the type of dithiol molecule used in the molecular networks were studied, and the tunability of the electrical properties of the networks was facilitated by varying those parameters. High voltage and cyclic voltammetry measurements were also conducted on the molecular networks and they showed switching, negative differential resistance, and hysteretic behaviour.

To complement the experimental studies conducted on the molecular networks, their properties were also modelled. The electrical properties of the molecular networks were modelled using LTspice simulations of a nanoscale resistive network. The electronic properties of gold-dithiol molecular networks were modelled using DFT-NEGF-based simulation methods.

In conclusion, possible circuit applications of the molecular networks (in molecular switches, logic circuits, molecular ICs etc.) based on the experimental/computational results were proposed.

Chapter 2 focuses on experimentally implementing the gold-dithiol nanoscale networks by self-assembly. The solution-based fabrication method, used to synthesize the molecular networks, is discussed. Previous works focused either on dense close-packed films of gold-dithiol molecules or oligomers of gold nanoparticles interconnected by dithiol molecules, but this work aims to study metal-molecular networks with an intermediate number of molecules linking the gold nanoparticles. The concentration of molecules in the metal-molecular networks was varied to allow for tunability of the networks' properties. Results

from the structural characterization of the fabricated self-assembled molecular networks using AFM and optical microscopy were also included.

Chapter 3 contains results from electrical characterisation of the self-assembled molecular networks. Additionally, the impacts of the type and concentration of molecules, size of metal nanoparticles, and the applied bias, on the electrical properties of the molecular networks were studied by using different types and concentrations of dithiol molecules and varying the applied bias. The conductivity or electrical properties of the networks were found to depend on the dimensions of the network, resistance of molecules, and applied bias. Finally, the electrical properties (*I-V* curves) of the networks were modelled using a nanoscale resistive network with component resistance values chosen depending on the type and concentration of molecule used and percentage of defects. The circuit modelling was performed using LTspice and the results showed some agreement with experimental data (for example, the resistance of the networks typically increased with an increasing concentration of molecules).

Chapter 4 focuses on modelling the electronic properties of gold-dithiol metal-molecular networks using density functional theory (DFT)-based simulation methods. The simulation packages, Spanish Initiative for Electronic Simulations with Thousands of Atoms (SIESTA), TranSiesta and TBTrans were used for performing calculations on networks built of interconnected benzenedithiol molecules and AuNP clusters. The transmission properties, *I-V* curves, density of states (DOS) and molecular orbitals of the networks are obtained and visualized using various SIESTA utilities. Finally, possible circuit

applications (in molecular switches, logic circuits, molecular ICs etc.) using the molecular networks are proposed.

Chapter 5 concludes the thesis by summarizing key points in the work, discussing possible future research tasks and highlighting possible device applications using the molecular networks.

The work in this thesis contributed to one journal paper [67], and two conferences [68], [69]. Another journal paper is under revisions [70] and another is in progress [71]. Additionally, a review article on carbon nanotubes was published [72], and another review article on nanoscale self-assembly [73] was submitted during the course of this work.

The experimental works, [67], [69], and [71], highlighted the tunability of the electrical properties (e.g., current and resistance) of metal-molecular networks having an intermediate number of molecules on modifying the thiol molecule-to-gold nanoparticle ratios and operating voltages of the devices, as well as the applicability of this tunability for generating random binary sequences for hardware security applications.

The modelling works, [68], and [70], highlighted the tunability of transmission (i.e., increase in the number and/or width of transmission peaks near the Fermi energy) of the benzenedithiol-Au_6 linear chains as the structures were extended. Additionally, nonlinear *I-V* characteristics and NDR effects which became more pronounced as the structures were extended, were observed in all the benzenedithiol-Au_6 linear and branched chains studied, highlighting their potential for application as circuit elements in nanoelectronic devices and circuits, including memory, logic, switching and sensing.

Chapter 2 Fabrication and Structural Characterization of Self-Assembled Metal-Molecular Networks with tunable metal nanoparticle (NP): molecule ratios

2.1 Introduction to self-assembled metal-molecular networks and their fabrication methods

The self-assembled metal-molecular networks studied in this work were fabricated using a solution-based method, which allows for the tunability of the networks' electrical properties by varying the type and ratio of molecules used in the solution.

2.1.1 Self-assembled Nanoparticle Layers

Weisbecker et al. used a similar approach to [41] introduced in Chapter 1 for fabricating self-assembled metal-molecular monolayers: SAMs were formed by the chemisorption of alkanethiols onto gold colloids (nanoparticles) in the presence of aqueous ethanol [74]. Aqueous dispersions of gold colloids, stabilized by the addition of sodium hydroxide (NaOH) solution, were mixed with an equal volume of alkanethiol solution in ethanol [74]. The resulting functionalized gold dispersions contained gold nanoparticles approximately 40 nm in diameter encapsulated by thiol molecules. A nonfunctionalized control solution was also prepared by mixing a portion of the colloidal gold solution with an equal volume of ethanol.

Drops of the dispersions were evaporated to dryness and TEM images of the dried precipitates of the functionalized dispersions showed the formation of ordered networks (Figure 2.1 (a)) with individual gold nanoparticles having visible surface coatings about 2 nm thick (Figure 2.1 (b)) indicating the formation of SAMs on the gold colloids [74]. Conversely, TEM images of the dried control precipitates showed chains of aggregated gold nanoparticles (Figure 2.1 (c)), wherein individual gold colloids had become fused together (Figure 2.1 (d)) [74].

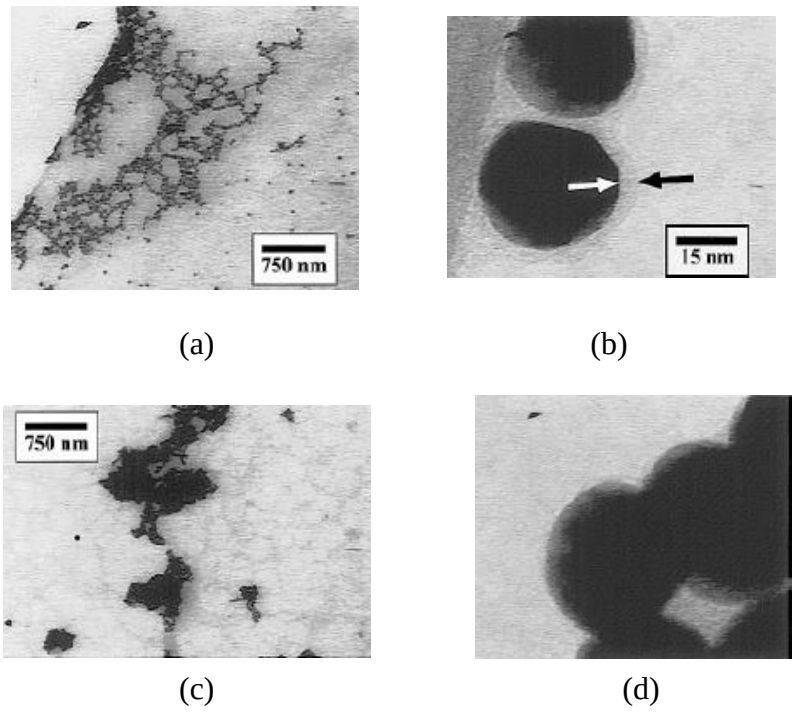

Figure 2. 1 (a) Floc of colloids that had been previously exposed to (11-mercaptoundecanyl)-1-phosphonic acid-terminated thiol, $HS(CH_2)_{11}PO_3H_2$; (b) a coating of material approximately 2 nm thick surrounding colloids that were exposed to thiol, $HS(CH_2)_{11}PO_3H_2$; (c) a floc of colloids that had not been exposed to any thiol; (d) unexposed colloids that became fused together (adapted from Ref. 74).

As introduced in Chapter 1 (Ref. 42), Santhanam et al. fabricated well-ordered SAMs containing mixtures of 5 nm AuNPs and alkanethiol molecules [41]. 5 mL of a 0.083 μM citrate-stabilized gold solution was mixed with 100 μL of a 20 mM solution of dodecanethiol in ethanol for 20 minutes. 30 mL of ethanol was used to top up the mixture, which was then allowed to sit for 2 hours before centrifuging for 1 hour at 3400 rpm. Following this, the supernatant solution was decanted, and the precipitate was dried in air overnight. Finally, the dried precipitate was dissolved in an appropriate solvent to produce a 1 μM colloidal solution. Using the above recipe, the ratio of thiol molecules to gold nanoparticles in the colloid solution was approximately 4800:1. Uniform monolayers were formed by dropping 0.4 mL of the 1 μM colloidal solution on a water surface inside a Teflon dish, allowing the organic solvent to evaporate, and subsequently transferring the monolayer films to solid substrates by lightly touching a hydrophobic surface to the nanoparticle film and lifting from the water surface. *Polydimethylsiloxane* (PDMS) stamp pads were also used for transferring the monolayer films from the water surface to solid substrates using microcontact printing [41].

Figure 2.2 shows the TEM images of the nanoparticle films formed using various nanoparticle colloid concentrations while keeping all other experimental parameters at their optimum values.

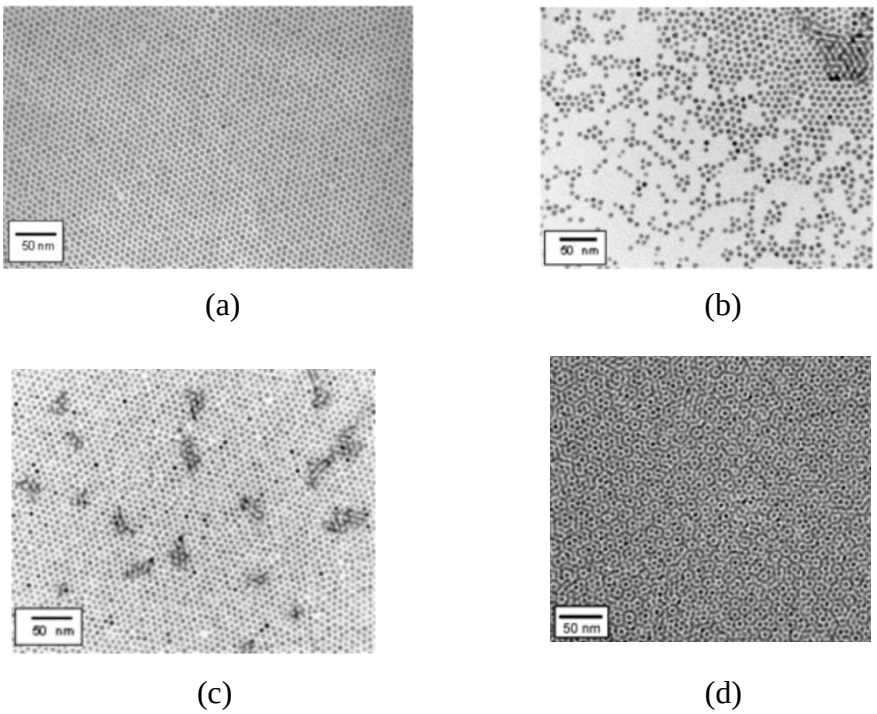

(a) (b)

(c) (d)

Figure 2. 2 TEM images of nanoparticle layers formed using different nanoparticle colloid concentrations (a) optimum concentration; (b) 50% of the optimum concentration; (c) 200% of the optimum concentration; (d) 400% of the optimum concentration (adapted from Ref. 41).

Figure 2.2 (a) shows the TEM image of a film formed using the optimum nanoparticle colloid concentration of 1 μM. In monolayers formed using 50% of the optimum colloid concentration (Figure 2.2 (b)), the nanoparticles cluster in small close-packed regions separated by sparsely populated domains, while in nanoparticle layers formed at 200% of the optimum colloid concentration, small patches of bilayers are randomly dispersed on a compact monolayer (Figure 2.2 (c)). Figure 2.2 (d) shows the TEM image of a uniform well-ordered nanoparticle bilayer formed at 400% of the optimum colloid concentration [41].

2.2 Fabrication Methods

2.2.1 Introduction to the Solution-based Fabrication Method

Dadosh et al. synthesized oligomeric structures comprising of a few gold nanoparticles connected by dithiolated organic molecules [75]. Dimer structures were synthesized by mixing equal volumes of a solution of dithiol molecules in NaOH with a colloidal gold solution consisting of 30 nm citrate-stabilized gold nanoparticles, using a molecule: AuNP ratio of about 1:10 [75]. Larger structures (trimers, tetramers and larger oligomers) were also formed by this method when more than one molecule attached to certain colloidal gold particles, however, using a reaction mixture with molecule: AuNP ratio of about 1:10 increased the likelihood of forming dimer structures that were bridged by a single molecule. In the final step, the dimeric structures were separated from other oligomers via centrifugation [75].

Graf et al. [45] fabricated gold nanoparticle dimers using various processes such as; the direct coupling of the unprotected sites of two gold nanoparticles with a bifunctional linker, the linkage of two identical functionalized particles with a bifunctional linker in a single step, and the coupling of a bifunctional linker to a regioselective functionalized particle, followed by the reaction of the coupling product with another identical regioselective functionalized particle.

The highest yield of stable dimer structures was obtained using a regioselective functionalization synthesis method which entailed a locally confined surface modification of gold nanoparticles followed by the coupling of the complementary functionalized

nanoparticles using an organic linker (Figure 2.3). This method enables the controlled assembly of nanoparticle oligomers in which certain sites of the nanoparticles are tightly connected with other particles while the rest of the particle surface remains stable against any uncontrolled aggregation with other particles [45].

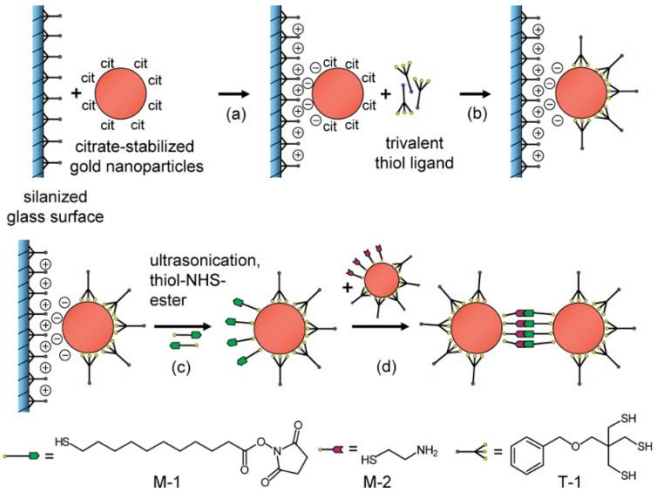

Figure 2. 3 Synthesis of gold nanoparticle dimers (a) Binding of citrate-stabilized gold nanoparticles to a silanized glass surface; (b) functionalization of the nanoparticle site opposite the glass with trivalent thiol ligands with a nonreactive group (here shown for ligand T-1); (c) detachment of the nanoparticles from the glass surface in the presence of a monovalent thiol ligand with a reactive group (here shown for ligand M-1, represented by a green pentagon); and (d) formation of dimers by binding to complementary functionalized gold nanoparticles (adapted from Ref. 45).

Functionalizing the gold nanoparticles with multivalent thiol molecules in the first step strongly increases their stability and protects them against uncontrolled aggregation with other gold nanoparticles in the presence of thiols. Figure 2.4 (a) shows the TEM image of the coupling products (dimers, trimers, and tetramers) formed using the process outlined in Figure 2.3 above, while Figure 2.4 (b) shows a TEM image of the coupling products of nanoparticles solely functionalized with two different monovalent thiol ligands, indicating

the presence of larger nanoparticle aggregates, and thus demonstrating the increased stability of trivalent thiol functionalized nanoparticles [45].

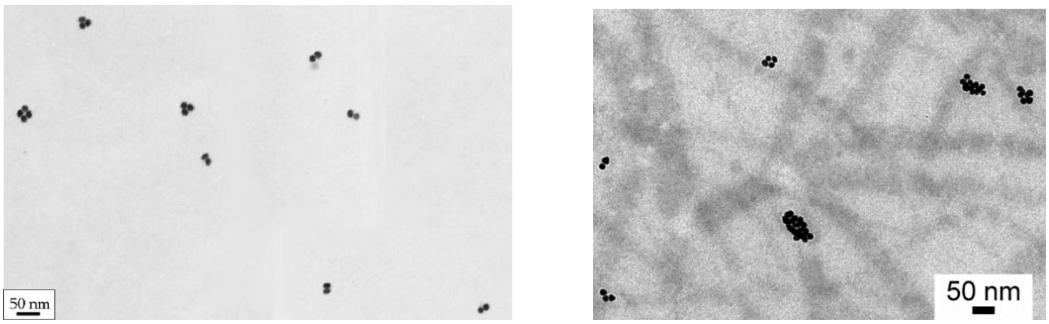

(a) (b)

Figure 2. 4 (a) TEM image of the coupling products of gold nanoparticles stabilized by the trithiol derivative T-1 and the NHS-ester derivative (ligand M-1) and those stabilized by the ligand T-1 and cysteamine (ligand M-2). A schematic presentation of the formation of these coupling products is shown in Figure 2.3; (b) TEM image of the coupling products obtained from gold nanoparticles stabilized with only monovalent ligands (adapted from Ref. 45).

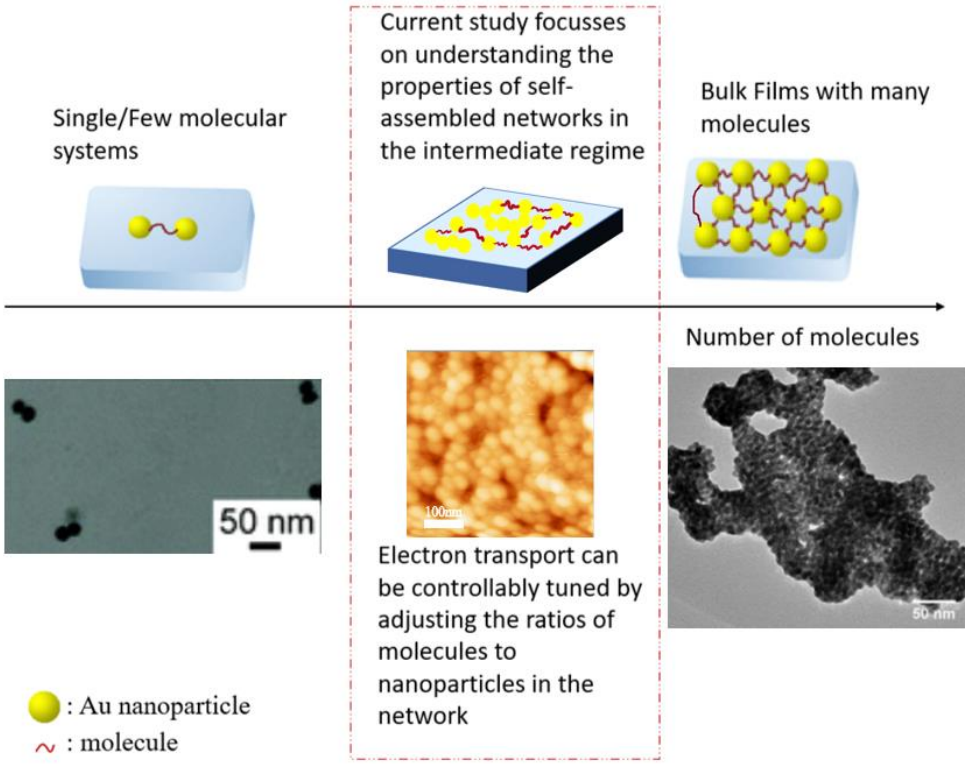

Figure 2. 5 Existing work on metal-molecular networks mainly focuses on studies with very few molecules (left) or many molecules compared to the number of gold nanoparticles (right) (adapted from Refs. 44, 45). The focus of the current work (centre) is on metal-molecular networks in the intermediate regime with tunable molecule-nanoparticle ratios.

Previous works in which structures comprising of gold nanoparticles interconnected by dithiol molecules were studied typically either focused on tightly packed networked layers of dithiol molecule-encapsulated gold nanoparticles fabricated using molecule: gold NP ratios of about 5000:1 [41], [44] or on small oligomeric structures comprising of a few gold nanoparticles linked by dithiol molecules, typically fabricated using molecule: gold NP ratios of about 1:10 [75]. The extremes of structures (comprising of a very high or very low concentration of molecules) that can be fabricated from interconnecting gold nanoparticles with thiol molecules have been extensively studied [35], [36], [41], [44],

[45], [74], [75], however the structures which lie between these two extremes have not been sufficiently characterized and this forms the motivation for this research work. Motivated by prior work on metal nanoparticle-molecular systems comprising of either bulk film SAMs or oligomers of gold nanoparticles interconnected by a few dithiol molecules, we fabricated and probed metal-molecular networks having an intermediate number of molecules. The synthesis method employed in fabricating our molecular networks resulted in networked aggregates of gold nanoparticles interconnected by a few dithiol molecules (Figure 2.5).

The fabrication method used for synthesizing the metal-molecular networks studied in this research work was based on an extension of the solution-based fabrication methods described by Weisbecker et al. [74] and Dadosh et al. [75], with some modifications.

Weisbecker et al. fabricated functionalized metal-molecular networks comprised of thiol-encapsulated interconnected gold nanoparticles (Figure 2.6 (a-b)) by mixing equal volumes of aqueous dispersions of gold colloids in NaOH and alkanethiol solutions in ethanol; and nonfunctionalized gold colloids comprised of chains of aggregated gold nanoparticles (Figure 2.6 (c)) by mixing equal volumes of colloidal gold solution and ethanol [74].

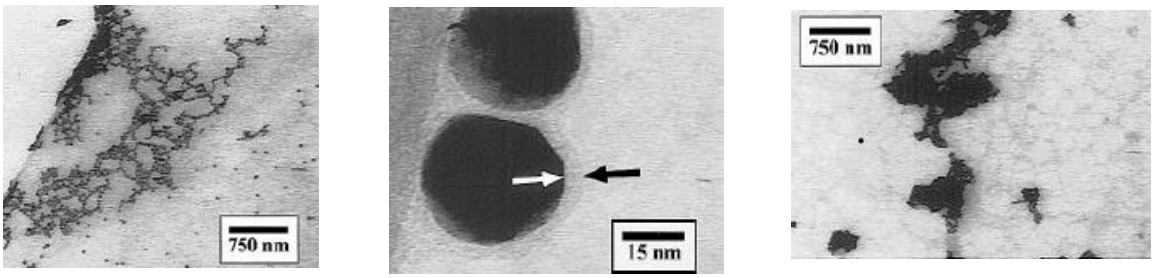

(a) (b) (c)

Figure 2. 6 Electron microscopy of dried flocs of gold colloids (a) a floc of colloids that had been previously exposed to thiol, $HS(CH_2)_{11}PO_3H_2$; (b) a coating of material approximately 2 nm thick surrounding colloids that were exposed to thiol, $HS(CH_2)_{11}PO_3H_2$; (c) a floc of colloids that had not been exposed to any thiols that became fused together (adapted from Ref. 74).

Dadosh et al. synthesized dimer structures (Figures 2.7 (a-b)) comprised of two gold nanoparticles bridged by a single dithiol molecule by mixing equal volumes of a solution of dithiol molecules in NaOH, and a colloidal gold solution using a molecule: AuNP ratio of about 1:10 [75]. Other oligomeric structures (e.g. trimers and tetramers) (Figures 2.7 (c-d)) were also fabricated by the above procedure [75].

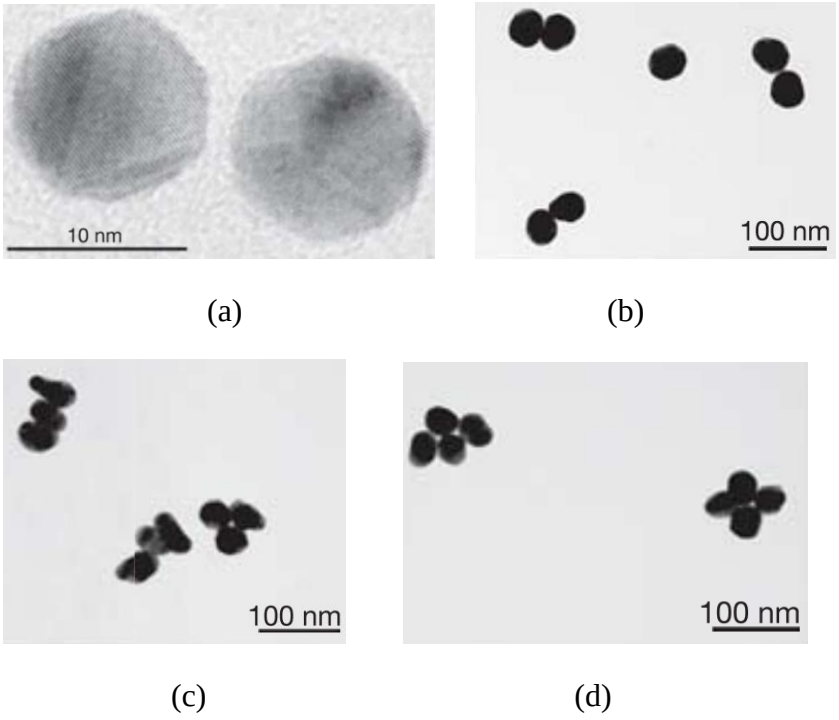

Figure 2. 7 (a) TEM image of a 1, 4-benzenedimethanethiol (BDMT) dimer made of 10 nm colloidal gold particles. The ~ 1 nm separation between the two particles corresponds approximately to the BDMT length (0.9 nm); (b-d) TEM images of BDMT dimer, trimer

and tetramer structures respectively, made of 50 nm colloidal gold particles (adapted from Ref. 75).

We employed Weisbecker's method of mixing equal volumes of gold nanoparticles dissolved in NaOH with thiols dissolved in ethanol, however we reduced the concentration of dithiol molecules to gold nanoparticles (hereafter referred to as $N_{molecule}$: $N_{particle}$) to avoid the formation of networks of thiol-encapsulated gold nanoparticles. Our recipe and resulting networks also differed from Dadosh et al.'s in that the concentration of dithiol molecules was higher than the concentration of gold nanoparticles, such that our resulting networks comprised of aggregates of gold nanoparticles interconnected by a few dithiol molecules, in contrast to their dimer structures. By varying the $N_{molecule}$: $N_{particle}$, we were able to control the number and distribution of molecular connections in the resulting networks.

2.2.2 Recipe for synthesizing metal NP-molecular networks with tunable metal NP: molecule ratios

1, 4-benzenedithiol, 1, 9-nonanedithiol (NDT), 10 nm, and 30 nm citrate-stabilized colloidal gold nanoparticles were purchased from Sigma Aldrich; NaOH pellets were purchased from EMD. NaOH solution and pure ethanol were used as solvents for the colloidal gold nanoparticles and dithiol solutions, respectively. Deionized water was used in all the experiments.

Molecular networks were fabricated by mixing equal volumes of concentrated colloidal gold solutions in NaOH with suspensions of dithiol molecules in ethanol and incubating the mixture at 4 °C for 24 hours before depositing on substrates (as outlined in Figure 2.8 below).

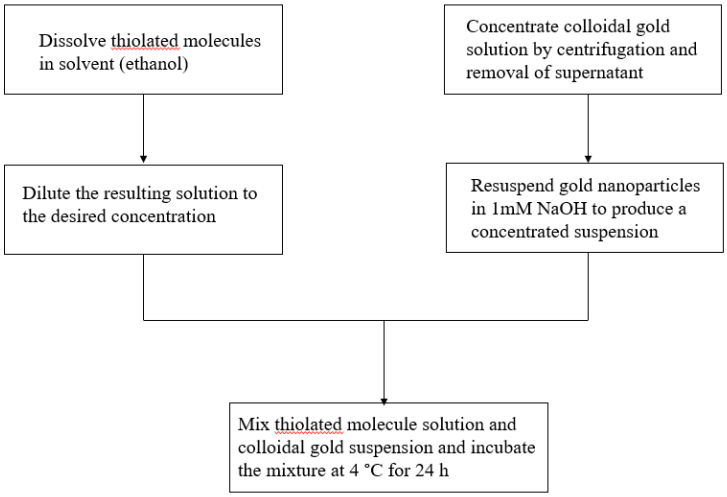

Figure 2. 8 Fabrication procedure for synthesizing metal-molecular networks.

The detailed steps followed to fabricate the molecular networks were as follows; Firstly, dithiol molecules were dissolved in ethanol and the solution was stirred on a VWR hot plate magnetic stirrer for 5 minutes at 300 rpm. Next, we filled five epitubes each with 39.5 µL of 10 nm colloidal gold solution and centrifuged at 9.8×10^3 g for 45 minutes, and the supernatant was discarded using a micropipette. Following this, the epitubes containing the gold nanoparticles were topped up with 1.25 mL of 1mM NaOH solution, and the precipitate was resuspended by handshaking, before being centrifuged again, this time for five minutes at 9.8×10^3 g. After the centrifugation process, the supernatant was discarded. The same procedure was repeated two more times, but for the second resuspension/centrifugation cycle, the precipitate was suspended in 0.25 mL of 1mM

NaOH solution, to produce a concentrated solution of colloidal gold (1.5×10^{-9} M) in NaOH.

The volume and concentration of dithiol molecules that was dissolved in ethanol varied depending on the type of thiol molecule being used in the molecular networks and the desired $N_{molecule}$: $N_{particle}$ of the networks being made. For example, to fabricate gold-nonanedithiol networks, we needed to prepare nonanedithiol solutions of different concentrations in ethanol and mix them with an appropriate amount of colloidal gold solution in NaOH. First, we prepared 100 mL of 1.5×10^{-4} M nonanedithiol (stock) solution by using the following steps; We filled 50 mL ethanol solution in a flask and added 3.2 µL of nonanedithiol solution to it (the correct volume of nonanedithiol needed to make a solution of the desired concentration was calculated based on the molecular weight and density of nonanedithiol). Next, we topped up the ethanol solution to the 100 mL mark. Finally, we put a magnetic stir bar in the flask and stirred the solution on a magnetic stirrer at 300 rpm for 5 minutes.

To prepare 100 mL of 1.5×10^{-9} M nonanedithiol solution in ethanol, 1 µL of the stock solution was added to a flask, diluted with 100 mL of ethanol, and finally stirred using a magnetic stirrer at 300 rpm for 5 minutes. 0.25 mL of the resulting solution was then mixed with an equal volume of 1.5×10^{-9} M colloidal gold solution in NaOH and incubated at 4 °C for 24 hours. Mixing equal volumes of the dithiol solution and colloidal gold solution of the same concentration results in the formation of a metal-molecule solution with $N_{molecule}$: $N_{particle}$ of 1:1.

The above synthesis procedure was repeated using nonanedithiol solutions with concentrations of 7.5×10^{-9} M, 7.5×10^{-8} M, and 3×10^{-10} M, and colloidal gold solution with concentration, 1.5×10^{-9} M to fabricate metal-molecular networks with $N_{molecule}$: $N_{particle}$ of 5:1, 50:1, and 1:5 respectively, in order to probe the effect of varying $N_{molecule}$: $N_{particle}$ on the networks' properties. Additionally, a control solution, containing colloidal gold particles dissolved in NaOH and pure ethanol, was synthesized. The resulting solutions of colloidal gold particles and dithiol molecules with $N_{molecule}$: $N_{particle}$, 5:1, 50:1, and 1:5, as well as the control solution were incubated at 4 °C for 24 hours.

The solution-based fabrication procedure outlined above is highly tailorable and can be used to fabricate metal-molecular networks using different types of thiol molecules (e.g. 1,4-benzenedithiol, 1-octanethiol, and 1, 6-hexanedithiol, etc.) and sizes of gold nanoparticles (10 nm, 30 nm, etc.) provided that accurate measurements of the required volumes and concentrations of the constituent solutions are made.

The metal-molecule solutions resulting from the fabrication were well-dispersed (as shown in Figure 2.9).

Figure 2. 9 Solution of 1, 9-nonanedithiol and colloidal gold particles with $N_{molecule}$: $N_{particle}$ of 1:1 after incubating for 24 hours.

In the final fabrication step, one or two 1 μL drops of the well-dispersed solutions of colloidal gold particles and dithiol molecules as well as the control solution were deposited on substrates; which had previously been rinsed with acetone, isopropanol and deionized water, and dried with nitrogen gas; using micropipettes and the dropped solutions were allowed to dry in air under ambient conditions.

2.2.3 Fabrication of samples/devices for electrical testing

The samples studied in this work comprised of metal-molecular networks deposited on substrates. The substrates for *I-V* measurements consisted of photolithographically patterned gold electrodes with a thin adhesion layer on a silicon wafer substrate coated with a 100 nm layer of silicon dioxide. The gold electrodes were 40 nm thick and typically separated by a gap of between 1 to 2.5 μm.

As mentioned earlier, the gold electrodes on the substrates were coated with a silicon dioxide layer, hence the wafers needed to be processed before using them for fabricating the devices in this study. First, the silicon wafer was sonicated in a solvent to remove the silicon dioxide coating in a process called “lift-off”, after which the substrate was rinsed with acetone, isopropyl alcohol (IPA), and water, in that order. After the lift-off process, the silicon wafer was cleaved into smaller pieces as shown in Figures 2.10 (a-c) below. For this step, it was important to cleave either parallel or perpendicular to the silicon plane. Finally, after cleaving the substrates to the desired sizes, they were rinsed again with acetone, IPA, and water, to remove any residues that may have deposited on them.

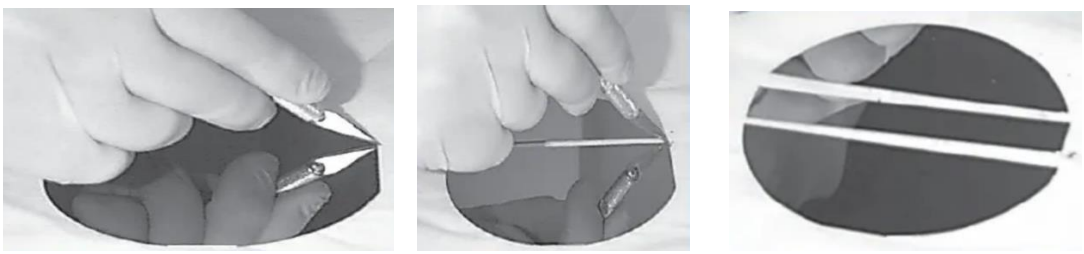

(a) (b) (c)

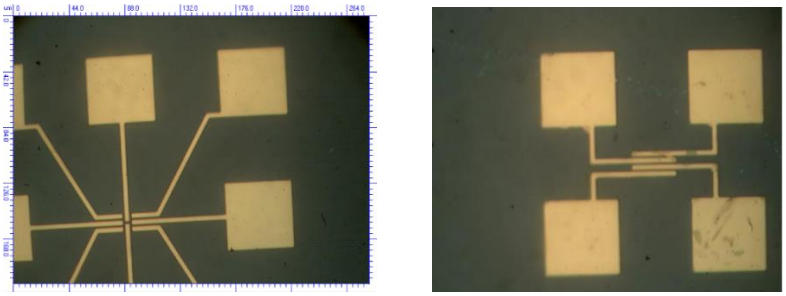

(d) (e)

Figure 2. 10 (a-c) Steps involved in cleaving silicon substrate; (d) set of 8 interdigitated gold electrodes on a silicon wafer; (e) set of 4 interdigitated gold electrodes on a silicon wafer.

Apart from the substrates, the second key component of the devices/samples studied in this work is the self-assembled metal-molecular network, which typically forms between the gold electrodes. After the synthesis and incubation of the molecular solutions, one or two 1 µL drops of the well-dispersed solutions are deposited on substrates using micropipettes and the dropped solutions are allowed to dry in air under ambient conditions. The dried molecular networks then form films which are subsequently characterized by electrical measurements.

2.3 Structural characterization methods of studying metal-molecular networks

The morphology of the self-assembled metal-molecular networks was studied using an Olympus BXFM optical microscope and Nanonics MultiView 1000 AFM with pulled glass fiber tips (10 nm nominal diameter) using the intermittent contact mode. All the measurements were conducted at room temperature under ambient conditions.

2.4 Results

AFM images (Figure 2.11) show the formation of colloidal gold nanoparticle oligomeric structures and networks after the deposition of suspensions of colloidal gold particles and thiolated molecules on the substrates, thereby depicting how the dithiol molecules can act as linkers between gold nanoparticles during self-assembly. Dense layers of molecular films comprised of aggregates of gold nanoparticles with some defect regions, can be seen between the electrodes. AFM height analyses of the oligomeric structures, shown in Figure 2.11 (a), show that the height of the structures is around 30 nm, which is consistent with the diameter of the gold nanoparticles used to fabricate the networks.

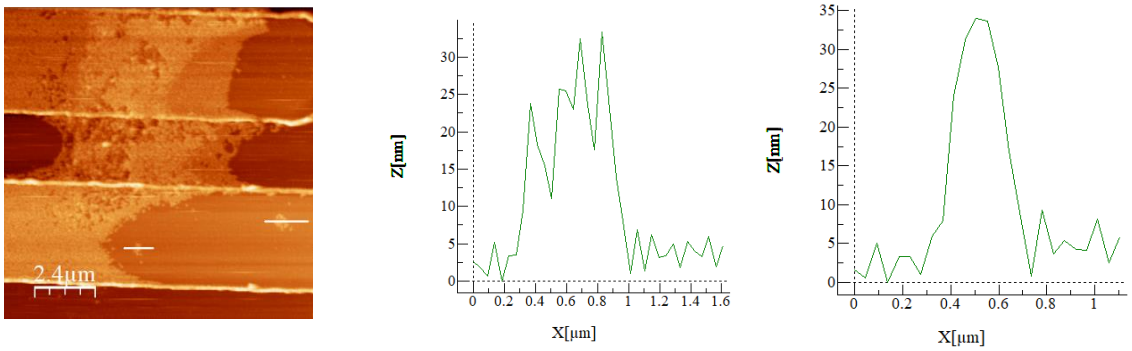

(a) (b) (c)

Figure 2. 11 (a) AFM image and height analysis of self-assembled gold nanoparticle-benzenedithiol molecular networks (N_{BDT}: $N_{particle}$ = 5:1); (b-c) AFM cross-section contours of the oligomeric structures in Figure 2.11 (a).

Oligomeric structures like the ones above tend to be made of single layers (monolayers) of dithiol-connected gold nanoparticles, however, larger internetworked films made up of multiple layers (multiplayers) of gold nanoparticles were also formed. Figure 2.12 (b), which is a zoomed in AFM image of Figure 2.11 (a) above, shows various regions of networked films formed between two electrodes. The AFM height analysis (Figure 2.12 (c)) shows that the average height of the films is about 50 nm, indicating that they are made up of layers of self-assembled gold nanoparticle films. Various defect regions/gaps in the networked films are also shown. These correspond to the points in the cross-section contours where the height rapidly decreases to about 5 nm.

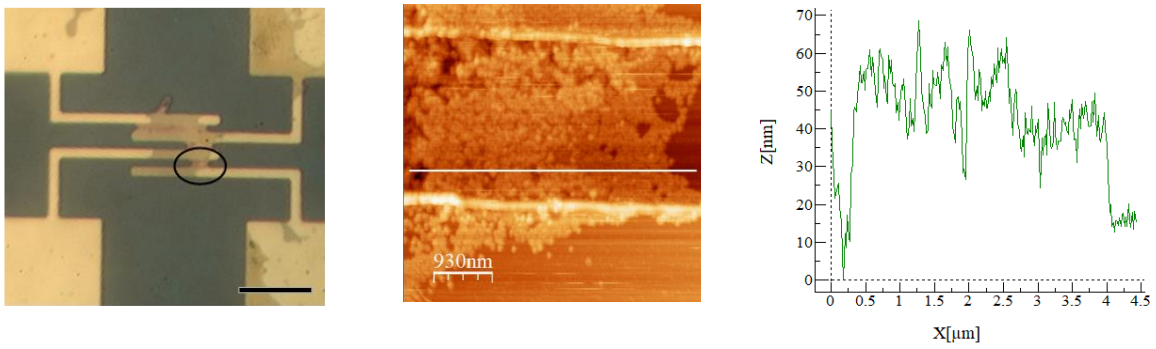

(a) (b) (c)

Figure 2. 12 (a) Optical microscope image of interdigitated gold electrodes after the deposition of gold nanoparticle-benzenedithiol network (N_{BDT}: $N_{particle}$ = 5:1) from solution (scale bar equals 15 μm); (b) Zoom-in AFM image of encircled region in (a) showing gold nanoparticle-molecular film bridging the electrodes; (c) AFM cross-section

contour of the multiplayer film in Figure 2.12 (b). White line represents the area selected for height analysis.

2.4.1 Gold Nanoparticle-benzenedithiol Networks

Gold nanoparticle-benzenedithiol molecular networks with $N_{molecule}$: $N_{particle}$ ratios, 1:1, 5:1, and 50:1, were fabricated using 30 nm colloidal gold particles.

Figure 2.13 below gives a clear picture of the structure of the colloidal gold nanoparticles used to fabricate the molecular networks studied. The AFM image of the structures shows what appears to be networks/clusters of homogeneously shaped spherical nanoparticles. AFM height/width analyses of the structures (Figure 2.13 (b-c)) show that the networks are comprised of monolayers of interconnected gold nanoparticles with individual nanoparticles having an average height of 30 ± 5 nm, and width of about 40 nm. Since the molecular networks were fabricated with 30 nm colloidal gold nanoparticles, we can assume that the structures in the AFM image are comprised of gold nanoparticles, and that we are resolving individual gold nanoparticles at some points (e.g., in Figure 2.13 (b)). The disparity between the apparent width of individual gold nanoparticles from AFM analysis and the actual width of the gold nanoparticles is probably due to AFM tip convolution and AFM imaging artifacts. Also, nanoparticle layers with heights of about 32- 34 nm probably consist of gold nanoparticles which have been functionalized by thiols.

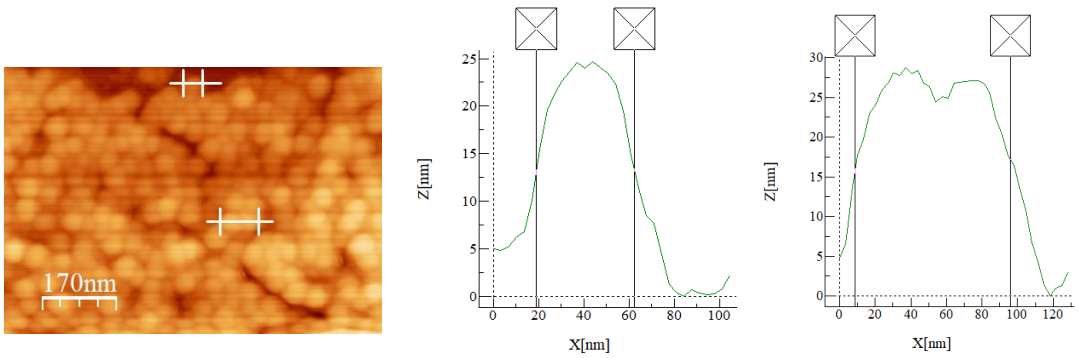

(a) (b) (c)

Figure 2. 13 (a) AFM image of self-assembled gold nanoparticle-benzenedithiol molecular networks (N_{BDT}: $N_{particle}$ = 1:1); (b-c) AFM cross-section contours of the structures in Figure 2.13 (a). Figure 2.13 (b) shows the cross-section of an individual gold nanoparticle while Figure 2.13 (c) shows the cross-section of two nanoparticles fused together, likely by thiol molecules.

As mentioned earlier, gold nanoparticle-benzenedithiol molecular networks, with $N_{molecule}$: $N_{particle}$ ratio = 5:1, were fabricated using 30 nm colloidal gold particles. Figure 2.14 (a) shows the optical image of the networks; the gold electrodes are bridged by a thin film of metal-molecular networks. AFM images of the circled region in Figure 2.14 (a) (Figures 2.14 (b-c)) show the structure of the molecular networks as being comprised of spherical gold nanoparticles that are densely packed in some areas to form agglomerates or clusters and loosely connected in others. The bright spots in Figure 2.14 (c) are likely made up of dense aggregates of nanoparticle multiplayers (topography analysis shows that the bright spots are about 70 nm high and 200 nm wide).

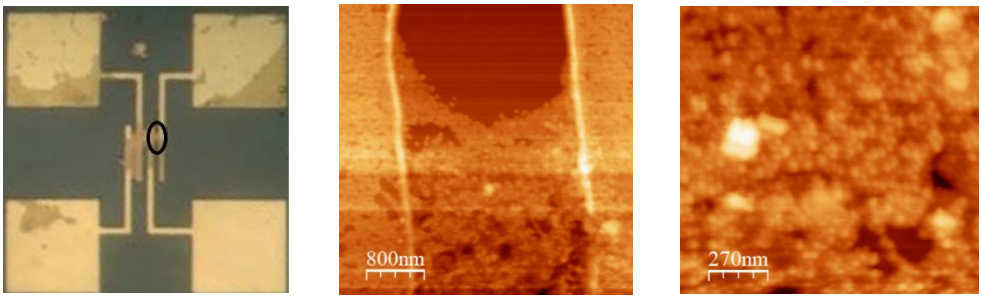

(a) (b) (c)

Figure 2. 14 Images of self-assembled gold nanoparticle-benzenedithiol molecular networks with $N_{molecule}$: $N_{particle}$ ratio = 5:1 (a) Optical image of networks; (b-c) AFM images of networks.

Defects, loose packing and clustering of nanoparticles were evident in some samples. For example, in the control sample shown in Figure 2.15 (a) below, made without any thiol molecules, loose packing of the colloidal gold nanoparticles is evident. Essentially, the molecular "glue" that directs the self-assembly process of the networks is missing in this case, thereby leading to increased defect regions in the molecular networks [76]. For comparison, AFM images of gold-benzenedithiol molecular networks with $N_{molecule}$: $N_{particle}$ = 1:1, and 5:1 are also shown (Figure 2.15 (b), and (c), respectively) indicating fewer defect regions and better packing of the gold nanoparticles. Gold-benzenedithiol molecular networks with $N_{molecule}$: $N_{particle}$ = 50:1, however, had many defect regions, thus suggesting that there is an optimal $N_{molecule}$: $N_{particle}$ for forming well-interconnected metal-molecular networks, below or above which, loose packing of the nanoparticles will be observed.

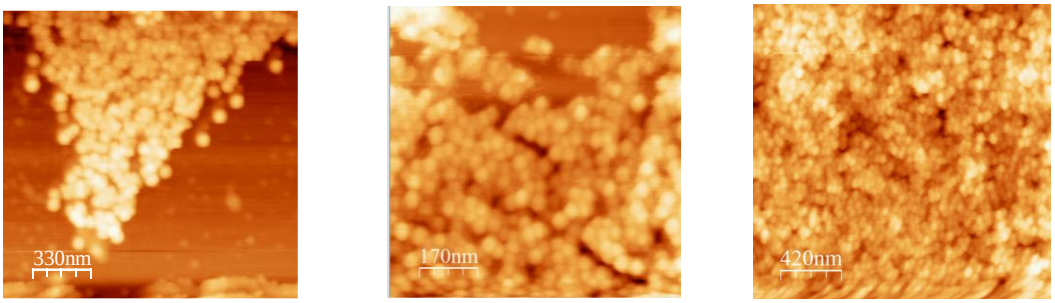

(a) (b) (c)

Figure 2. 15 AFM image of gold nanoparticle network (a) made without molecules and deposited on SiO_2 substrate. Loose packing and defects are likely caused by the lack of strong particle coupling due to absence of thiol molecules (adapted from Ref. 73); (b) gold-benzenedithiol molecular network with $N_{molecule}$: $N_{particle}$ = 1:1; (c) gold-benzenedithiol molecular network with $N_{molecule}$: $N_{particle}$ = 5:1.

In addition to the proposed mechanism of formation of ordered molecular networks in this study (thiol molecules acting as linkers between gold nanoparticles), several other possibilities for benzenedithiol-gold nanoparticle bonding exist. From previous studies, the adsorption behaviour of 1,4-benzenedithiol on colloidal gold varied depending on the concentration of 1,4-BDT in the solution: Both flat/lying down orientations of the BDT species (at lower surface coverage) and perpendicular/upright orientations (at higher surface coverage) were observed by means of surface-enhanced Raman scattering (SERS) [77], [78]. Essentially, if the concentration of thiol molecules was sufficient to form dense packing, more upright orientations of the BDT molecules were observed [77], [78]. This could also explain the changes in the morphologies of the molecular networks on modifying the thiol molecule: gold nanoparticle concentrations.

2.5 Conclusion

The focus of this chapter is on the fabrication and structural characterization of metal-molecular networks. Metal-molecular networks with an intermediate number of molecules were fabricated using the solution-based self-assembly method, which allows for the tailorability of the networks' topographies by varying the concentration of dithiol molecules used in the solution. The synthesis method employed in fabricating our molecular networks resulted in networked aggregates of gold nanoparticles interconnected by a few dithiol molecules, which could potentially serve as components in future molecular circuits. Therefore, the solution-based self-assembly fabrication method is believed to be a promising route for implementing molecular circuits because of its capability to synthesize large numbers of nanoscale structures with different topographies with relative ease and low cost.

Post fabrication, the topographies of the molecular networks were studied using optical microscopy and AFM, and the networks were found to be constituted of various types of nanoparticle layers (monolayers and multiplayers). Variations in the networks' topographies were also observed by varying the ratio of molecules to gold nanoparticles during the synthesis of the networks.

Chapter 3 Electrical Characterization of Self-Assembled Metal-Molecular Networks with tunable metal NP: molecule ratios

3.1 Introduction to molecular electronic devices and characterization tools

Since the inception of molecular electronics in the 1970s, various research groups have demonstrated the suitability of molecules and molecular units as electronic device components such as resistors, diodes, transistors, and switches.

The electronic transport properties of these molecular units have been extensively probed to evaluate their suitability for nanoelectronic circuit applications.

Kuhn and Mann conducted conductivity measurements on LB molecular films of cadmium salts of fatty acids sandwiched between metal electrodes, and the results (Figure 3.1) showed that conductivity decreased exponentially with increasing length of the molecules, thereby implying the occurrence of electron tunneling through organic monolayers [26].

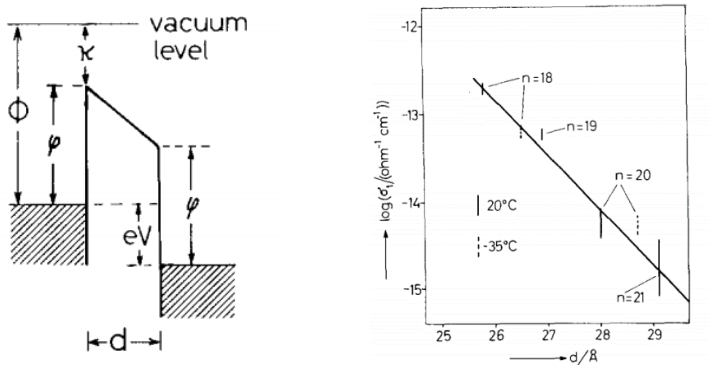

(a) (b)

Figure 3. 1 (a) Idealized potential barrier between similar electrodes separated by a fatty acid monolayer with a biased voltage; (b) Measurements of the low-bias tunneling conductivity (σ_t) vs. the distance, d between the electrodes in

(Aluminium)Al/*S(n)*/Mercury*(*Hg) junctions. Here, *S(n)* stands for monolayers of Cd salt of fatty acid $CH_3(CH_2)_{n-2}COOH$ with different lengths. The solid line is a linear fit to the experimental data (adapted from Ref. 26).

In addition to resistance, discussed above, another electrical property that has been measured in molecular units is rectification. Figure below shows the schematic of a molecular junction and corresponding *I*-*V* characteristics of a molecular diode made using oligomers of thiopene-1,1-dioxide (TDOn). Rectification ratios as high as 200 were obtained for voltages of about 370 mV [29].

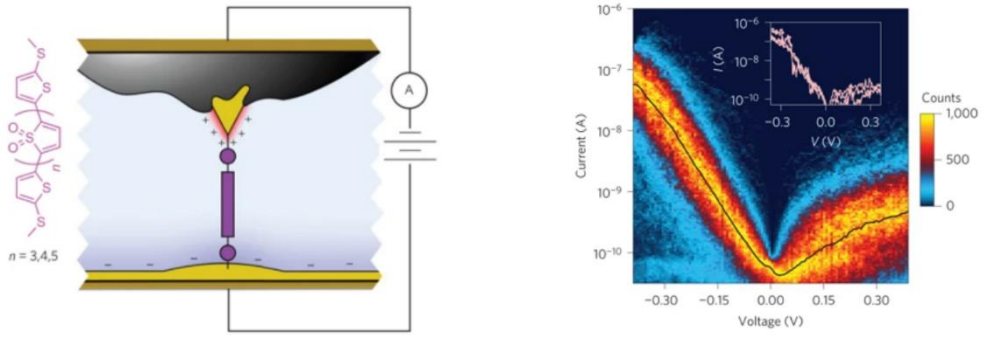

(a) (b)

Figure 3. 2 (a) TDOn molecular structure and schematic of the molecular junction; (b) Absolute current versus voltage histogram for TDO5 in propylene carbonate solvent. Inset: Examples of exceptionally rectifying junctions. (adapted from Ref. 29).

Additionally, experimental work demonstrating hysteretic and bistable behaviour in (1,5-dithiacyclooctane 1-oxide bis(pentaamine-ruthenium (II)) was conducted in 1991, suggesting possible applications of this molecule in memory and digital electronic devices [30]. The hysteretic behaviour of the system could be accounted to switching from the mixed-valence state to the isomeric alternative via electron transfer from redox [79].

Memory and logic applications have also been demonstrated using molecular computing devices. For example, Chen and his group designed a crossbar circuit comprising of a monolayer of rotaxane molecules sandwiched between an array of platinum and titanium nanowires; and employed the crossbar circuits in memory and logic applications [32].

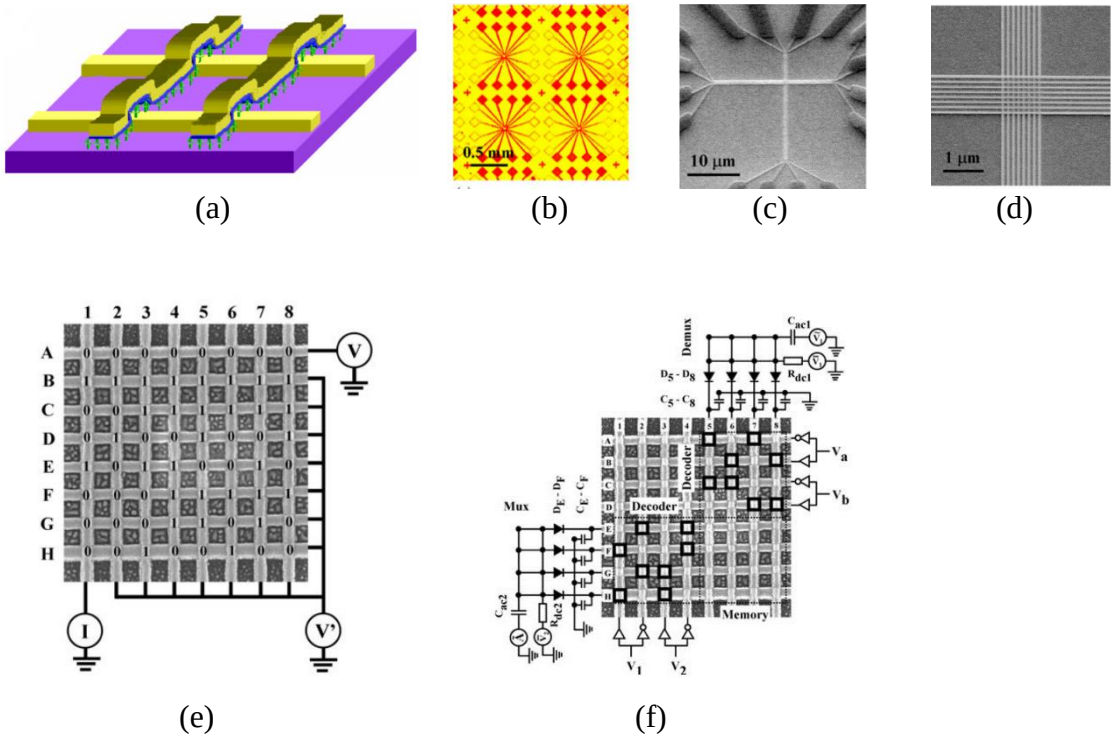

(a) (b) (c) (d)

(e) (f)

Figure 3. 3 (a) Schematic representation of the crossbar circuit structure; (b) An optical microscope image of an array of four test circuits; (c) An SEM image showing two mutually perpendicular arrays of nanowires connected to their micron-scale connections; (d) SEM image showing two sets of nanowires crossing each other in the central area; (e) The crossbar as a 64-bit random access memory; (f) The crossbar as a combination of a 4 × 4 demultiplexer, 4 × 4 memory and a 4 × 4 multiplexer. (adapted from Ref. 32).

The molecular transistor is an invaluable nanoelectronic circuit device with potential switching applications. Historically, molecular transistors were fabricated using LB films of conducting polymers and oligomers [80] or three-terminal arrays of sandwiched

electrodes [81], however, with recent technological advancements, research groups began to fabricate transistors out of single molecules (single-molecule transistors) [33], [34].

In 2009, Reed and his group constructed molecular transistors by connecting individual molecules to source and drain electrodes with a bottom-gate electrode in the FET configuration (Figure 3.4 (a)) [33]. In the molecular transistors, the transport current was controlled by directly modulating the energy of the molecular orbitals of a single molecule by electrostatic gate control [82]. Figures 3.4 (b-c) show the transport characteristics of the gold-octanedithiol-gold (Au-ODT-Au) junction formed in this manner [34].

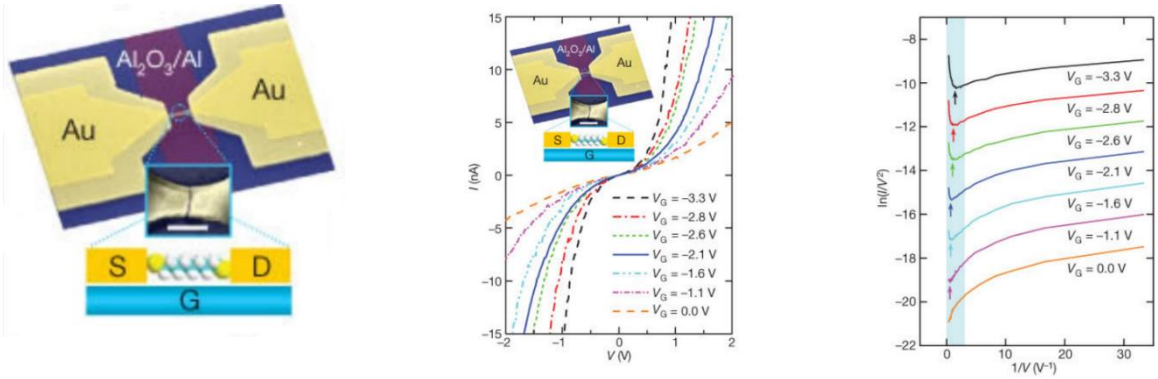

(a) (b) (c)

Figure 3. 4 (a) Device structure and schematic of the Au-ODT-Au junction; (b) *I-V* curves measured for different values of V_G. Inset shows the device structure and schematic. S, source; D, drain; G, gate. Scale bar, 100 nm; (c) Fowler-Nordheim plots corresponding to the *I-V* curves in b (adapted from Ref. 34).

Certain characterization tools such as scanning probe microscopy and break junctions have been invaluable to molecular electronics research. SPM techniques such as AFM, and STM have been effectively used to characterize various molecules and films.

Various adaptations to the AFM have been invented to measure various electronic properties (e.g., electrostatic forces, resistances, capacitances etc.) of nanoscale materials,

while simultaneously generating high resolution images of the samples. Conducting-probe AFM (CP-AFM) is one of such adaptations in which a conducting probe, in direct contact with the sample, is used to measure the *I-V* characteristics and resistance of the sample, by applying a voltage between the conducting probe and a fixed electrode and recording the current obtained at various points in the sample [51].

Frisbie and his co-workers used CP-AFM to study the *I-V* characteristics of very thin crystals of a p-type semiconducting thiopene oligomer, sexithiophene, or 6T [51]. Figure 3.5 (b) shows an AFM tomograph of a 6T crystal contacted by a microfabricated Au wire on SiO_2. Five points on the crystal, each an increasing distance from the wire, were selected to make point-contact *I-V* measurements [51]. The points are labelled in Figure 3.5 (b) and their resulting *I-V* traces, which show decreasing current with increasing wire-probe distance, are shown in Figure 3.5 (c). This observation is expected as the resistance of the crystal would increase with probe-wire separation [51].

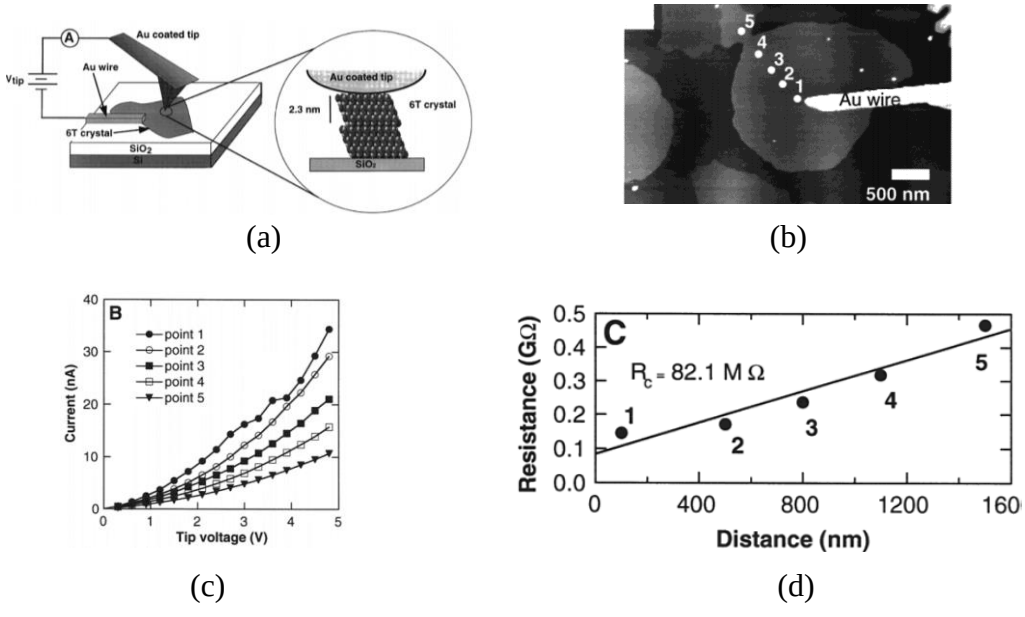

Figure 3. 5 (a) Schematic of a typical point-contact CP-AFM experiment; (b) tapping mode AFM image of a 6T crystal. The locations of five point-contact *I-V* measurements

are labelled; (c) Point-contact *I-V* characteristics obtained by CP-AFM at points 1-5 labelled in (b); (d) Resistance versus probe-wire separation distance. The intercept gives a contact resistance R_c = 82 M Ω (adapted from Ref. 51).

The break junction is another significant invention that greatly accelerated molecular electronics research. It allows for the measurement of conductance of molecules bridged between electrodes.

Bourgoin and his group used the MCBJ technique to investigate the electronic transport properties of bisthiolterthiophene 2.5”-bis(acetylthio)-5.2’5’.2”-terthienyl (T3) and observed that switching between different kinds of *I-V* curves could be induced by varying the distance between the two metallic (gold) electrodes [52]. T3 molecules were self-assembled on gold electrodes formed using the break junction technique by immersing the suspended junction in a droplet of a 5×10^{-4} M solution of T3 in trichloro-1,1,1,-ethane and allowing the solvent to evaporate. Finally, the bridge gap was reduced using a piezoelectric fine adjustment of the driving rod until a non-zero conduction was detected [52]. Figure 3.6 (a) shows the process of making the metal-molecule-metal junction, while the *I-V* characteristics and switching behaviour for different nanogap dimensions are shown in Figure 3.6 (b).

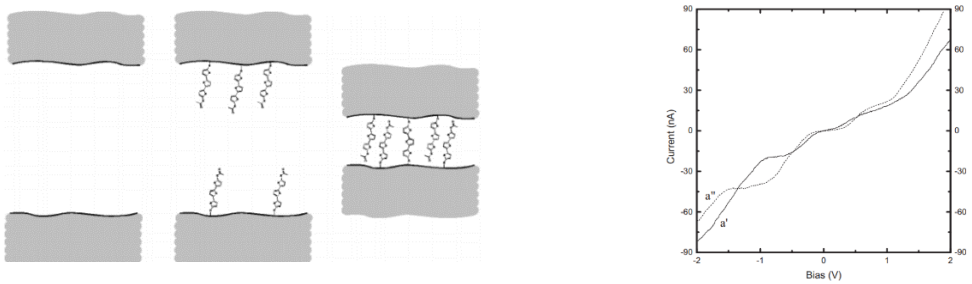

(a) (b)

Figure 3. 6 (a) Experimental setup for fabricating metal-molecule-metal junction: top and bottom gold electrodes are separated by breaking the junction (left), T3 molecules are

adsorbed onto them (middle) and the electrodes are brought closer to allow *I-V* measurements (right) on a single or a few molecules; (b) *I-V* curves recorded (a') before and (a") after reduction of the inter-electrode spacing by approximately 0.4 nm. Both *I-V* curves were obtained by averaging over 5 voltage sweeps (adapted from Ref. 52).

3.2 Two-terminal electrical characterization (I-V measurements)

Current-voltage *(I-V)* data was obtained using a Janis probe station with tungsten tips connected to an electrical characterization system (Keithley 4200-SCS). Various types of measurements ranging from low voltage, high voltage to cyclic voltammetry measurements were conducted using the Keithley system to probe the molecular networks.

3.2.1 Experimental setup/ equipment used for I-V measurements

The experimental setup for conducting *I-V* measurements comprised of a Janis probe station, Keithley electrical characterization system and metal-molecular networks deposited on substrates with interdigitated electrodes. The substrates were mounted on the Janis probe station, and tungsten probes were used for two-terminal electrical measurements of the metal-molecular networks by contacting the substrate pads at various locations where the metal-molecular networks were deposited between interdigitated electrodes.

Figure 3.7 below shows a 3D sketch of the devices fabricated in this study. Specifically, shown here is the 8-pad configuration wherein the substrate is divided into sets of eight

interdigitated electrodes with eight gold contact pads each. The 4-pad configuration (with the substrate divided into groups of four interdigitated electrodes) was also used for probing many of the samples in this study. The substrates for *I-V* measurements consisted of photolithographically patterned gold electrodes with a thin adhesion layer on a silicon wafer substrate coated with a 100 nm layer of silicon dioxide. Metal-molecular networks were deposited on these substrates and probed using electrical characterization techniques.

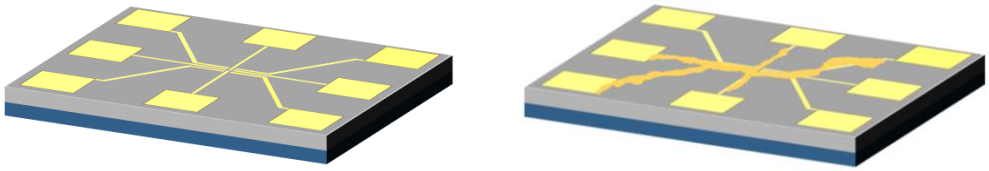

(a) (b)

Figure 3. 7 3D sketch of device sandwich structure used for probing the metal-molecular networks with silicon substrate, silicon oxide layer on top, and gold electrodes etched on the silicon oxide layer (a) device without metal-molecular network deposited on it; (b) device showing metal-molecular networks deposited across the interdigitated electrode fingers.

3.2.2 Low-voltage *I-V* measurements

Low-voltage *I-V* measurements were conducted on gold nanoparticle-benzenedithiol and gold nanoparticle-nonanedithiol networked films using linear voltage sweeps with bias voltages of ±0.3 V. The gold-benzenedithiol molecular networks studied displayed nonlinear *I-V* characteristics in some cases, however, they typically showed linear *I-V* characteristics at low biases. The gold-nonanedithiol molecular networks, however,

displayed almost equal distributions of linear and nonlinear *I*-*V* characteristics at low biases.

3.2.3 High-voltage *I*-*V* measurements

High-bias *I*-*V* measurements were conducted on gold nanoparticle-benzenedithiol networked films using voltage sweeps cycled between 0 and 5 V. Interesting nonlinear behaviours such as hysteresis and negative NDR were observed in the molecular networks when cycling voltages to very high values, and the nonlinearities were more pronounced in gold-benzenedithiol molecular networks with higher percentages of molecules.

3.2.4 Cyclic voltammetry measurements

Cyclic voltammetry (CV) measurements were conducted on gold-benzenedithiol molecular networks at high biases by sweeping voltage from -5 to +5 V (i.e., from 0 to 5 V and then back to 0 V; and from 0 to -5 V and then back to 0 V). Hysteretic and NDR behaviours were observed in the gold-benzenedithiol molecular networks upon cycling between very high voltages (-5 V to +5 V), particularly in samples with a higher concentration of benzenedithiol molecules.

3.3 Results and Analysis

3.3.1 Gold-benzenedithiol molecular networks

The results of the electrical characterization of gold-benzenedithiol molecular networks with various molecule: AuNP ratios fabricated using 30 nm colloidal gold nanoparticles are discussed in this section. For samples with molecule: AuNP = 1:1; the measured current magnitude at low bias typically fell in the nA - μA range, with linear *I-V* characteristics being a common theme. The optical image shows a thick gold-coloured film deposited across the electrode fingers. The *I-V* plot shown in Figure 3.1(b) corresponds to the film deposited between the uppermost electrode fingers (as represented in the schematic in Figure 3.8(a)).

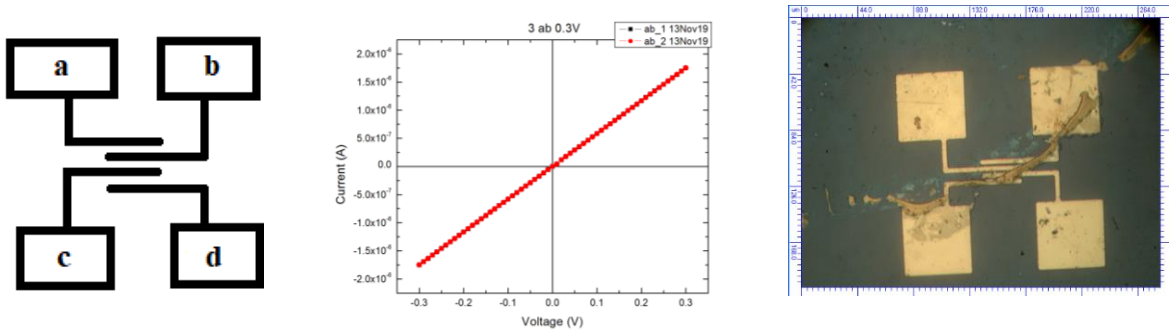

(a) (b) (c)

Figure 3. 8 (a) Schematic diagram of the electrode arrangement; (b) *I-V* plot; (c) Optical image of gold-benzenedithiol molecular network with molecule: AuNP = 1:1.

Similarly, for high-bias electrical measurements of metal-molecular networks with 1:1 molecule: AuNP ratios, most of the samples showed linear *I-V* behaviour, with very few exhibiting nonlinearities in their *I-V* curves. Figures 3.9 and 3.10 below show the high-bias *I-V* plots and corresponding optical images of gold-benzenedithiol molecular networks with 1:1 molecule: AuNP ratio.

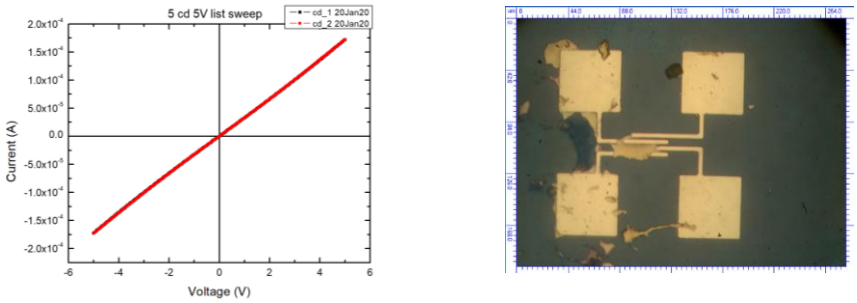

(a) (b)

Figure 3. 9 (a) *I-V* plot; (b) Optical image of gold-benzenedithiol molecular network with molecule: AuNP = 1:1.

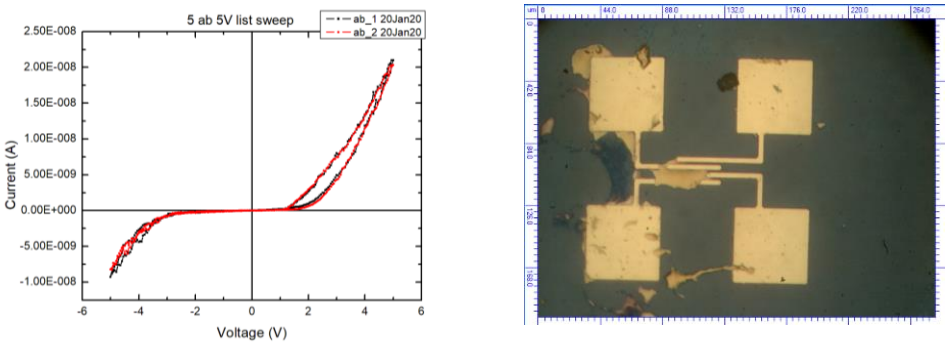

(a) (b)

Figure 3. 10 (a) Schematic diagram of the electrode arrangement; (b) *I-V* plot of gold-benzenedithiol sample; (c) Optical image of gold-benzenedithiol molecular network.

For molecular networks with molecule: AuNP = 5:1, the measured current magnitude at low bias typically fell in the nA - pA range, with linear *I-V* characteristics being prevalent. At higher biases, however, nonlinearities were observed in the *I-V*s of many measured samples. Figure 3.11 below shows the *I-V* plots (both at low and high biases) and corresponding optical image of a gold-benzenedithiol molecular network with 5:1 molecule: AuNP ratio. The optical image shows a narrow rectangular film deposited between the middle two electrode fingers. Figure 3.11 (a) shows a linear *I-V* plot

corresponding to the low-bias measurement of the sample while Figure 3.11 (b) shows a nonlinear plot with hysteretic behaviour corresponding to the high voltage CV measurement of the same film.

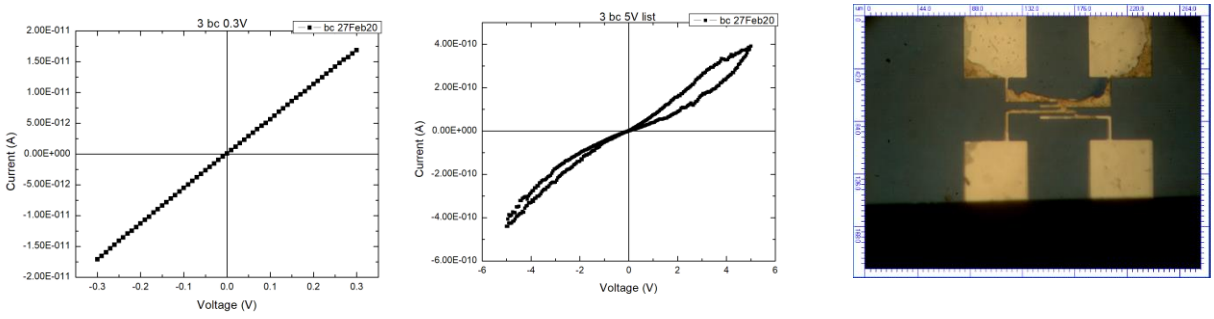

(a) (b) (c)

Figure 3. 11 (a) low-bias *I-V* plot; (b) high-bias *I-V* plot; (c) Optical image of gold-benzenedithiol molecular network with molecule: AuNP = 5:1.

Molecular networks with molecule: AuNP = 50:1 displayed the lowest measured current magnitudes with values typically falling in the pA range for low-bias measurements. Both linear and nonlinear *I-V* characteristics were obtained at low biases. However, some molecular networks which displayed linear *I-V* curves at low biases showed significant nonlinearities in their *I-Vs* at higher voltages. Figure 3.12 (b) shows a nonlinear plot with a pronounced NDR behaviour obtained from high bias electrical measurements of the same film.

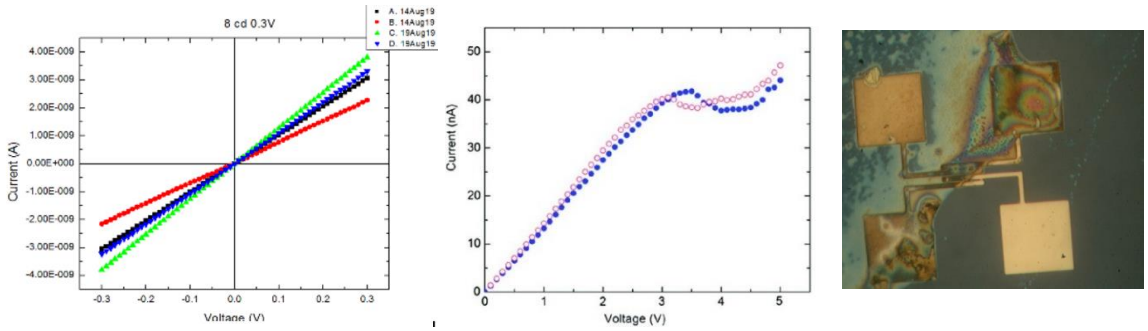

(a) (b) (c)

Figure 3. 12 (a) low-bias *I-V* plots; (b) high-bias *I-V* plots; (c) Optical image of gold-benzenedithiol molecular network with molecule: AuNP = 50:1.

In our studies, control samples were fabricated using only gold nanoparticles, without the addition of thiol molecule linkers. Specifically, control samples were made using both mixtures of ethanol and 10 nm colloidal gold nanoparticles, and mixtures of ethanol and 30 nm colloidal gold nanoparticles. Electrical characterization measurements using both low and high biases were subsequently conducted on the samples. For control samples made using 30 nm gold nanoparticles, the measured currents at low bias typically fell in the 10^{-13} A – 10^{-12} A range, and both linear and nonlinear *I-V*s were observed.

High bias measurements on control samples made using 30 nm gold nanoparticles yielded linear *I-V* characteristics, which contrasted the behaviour of gold-benzenedithiol molecular networks at higher bias. Figure 3.13 shows the *I-V* curve at high bias and optical image of a control sample.

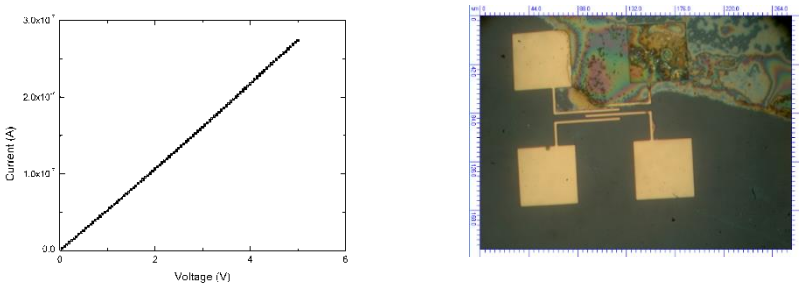

(a) (b)

Figure 3. 13 (a) Linear *I-V* plot of a control sample at high bias; (b) Optical image of a control sample.

In summary, the nonlinearities in the *I-V* curves of the gold-benzenedithiol molecular networks at higher biases became more pronounced with increasing molecule: AuNP ratio, with the control sample, consisting of only gold nanoparticles, displaying linear *I-V* behaviour at higher biases. The evolution of *I-V* characteristics as a function of N_{BDT}:$N_{particle}$ ratio in the gold-benzenedithiol molecular networks is shown in Figure 3.14 below.

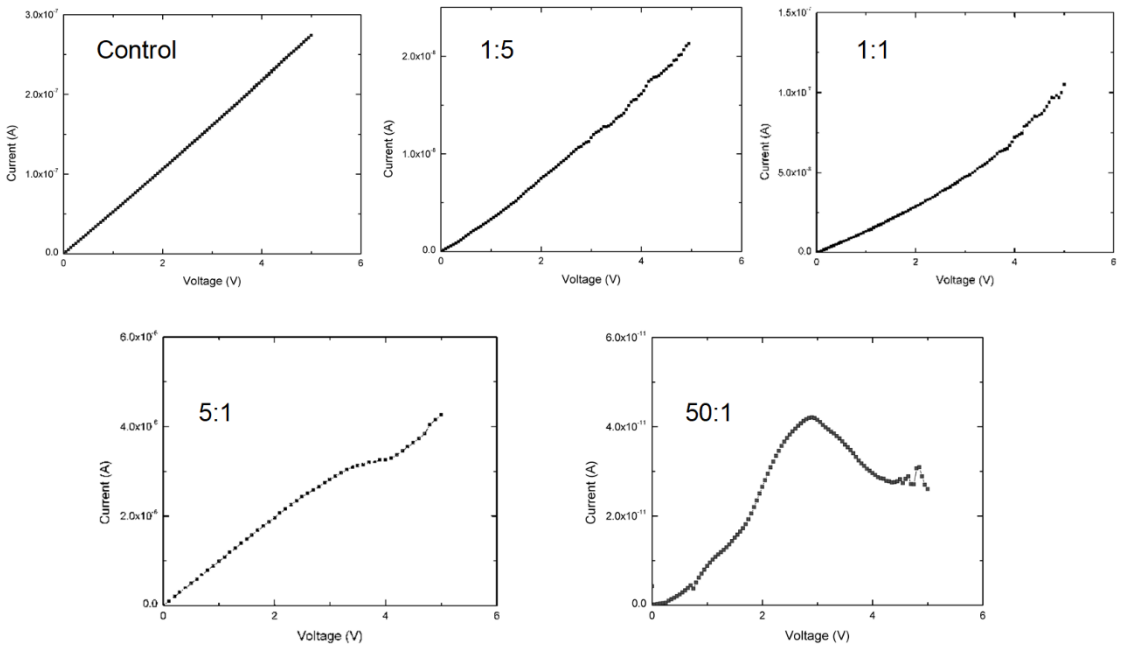

Figure 3. 14 Evolution of *I-V* characteristics of gold-benzenedithiol molecular networks as a function of N_{BDT}:$N_{particle}$ ratio (control sample consists of gold nanoparticles only) showing increase in nonlinearity and NDR appearance near 5:1. A peak-to-valley ratio of approximately 1.52 is seen for the 50:1 network sample.

3.3.2 Analysis of Experimental Data

3.3.2.1 Discussion of results

It was typically observed that the current in the molecular networks studied decreased with increasing molecule: AuNP, consistent with other works [76]. For example, in gold-benzenedithiol molecular networks with approximately the same length-to-width ratios, current was found to decrease from the μA range in 1:1 ratio samples to the nA range in 50:1 samples.

Figure 3.15 shows the low-bias *I-V* plots of gold nanoparticle-benzenedithiol molecular networks with molecule: AuNP ratios of 1:1 and 50:1, and current ranges of μA and nA, respectively, in the samples.

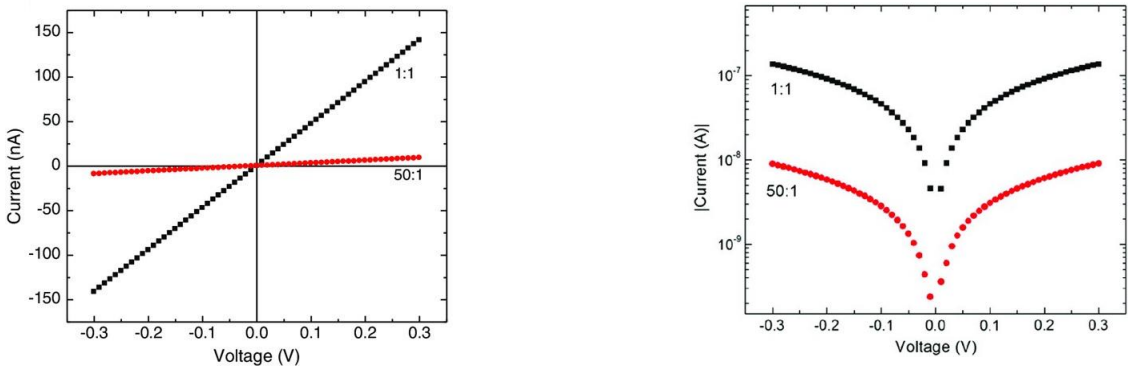

(a) (b)

Figure 3. 15 (a) *I–V* plots of 1:1 network sample (effective film dimensions ≈ 2 by 1.8 μm) and 50:1 network sample (effective film dimensions ≈ 0.9 by 0.7 μm); (b) Semilogarithmic plots of magnitude of current versus voltage for different molecule: AuNP ratios of gold nanoparticle–benzenedithiol networks.

Additionally, many gold-benzenedithiol molecular networks which had linear *I-V* characteristics at low biases displayed nonlinearities in their *I-V*s at higher biases. This behaviour became particularly pronounced in molecular networks with a higher percentage of molecules.

A probable model which explains the observed nonlinear *I-V*s at larger biases for gold-benzenedithiol molecular networks containing a higher percentage of molecules is based on tunneling transport and charge trapping. The tunneling mechanism, particularly, a transition to the field-assisted Fowler-Nordheim tunneling mechanism at higher biases (above 1V), coupled with field-assisted charge trapping/emission in metal-molecular

networks provides a plausible explanation for the observed NDR and hysteretic behaviours. In this scenario, a change in tunneling barriers at around 3-4 V could be caused by charge capture due to defects becoming active in the networks at higher biases, thereby inhibiting further injection of charge through the junction and in turn reducing the current. The opposite process, i.e., charge carrier emission, would then lead to hysteretic behaviour upon cycling the voltage [83], [84], [85]. Another possible explanation for the observed NDR could be resonant tunneling between molecular orbitals and the metal delocalized states, thereby leading to a conduction peak followed by a decrease in the tunneling current for charge carrier energies that are off resonance at higher biases [86].

3.3.2.2 Analysis of results (LTspice)

Experiments using local conducting-tip AFM showed that the gold-molecular networks displayed distinct resistance ranges depending on the type of connection being probed [76]. By sampling multiple locations on the networks, either direct gold-gold nanoparticle connections with resistances in the kΩ range, or gold nanoparticle-molecule connections with resistances in the MΩ range, were probed. The variations in resistance values observed experimentally were used to develop a linear resistor circuit model of the network's structure to analyze the low-bias behaviour of the molecular networks. Additionally, AFM images showed that defects were present in the molecular networks, and this was also accounted for in the circuit model. Consequently, the circuit model comprised of gold nanoparticle-molecule connections, gold-gold nanoparticle contacts and defects, each having unique resistance values.

LTspice, a SPICE-based simulator of electronic circuits produced by Linear Technology Corporation (LTC), was used for implementing and simulating the circuit model of the nanoparticle networks at low bias. First, a subsection of the circuit, comprising of 36 resistors to serve as a repeating unit, was built (Figure 3.16 (b)). Following this, the whole network was built by repeating the building blocks until the desired dimension of the circuit was achieved. The contact resistance between the gold electrodes and the resistors in the circuit was chosen as 0.55 Ω. The resistors in the unit cell were parameterized with unique variables, R_1 to R_{36}, such that it was possible to tune the number of molecular contacts, gold contacts and defects. A python script was used for generating a random set of variables, which determined the positions of the nanoparticles, molecular contacts, and defects.

For example, a 500 nm long by 500 nm wide network, created by repeating the 36-resistor unit cell as per the desired dimensions obtained from microscopy data, was used for simulating the gold-benzenedithiol molecular networks. The circuit model is as shown in Figure 3.16 (a) below. The resistances assigned to the various types of connections in the molecular networks are: gold-gold nanoparticle contacts, 12907 Ω; gold nanoparticle-benzenedithiol connections, 1MΩ; and defects, 1×10^{15} Ω. Other molecular networks e.g., gold-nonanedithiol and gold-hexanedithiol molecular networks were simulated by assigning the appropriate gold nanoparticle-molecule resistance where applicable.

The number of gold-molecule connections, gold-gold nanoparticle contacts and defects was varied using “random.shuffle”, a function in our Python script that is based on the Mersenne Twister pseudorandom number generator. The random variable generator assigns all the resistors in the unit cell to be one of three values: either the quantized inter-

particle contact resistance, the bezenedithiol molecule resistance, or the defect resistance, depending on the desired molecule:gold nanoparticle concentration as well as the desired percentage of defects, as shown by the configurations in Figure 3.16 (c-d). For example, a network having 50% molecular connections and no defects would be such that 18 resistor values out of the unit cell, would be set to the benzenedithiol molecule resistance, 1 MΩ, and 18 resistor values would be set to the gold-gold inter-particle contact resistance. Simulations were generally repeated 3 times with the resistor values within the unit cell being randomized each time for the desired molecule:gold nanoparticle and defect ratio [67].

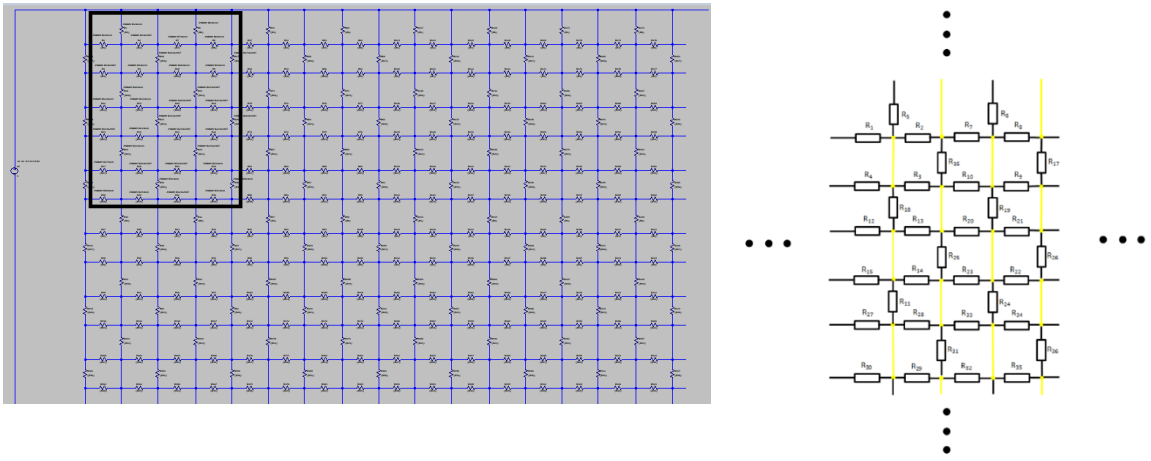

(a) (b)

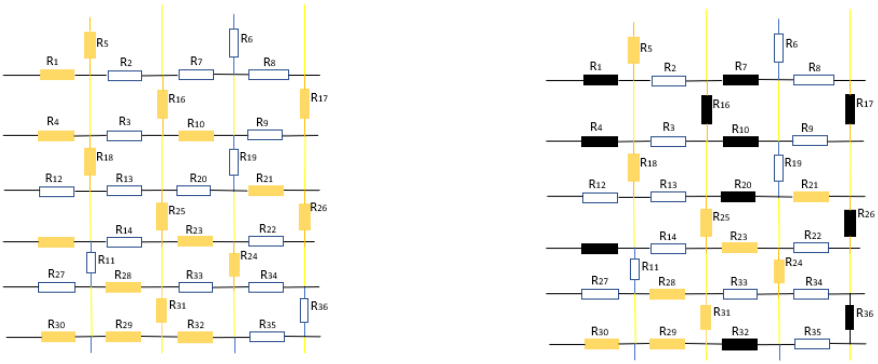

(c) (d)

Figure 3. 16 (a) Resistor network (length: 500 nm, width: 500 nm) used for circuit simulations. Black highlighted box represents the unit cell (building block of the circuit network); (b) Building block of the circuit model showing 36 resistor variables. The yellow lines represent nanoparticles, each with six nearest neighbour connections. Each resistor is assigned one of three possible values, i.e., either the gold-gold nanoparticle contact resistance, the molecule resistance, or the defect resistance; (c) Randomized unit cell configurations corresponding to 50% molecular and 0 defect connections; (d) Randomized unit cell configurations corresponding to 50% molecular connections, and 30% defects (molecules- white, gold-gold nanoparticle contacts- gold, defects- black).

Figure 3.17 below shows the result of low-bias LTspice simulations of a 500 nm by 500 nm circuit (corresponding approximately to the length/width ratios for the gold-benzenedithiol samples in Figure 3.15). Resistance ranges from about 10 kΩ (no molecules in the network) to a few MΩ (all molecular contacts in the network) were obtained from the simulations. Resistance values were typically seen to increase with an increase in the percentage of benzenedithiol molecules and defects, in agreement with experimental data (Figure 3.15). For example, circuit simulation data showed an order of magnitude increase in resistance for > 30 – 40% molecular contacts in the network. Additionally, including point defects in the circuits (> 30%) generally improved the agreement of simulation data with the experimental low-bias *I-Vs*, consistent with AFM results. For example, in the circuit simulation below, the resistance of the network with 100% molecular contacts and 50% defects is a few MΩ; this value roughly agrees with the resistance of the gold nanoparticle-benzenedithiol molecular network with molecule: AuNP ratio of 50:1 (Figure 3.15) [67].

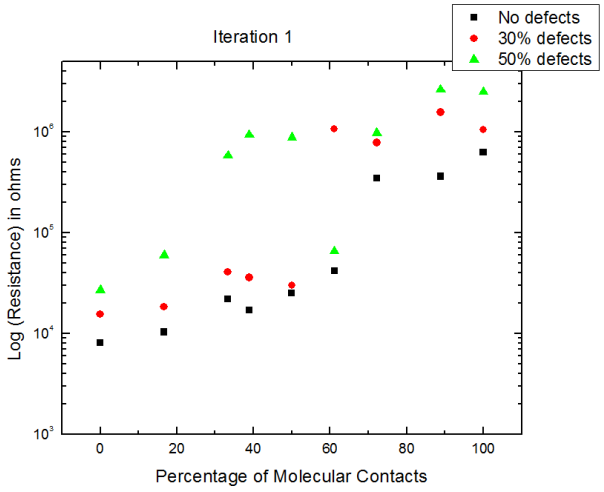

Figure 3. 17 Low-bias linear circuit simulation results for a 500 by 500 nm network: semilog plot of gold nanoparticle-benzenedithiol network resistance versus percentage of molecular connections in the circuit. Simulated resistance values with no defects (black squares), 30% defects (red circles), or 50% defects (green triangles) are shown.

Although the linear circuit model with a high percentage of defects gives a fairly good approximation to the experimental results, the circuit simulation accuracy is affected by certain factors which are omitted in the circuit modelling process. For example, parasitic contact resistances likely exist between the nanoparticles and thiol molecules but are not accounted for in the circuit model. Additionally, the circuit model assumes a monolayer network whereas in practise, the networked films are often made up of multiple layers of interconnected gold nanoparticles and thiol molecules. Irrespective of the uncertainties in the circuit simulation, the spice modelling is consistent with the measured data over a wide range of experimental conditions and serves as a guide for designing self-assembled molecular electronic circuits.

Observed nonlinearities (e.g., NDR, hysteresis and rectification) in the *I-V*s of the metal-molecular networks studied in addition to the tunability of the resistance of the molecular

networks by tuning the $N_{molecule}$: $N_{particle}$ ratio, can be harnessed in nanoelectronic circuit/ device applications such as memory, logic, switching and sensing.

The metal-molecular networks were stable over all the operating voltages (±0.3 V and ±5 V) used in this study. Low-bias measurements (±0.3 V) of samples before and after high-bias measurements (±5 V) yielded similar results. Additionally, *I-V* measurements were repeatable 98% of the time for samples which displayed linear *I-Vs*, and 90% of the time for samples with nonlinear *I-Vs*.

3.4 Applications – Random key generation and testing

3.4.1 Methods

3.4.1.1 Random key generation: Using current values or *I-V*s to assign digits

The variability of the *I-V* characteristics of the metal-molecular networks by tuning the $N_{molecule}$: $N_{particle}$ ratio can be harnessed in device applications. Specifically, in this work, nanoelectronic circuits comprised of interconnected thiol molecules and colloidal gold nanoparticles were used for hardware security applications by utilizing device level physical randomness and imperfections induced during fabrication for generating random keys. The molecular networks were deposited on substrates with eight interdigitated electrodes and two-terminal electrical measurements were conducted on the molecular networks deposited between all the electrode pairs. Electrical measurements showed variations in the resistances of the networks when different electrode pairs were probed,

and the variations in resistances between adjacent electrode pairs were used for generating arrays of bits for encryption keys.

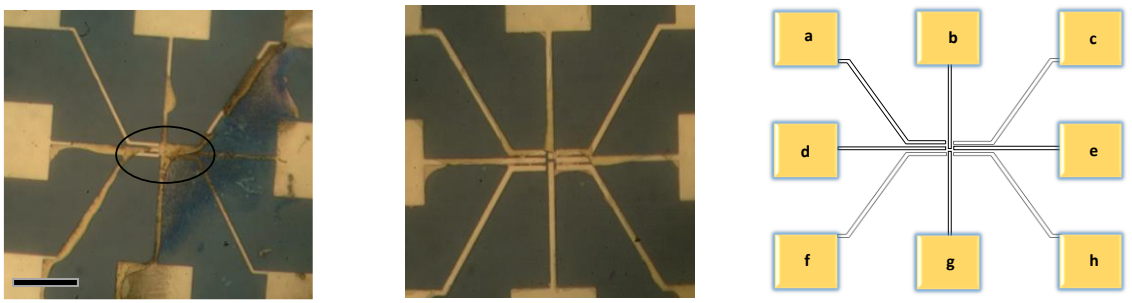

(a) (b) (c)

Figure 3. 18 (a) Optical microscope image of patterned gold electrodes after deposition of gold nanoparticle-hexanedithiol network from solution ($N_{molecule}$:$N_{particle}$ = 5:1, scale bar equals 15 μm); (b) Zoom-in optical image of an 8-pad sample; (c) Schematic of the device architecture showing multiple electrode pairs indicated by alphabets a-h.

Figure 3.18 (a) above shows the optical microscope image of the gold nanoparticle-molecular network self-assembled between a portion of the interdigitated electrodes, and Figure 3.18 (c) shows a schematic of the device architecture showing multiple electrode pairs that can be probed for two-terminal electrical characterization.

Several samples using different dithiol molecules (benzene, hexane, and nonane) and $N_{molecule}$: $N_{particle}$ ratios were fabricated for electrical characterization. Typically, for molecular networks probed with low biases (up to 0.5 V), the obtained *I-V*s were linear. The dynamics of self-assembly lead to device level randomness and imperfections, which in turn culminated in the unique properties of the self-assembled molecular networks and variations in the measured resistance when different electrode pairs were electrically probed.

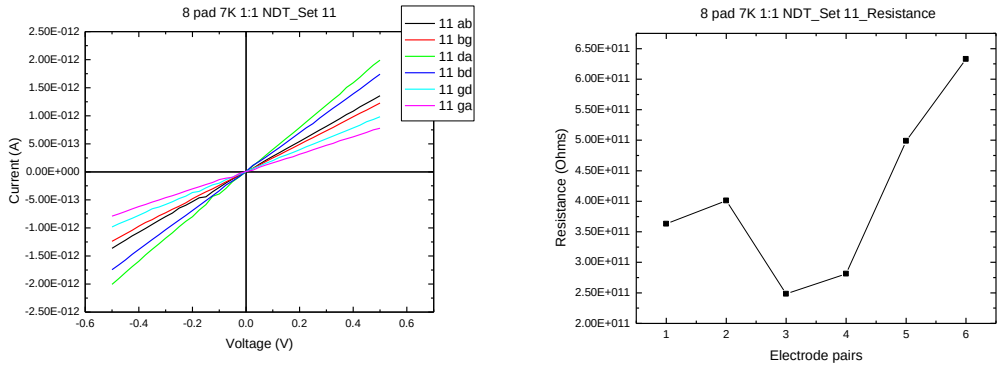

(a) (b)

Figure 3. 19 (a) *I-V* curves of gold nanoparticle-nonanedithiol networked films with $N_{molecule}$: $N_{particle}$ ratio of 1:1; (b) Resistance profile built by calculating resistance values at V = 0.5 V for different adjacent electrode pairs.

Figure 3.19 shows the *I-V* curves measured for different electrode pairs and the corresponding resistance profile of gold-nonanedithiol networked films with $N_{molecule}$: $N_{particle}$ ratio of 1:1. The various electrode pairs show variations in the measured currents, depending on the size of the networked film formed between the electrodes, the type of molecules used in the network, and also on the ratio of molecules to particles in the networks.

Arrays of bits were generated by comparing the adjacent resistances calculated at a fixed voltage, V = 0.5 V plotted as a function of the electrode pair number (N). In all cases, if the measured resistance between an electrode pair is greater than the resistance of the next pair, an integer value of "1" is assigned, and a value of "0" is assigned if the reverse is the case. This process results in the generation of binary keys of various lengths depending on the number of electrode pairs measured for each sample.

3.4.1.2 Random key testing: Testing using NIST and Hamming tests

After generating the binary keys, the randomness of the bits was evaluated using testing methodologies like the NIST statistical randomness test suite [87], and the Hamming distance metric [88], [89].

The Hamming distance metric for testing binary keys takes into cognizance the Hamming distance, or the total number of changes required to make two bit streams of the same length equal. In cases where the two keys are obtained from repeated measurements on the same set of electrode pairs, we calculate the Hamming intra-distance value. Typically, measurements made on the same set of electrode pairs more than once showed good repeatability, hence leading to very low intra-distances. However, if the keys are from different samples, we calculate the Hamming inter-distance value. For example, using the binary key generation method discussed earlier on gold-nonanedithiol molecular network samples with $N_{molecule}$: $N_{particle}$ ratios of 1:1 and 50:1, respectively, the following 16-bit binary keys were generated: 0101001101100100 and 1011101000110110. On comparing these two arrays of bits, eight bit changes are required to make the two bit streams equal, hence the resulting inter-Hamming distance, H^{bin}_{inter} (key 1 – key 2) = 0.5.

In addition to the Hamming distance metric, NIST tests were also used to evaluate the generated keys for randomness. The NIST Statistical Test suite is a group of 15 tests that were developed by the National Institute of Standards and Technology for evaluating the randomness of random and pseudorandom number generators for cryptographic applications [87].

After generating the binary sequences, they can be stored in a text file for evaluation using the NIST test suite. Testing with the NIST suite requires the use of a terminal such as

Cygwin. After installation of the NIST test suite, and the terminal, we were required to enter the directory which contains the NIST tests using the terminal and invoke the makefile. Following this, the NIST statistical test suite was invoked using the keyword "assess" followed by the bit stream length. Subsequently, a series of menu prompts will be displayed in order to select the data to be analyzed and the statistical tests to be applied. Once testing is completed, the empirical results can be found in the "experiments" folder, which contains details about the proportion of sequences that passed/failed all the tests run and their p-values.

3.4.1.3 LTSpice simulation

The LTspice circuit model outlined in 3.2.4 was also used here in generating binary sequences and analyzing the experimental data. The only difference in the circuit model used for generating binary sequences is the electrode configuration. In this case, the networks were probed at different locations using 8 electrodes, to simulate the electrical measurements being conducted experimentally on the metal-molecular networks deposited on 8-pad substrates. The molecular, gold nanoparticle, defect, and electrode contact resistances were set to $1e^{6}$ Ω, 12907 Ω, $1e^{15}$ Ω, and 0.55 Ω respectively, and the applied bias was 0.5 V. The bit streams could also be extended to form longer, more secure keys by combining smaller bit streams together.

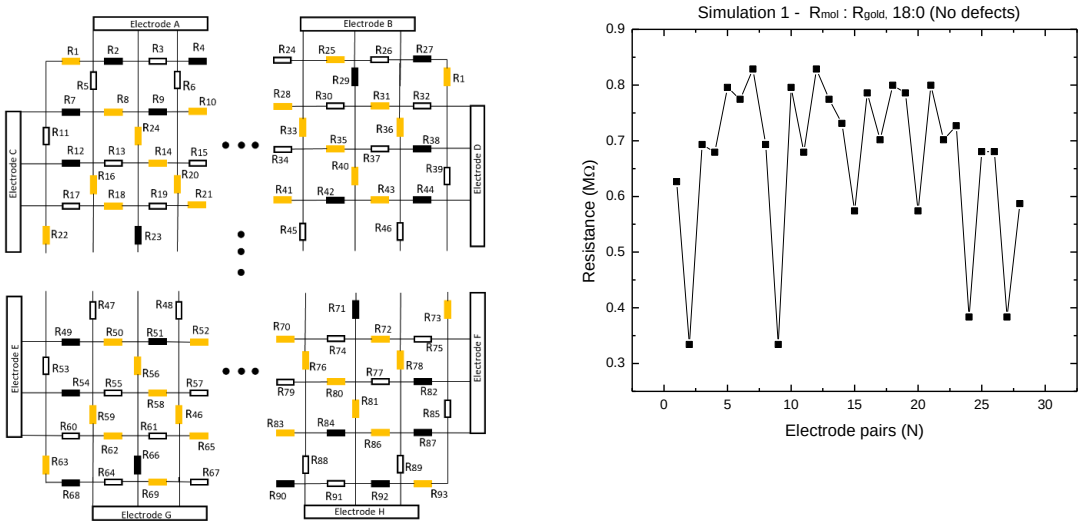

(a) (b)

Figure 3. 20 (a) Schematic of the LTspice circuit used for simulations; (b) Resistance profile built by calculating resistance values at V = 0.5 V for different adjacent electrode pairs in a circuit with 100% molecular contacts and no defects.

Figure 3.20 (a) shows the schematic diagram of the LTspice circuit used for generating random keys. The resistance values were assigned to elements in the circuit depending on the desired percentage of molecules, gold nanoparticles and defects. Figure 3.20 (b) shows the results of low-bias circuit simulations of a network comprising of 100% molecular contacts and no defects. The resistance profile shows a variation in resistance values between adjacent electrode pairs, and these variations were used for generating bits: “1” was assigned if the calculated resistance between an electrode pair was greater than the resistance of the previous pair, and a value of “0” was assigned if the reverse is the case.

3.4.2 Results and Analysis

3.4.2.1 Random key generation analysis

The generated array of binary keys can span to various lengths (e.g., 8-, 16-, 32-, 64-, 100-bits etc.) depending on the number of electrode pairs measured for each sample. The resistance profiles and corresponding 16-bit keys generated using the experimental data for gold-nonanedithiol molecular networks with $N_{molecule}$: $N_{particle}$ of 1:1 and 50:1, respectively, are shown in Figure 3.21 below.

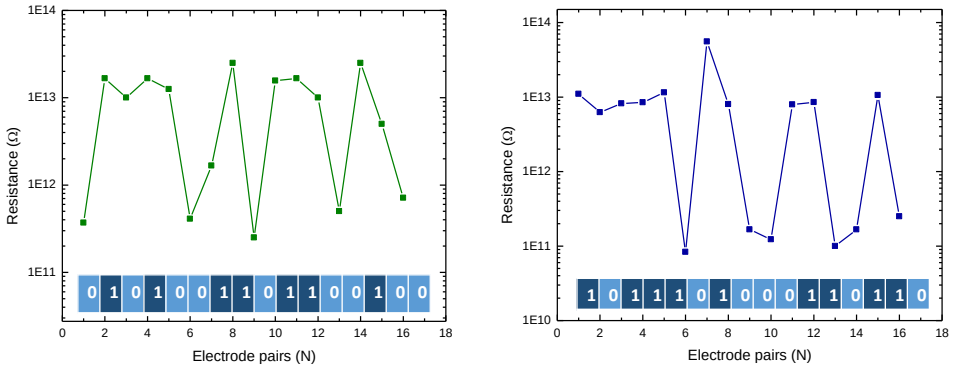

(a) (b)

Figure 3. 21 Resistance profiles built by calculating resistance value at V = 0.5 V for different electrode pairs measured for N_{NDT}: $N_{particle}$ ratio of (a) 1:1 and (b) 50:1. Insets show the 16-bit random keys generated by comparing the values of resistances between adjacent electrode pairs.

On comparing the two arrays of binary keys, 8 bit changes out of 16 bits are required to make the two bit streams equal, hence the resulting inter-Hamming distance is H^{bin}_{inter} (key 1 – key 2) = 0.5. Previous work in this field suggests that an inter-Hamming distance of 0.5 or closer indicates that the two keys are random, uncorrelated and unclonable [90], [91].

Similarly, a 100-bit key was generated using experimental data obtained from gold-nonanedithiol networked films with $N_{molecule}$: $N_{particle}$, 1:1. The bit stream, 01110101101101011101010111000110011111011001010110010010110011011110010111001010001111010101001010101, was generated by comparing resistances between adjacent electrode pairs. Figure 3.22 shows the corresponding resistance profile for the gold-nonanedithiol networked films.

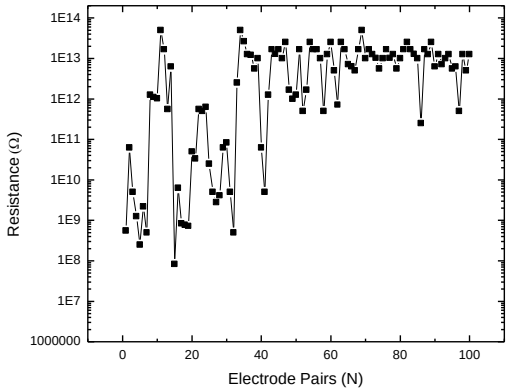

Figure 3. 22 Resistance profile built by calculating resistance values at V = 0.5 V for different electrode pairs measured for N_{NDT}: $N_{particle}$ ratio of 1:1.

The randomness of the 100-bit key was evaluated using the NIST statistical test suite, and the results (p-values) of the various tests conducted on the key are shown in Table 3.1 below.

Table 3. 1 : National Institute of Standards and Technology (NIST) test results for 100-bit key.

Statistical Test **Bit Stream (100 bits)**	**Frequency**	**Block Frequency**	**Cumulative Sums test**	**Non-periodic template matching test**	**Serial test**	**Approximate Entropy**

0111010 1101101 0111010 1011100 0110011 1101100 1010110 0100101 1001101 1110010 1110010 1000111 1010101 0010101 01	0.230139	0.904131	0.387010	1.0000	0.498961	0.024511

According to the NIST manual [87], if the p-value is < 0.01, then one can conclude that the sequence is non-random. Otherwise, the sequence is random. By these metrics, the 100-bit key passed the Frequency test, Frequency within a block test, Cumulative Sums test, Nonoverlapping template matching test, Serial test, and Approximate entropy tests with p-values > 0.01 (Table 3.1) and can be considered as a random binary sequence.

3.4.2.2 LTspice simulations and analysis of results

In addition to experimental data, binary sequences were also generated using LTspice simulation data. LTspice circuit simulations were performed using a 500 nm by 500 nm network with various molecular, gold nanoparticle and defect ratios. The resistance profiles for some of the simulations performed using LTspice are shown in Figure 3.23 below. In total, 15 sets of simulations were performed with $N_{molecule}$: $N_{particle}$ ratios of 18:0, 16:2, 9:9, 6:12, and 0:18 respectively. Also, each group of simulations (with a particular $N_{molecule}$: $N_{particle}$ ratio) was performed with defect percentages 0, 30 and 50%.

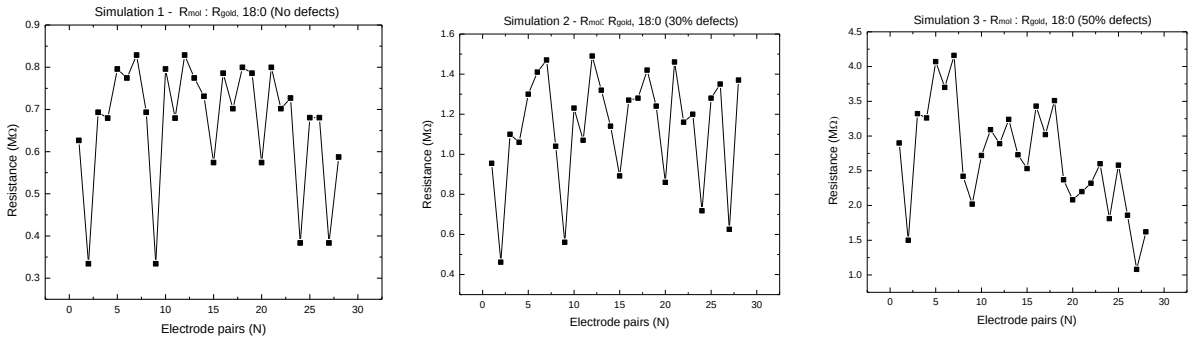

(a) (b) (c)

Figure 3. 23 Low-bias linear circuit simulation results for a 500 by 500 nm network: Resistance profiles built by calculating resistance values at V = 0.5 V between different electrode pairs of molecular networks with (a) molecule: gold nanoparticle ratio, N_{molecule}: N_{particle} of 18:0 (no defects); (b) N_{molecule}: N_{particle} ratio of 18:0 (30% defects); (c) N_{molecule}: N_{particle} ratio of 18:0 (50% defects).

Using the resistance profiles generated from all the simulations, 15 27-bit binary sequences were generated, and subsequently tested using the NIST statistical test suite. The binary sequences and results of the statistical tests are shown in Appendix A.

It can be observed from the results of the NIST tests that the molecular networks with a higher percentage of defects passed a higher number of tests in most cases. For example, the third bit stream, corresponding to Simulation 3 (N_{molecule}: N_{particle}, 18:0 with 50% defects) passed all the seven tests run, while the first bit stream, corresponding to Simulation 1 (N_{molecule}: N_{particle}, 18:0 with no defects) passed only four of the seven tests run. This is also the case for Simulations 4 and 6. The fourth bit stream, corresponding to Simulation 4 (N_{molecule}: N_{particle}, 16:2 with no defects) passed only four out of the seven tests while the sixth bit stream, corresponding to Simulation 6 (N_{molecule}: N_{particle}, 16:2 with 50% defects) passed six out of the seven tests.

Another interesting observation from the NIST tests on generated keys is related to the percentage of molecular contacts in the networks. In most cases, the higher the percentage of molecular contacts in the networks, the more the number of tests passed. For example, the thirteenth bit stream, corresponding to Simulation 13 ($N_{molecule}$: $N_{particle}$, 0:18 with no defects) passed only four out of the seven tests run, while both the tenth bit stream, corresponding to Simulation 10 ($N_{molecule}$: $N_{particle}$, 6:12 with no defects), and the seventh bit stream ($N_{molecule}$: $N_{particle}$, 9:9 with no defects) passed all seven tests run. Exceptions to this were observed for molecular networks with 100% molecular contacts, which passed only four out of the seven tests run. Therefore, irrespective of the overall trends observed, extreme cases (or molecular networks with 100% molecular contacts or 100% gold nanoparticles) did poorly on the NIST tests. This behaviour can likely be explained by the distribution of resistances in the network: the more evenly distributed the proportion of molecules to gold nanoparticles, the more the variations in the resistances between electrode pairs, and the more random the generated keys. Essentially, for networks with both gold nanoparticles and molecules, the resistances will not cluster around similar values because both molecular contacts and gold nanoparticle contacts, with significantly different resistances, exist in the molecular networks.

Observations from the simulations of the molecular networks present a roadmap for future experiments for generating random binary sequences: by harnessing the tunability of the ratio of molecules to gold nanoparticles in the molecular networks, it might be possible to control and improve the randomness of the generated bits.

3.5 Conclusion

Self-assembled gold nanoparticle networks were fabricated, based on a solution-based method, and electrically characterized using the Keithley 4200-SCS system. In most cases, linear current-voltage characteristics were measured on the nanostructured networks at low biases, however, nonlinear asymmetric I-V curves were occasionally observed in some samples. Another interesting occurrence was the observation of nonlinear *I-V*s at high biases in some samples which displayed linear *I-V*s at lower bias.

The conducting properties of molecular networks were investigated through the analysis of their *I-V* data, and the results show the tunability of the electrical properties of the networks by modifying the concentration of gold nanoparticles or molecules.

A simplified linear resistor circuit model of the molecular network's structure provides an approximate way to associate the network conductivity to its dimensions. Consequently, the molecular network can be abstracted into a network of interconnected resistors. The developed linear circuit model provides a good estimation of the network's conductance at low bias and is consistent with the measured data to a certain extent, however, the accuracy of the model might be improved by modelling nonlinearities in the molecular networks and also accounting for the multilayer nature of the molecular films.

Molecular networks hold potential as elements (resistors, diodes [92], transistors, memory devices [92], etc.) in future molecular integrated circuits by harnessing observed NDR, hysteresis and rectification effects, and the self-assembly method is believed to be a promising way for implementing molecular circuitry because of its capability to fabricate nanoscale structures in large numbers cheaply and easily.

At present, we propose a hardware security device based on metal-molecular networks deposited on 8-pad substrates, which utilizes variations in the resistance of the networks between electrode pairs for generating random keys. The generated keys passed randomness tests such as the Hamming inter-distance and NIST tests.

Chapter 4 Modelling the Electronic Characteristics of Metal-Molecular Networks

4.1 Introduction to Quantum Mechanical (QM) Computational Methods

QM-based descriptions of systems partition the atom into the nuclei and surrounding electrons and hence several parameters such as electron density, many-body contributions, and charge transfer, are considered in the description of the system [93]. Most calculations in quantum mechanical systems are based on the time-independent Schrödinger wave equation and the various methods and approximations which have been developed to solve it are discussed in this Section.

4.1.1 Molecular orbital (MO) theory

MO theory is a method for describing the electronic structure of molecules using quantum mechanical approximations. In MO theory, electrons in a molecule are not assigned to individual chemical bonds between atoms but are treated as moving under the influence of the atomic nuclei in the whole molecule [94].

A basic principle of molecular orbital theory is the approximation of the states of bonded electrons or molecular orbitals as linear combinations of atomic orbitals, wherein the

molecular orbital wave function ψ_j can be written as a weighted sum of the N constituent atomic orbitals X_i according to the following equation [94]:

$$\psi_j = \sum_{i=1}^{N} C_{ij} X_i \quad (4.1)$$

Molecular orbitals are often termed as bonding, or antibonding orbitals. A bonding orbital concentrates the electron density in the region between a given pair of atoms, and can further be grouped into sigma, pi, delta, or phi orbitals [95]. Antibonding orbitals concentrate the electron density on the side of each atom which is furthest from the other atom, and so tends to pull the two nuclei away from each other and weaken the bond between them [96]. In such a case, the molecular orbital wave function can have a node with zero electron density between the nuclei, due to the cancellation or destructive interaction of atomic wave functions [96].

Figure 4.1 below shows an image of hydrogen bonding and antibonding molecular orbitals.

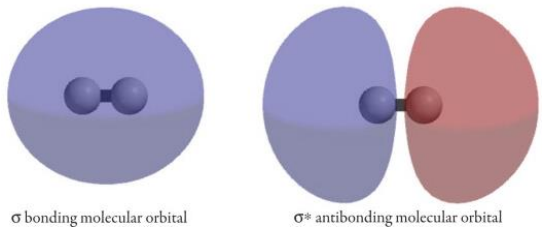

Figure 4. 1 Image of Hydrogen bonding and antibonding molecular orbitals (adapted from Ref. 96).

4.1.2 Ab initio methods (e.g., Hartree-Fock Method)

Quantum mechanical methods can be divided up into ab initio, semi-empirical, and density functional theory (DFT) methods. Ab initio means “from first principles” or “from the beginning”, implying that the only inputs into such calculations are physical constants [97].

Ab initio methods require no empirical information about the molecular system being considered, but rather apply various approximations to solve Schrödinger's equation using wave functions to describe atomic orbitals for the calculation of molecular properties. These methods are useful because they can transform many-atom systems into many-body systems composed of electrons and nuclei, hence simplifying Schrödinger's equation [97].

Ab initio methods are extremely rigorous and can only be applied to molecular systems with a few atoms, hence other quantum mechanical methods that are less computationally intensive may be preferred in cases where an extremely high level of accuracy is not required [98].

Of the ab initio methods available, the Hartree-Fock method is one of the best known and most used approximation procedures to solve the time-independent Schrödinger wave equation for a multi-electron molecular system. Hartree-Fock method assumes that the exact N-body wave function of the system can be approximated by a single Slater determinant (in the case where the particles are fermions) or by a single permanent (in the case of bosons) of N spin-orbitals.

The Hartree-Fock method is also commonly called a self-consistent field (SCF) method because the solution requires the final field as computed from the charge distribution to be self-consistent with the assumed initial field, and the equations are typically solved by means of an iterative procedure.

The Hartree-Fock method makes five simplifications to numerically solve the time-independent Schrödinger equation for many-electron systems [98]:

1. The Born-Oppenheimer approximation is assumed. The coupling between the nuclei and electrons can be ignored and the motion of the electrons and nuclei can be separated.

2. Relativistic effects are completely neglected, and the momentum operator is assumed to be completely non-relativistic.

3. The variational solution is assumed to be a linear combination of a finite number of basis functions, which are usually chosen to be orthogonal, and the finite basis set is assumed to be approximately complete.

4. Each energy eigenfunction is assumed to be describable by a single Slater determinant. The wave function can be built using the Slater determinants as follows:

$$\Psi\lambda 1, \lambda 2, \dots, \lambda \mathrm{N}\ (1,2, \dots, \mathrm{N}) = \frac{1}{\sqrt{N!}} \sum_P (-)^P\ P_{\Psi\lambda 1}(1)_{\Psi\lambda 2}(2) \dots {}_{\Psi\lambda \mathrm{N}}(N) \tag{4.2}$$

$$\Psi\lambda 1, \lambda 2, \dots, \lambda \mathrm{N}\ (1,2, \dots, \mathrm{N}) = \frac{1}{\sqrt{N!}} \begin{vmatrix} \Psi\lambda 1(1)\Psi\lambda 2(1) \dots \Psi\lambda \mathrm{N}(1) \\ \Psi\lambda 1(2)\Psi\lambda 2(2) \dots \Psi\lambda \mathrm{N}(2) \\ \dots \\ \Psi\lambda 1(\mathrm{N})\Psi\lambda 2(\mathrm{N}) \dots \Psi\lambda \mathrm{N}(\mathrm{N}) \end{vmatrix} \tag{4.3}$$

where $(-)^P$ represents the permutation factor equal to +1 or -1 for an even or odd number of interchanges, respectively. The columns in the Slater determinant are the single electron wave functions or molecular orbitals. The total wave function in the Hartree-Fock method is a product of the electron orbitals.

5. The mean-field approximation is implied i.e., the method neglects the Coulombic electron-electron repulsion but considers its average effect (mean field) [98], [99].

In summary, an initial guess for the molecular orbital coefficients is made based on the input information. Following this, the Fock matrix is generated and diagonalized, such that the eigenvectors are the new molecular orbital coefficients. A new density matrix is then formed and compared with the former density matrix, and the Fock matrix generation/diagonalization process is repeated until self-consistency is achieved [98].

The starting point for the Hartree-Fock method is a set of approximate one-electron wave functions known as spin orbitals. For a molecular orbital calculation, the initial approximate one-electron wave functions are typically a linear combination of atomic orbitals. According to quantum mechanics, one can determine the ground state of the Hamiltonian by means of the variational principle for the normalized wavefunction $\Psi\,(1,2,\ldots,\mathrm{N})$:

$$\langle\Psi|\mathrm{H}|\Psi\rangle = \sum_{S1}\sum_{S2}\ldots\sum_{SN}\int \Psi^{*}\,(1,2,..,N)\mathrm{H}\Psi(1,2,..,N)\,dr_1 dr_2 \ldots\, dr_l = \text{minimum} = E_0 \tag{4.4}$$

The variational theorem states that for a time-independent Hamiltonian, any wave function will have an energy expectation value that is greater than the true ground-state energy, E_0. Accordingly, one may try to find an approximate wave function $\Psi(1,2,..,N)$ to minimize the expectation value $\langle\Psi|\mathrm{H}|\Psi\rangle$.

Using a Lagrange multiplier, the variational problem can be solved to give:

$$\sum_{\lambda=1}^{N}\langle\partial\Psi_\lambda|H_0|\Psi_\lambda\rangle + \sum_{\lambda,\mathrm{v}}\langle\partial\Psi_\lambda\Psi_\mathrm{V}|U|\Psi_\lambda\Psi_\mathrm{v}\rangle - \sum_{\lambda,\mathrm{v}}\langle\partial\Psi_\lambda\Psi_\mathrm{V}|U|\Psi_\mathrm{v}\Psi_\lambda\rangle - \sum_\lambda \varepsilon_\lambda\langle(\partial\Psi_\lambda|\Psi_\lambda)\rangle$$

$= 0$, where ε_λ (λ =1,2, .., N) denotes the Lagrange multiplier (4.5)

To satisfy (4.5) for an arbitrary variation $\langle \partial \Psi_\lambda \rangle$, the one-electron wavefunction Ψ_λ should be such that: $H_0 \Psi_\lambda(i) = \varepsilon_\lambda \Psi_\lambda(i)$ (4.6)

Equation (4.6) and the approximation used to derive it (i.e., the use of a single Slater determinant to express the many-electron wavefunction) are called the Hartree-Fock equation, and the Hartree-Fock approximation, respectively [98].

4.1.3 Semi-empirical methods

Semi-empirical quantum mechanical methods use similar calculation techniques to ab initio and DFT methods but neglect the core electrons in their approximations and use some parameters from empirical data [100].

4.1.4 Density Functional Theory (DFT)

Besides the ab initio and semi-empirical methods discussed above, another main category of quantum mechanical computational methods is the density functional theory [97]. DFT methods determine the properties of molecular systems from calculations based on their electron densities, instead of dealing with the wave functions directly. DFT methods are advantageous because they can be used for modelling systems involving hundreds of atoms however, they have a major drawback of not being able to account for electron-correlation effects, which may be important depending on the molecular system being studied [97].

DFT allows for the calculation of the properties of a molecular system based on a description of the positions and species of the individual atoms in the system. The DFT has

its starting point as Schrodinger's equation for an N-electron system in a given external potential $v_{ext}(r)$ [53]:

$$\left[-\frac{\hbar^2}{2m}\sum_{i=1}^{N}\nabla i^2+\sum_{i=1}^{N}v_{ext}(r_i)+\frac{1}{2}\sum_{i\neq j}\frac{e^2}{|r_i-r_j|}\right]\psi(r_i,\dots,r_N)=E\psi(r_i,\dots,r_N) \qquad (4.7)$$

where $\psi(r_i,\dots,r_N)$ is the many-body wave function and E is the total energy of the system [53].

Schrodinger's equation contains all the information about the properties of a molecular system, however solving it directly presents some difficulties because it entails finding a function of 3N variables (where N is the number of electrons in the system) or solving a many-body problem [54]. The DFT, which rests on the Hohenberg and Kohn theorem and the equations derived by Kohn and Sham, provides an immense simplification of this problem by transforming the many-body Schrodinger equation into a one-electron equation [54].

The Hohenberg and Kohn theorem states that the ground state energy from Schrodinger's equation is a unique functional of the electron density and the electron density that minimises the energy of the overall functional is the true ground-state electron density corresponding to the full solution of the Schrodinger equation. By extension, the ground-state electron density *n*(r) uniquely determines all the physical properties, including the energy and wave function, of the ground state, and the Schrodinger equation can be solved by finding a function of three spatial variables, the electron density, rather than a function of 3N variables, the wave function.

According to the Kohn-Sham theory, there exists an unknown energy functional of the charge density, which attains its minimum value only if the charge density is the ground-

state charge density, thus the ground-state charge density and all other desired properties can be obtained by minimising the energy functional [53].

Kohn and Sham decomposed the functional according to [53]:

$$F[n] = T_s[n(r)] + \frac{e^2}{2} \int dx dx' \frac{n(r)n(r)'}{|r-r'|} + E_{xc}[n(r)] \quad (4.8)$$

where $T_s[n(r)]$ is the kinetic energy of the non-interacting electron system, the second term in Eq. 4.8 is the Coulomb electronic repulsion, and $E_{xc}[n(r)]$ is the unknown term, called the exchange-correlation functional. Various approximations for the exchange-correlation functional exist depending on the method used to describe it. In the Local Density Approximation (LDA), the exchange-correlation functional depends only on the local value of the density and is obtained from the parametrization of the exchange-correlation energy of a uniform electron gas as a function of the density. The Generalised Gradient Approximation (GGA) determines the exchange-correlation functional using the both local electron density and the local gradient in the electronic density, to give a more sophisticated approximation.

The solutions of the Kohn-Sham equations are the single-electron wave functions that depend on only three spatial variables [53]. Since the exchange-correlational functional is initially unknown, a guess has to be made for the initial electron density value used to solve the Kohn-Sham equations. The Self-Consistent algorithm used in obtaining the ground-state electronic density is described below.

In this work, we focused on using DFT-based, SIESTA for modelling the electronic properties of dithiol molecule-metal cluster networks [101]. SIESTA is a fully self-consistent calculation which allows for fast simulations by using minimal basis sets based

on a flexible linear combination of atomic orbitals. The important approximations on which SIESTA is based are the Born and Oppenheimer approximations and the use of pseudopotentials. The pseudopotentials are used with atomic basis sets to get rid of the core electrons and allow for the expansion of a smooth (pseudo)charge density on a uniform spatial grid. In summary, the main features of Siesta are [101]:

1. It uses the standard Kohn-Sham self-consistent density functional method in the LDA and GGA approximations.

2. It uses norm-conserving pseudopotentials in their fully nonlocal (Kleinman-Bylander) form.

3. It uses atomic orbitals as a basis set, allowing unlimited multiple-zeta and angular momenta, polarization and off-site orbitals. The radial shape of every orbital is numerical and any shape can be used and provided by the user, with the only condition that it has to be a strictly confined basis orbital, i.e., it has to be strictly zero beyond a user-provided radius.

4. Projects the basis functions and electron density onto a real-space grid to calculate the Hartree and exchange-correlation potentials and their matrix elements.

5. It allows for the use of localized linear combinations of the occupied orbitals, hence making the computer time and memory scale linearly with the number of atoms in the

system. Therefore, simulations with several hundred atoms are feasible with modest workstations.

4.1.5 Density Functional Non-equilibrium Green's Function (DFT-NEGF)

The NEGF method, a modification to the mesoscopic transport theory developed by Landauer, includes the effects of inelastic (electron-phonon) scattering and electron-electron interactions under non-equilibrium conditions (under an applied bias), and gives a more general approach for solving the transport problem [53]. In the NEGF method, the system is partitioned into the central region and left and right electrodes, as shown in Figure 4.2 below.

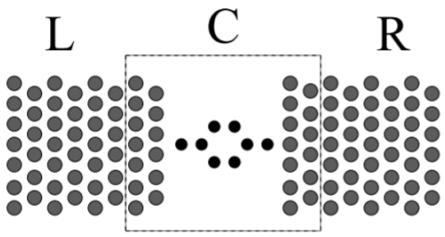

Figure 4. 2 Typical setup of a NEGF calculation: the left and right electrodes (L, R) are assumed to be semi-infinite electron reservoirs in equilibrium at a fixed electrochemical potential. The central region (C, within the dashed box), includes the molecule and a small portion of the electrodes (adapted from Ref. 53).

The electronic structures of the various regions are computed in different ways, depending on the different implementations of the NEGF method used. If a cluster geometry is adopted, then the central region is finite, and the electrodes are considered to be bulk-like or semi-infinite. Otherwise, the electronic structure is computed with a periodic boundary conditions calculation.

The NEGF method of solving for electronic systems' transport basically entails the calculation and integration of the Green's functions with respect to the energy and wave vectors, to obtain the density matrix of the electronic system [53].

The NEGF formalism, combined self-consistently with DFT (DFT-NEGF) is the most ubiquitous method of modelling electronic transport at the nanoscale [54]. The DFT is first used to obtain the Hamiltonian and electronic structure for the scattering region and then the NEGF is used to solve for the charge density, transmission and current of the molecular system.

After solving the ground state problem using DFT, the Green's function of the central region is computed [54]. The Green's function at energy E is given by [55]:

$$G(E) = [(E+i\eta)S - H - \Sigma_L - \Sigma_R]^{-1} \quad (4.9)$$

where H and S are the Hamiltonian and overlap matrix for the scattering region as determined by DFT, η is a positive infinitesimal and $\Sigma_{L,R}$ are self-energies that account for the effect of the left and right electrodes on the scattering region.

Following this, the new charge density and potential are calculated. The charge or electronic density is obtained as:

$$\rho = \frac{1}{2\pi} \int_{-\infty}^{\infty} [f(E, \mu_L)\, G\Gamma_L G^{\dagger} + f(E,\ \mu_R)\, G\, \Gamma_R G^{\dagger})]dE \quad (4.10)$$

where $\mu_{L,R}$ are the electrochemical potentials of the electrodes and $f(E, \mu)$ is the Fermi-Dirac function that describes the population for a given energy. The electronic density obtained from Green's function is used in a subsequent DFT step, and the calculation is repeated until self-consistency between DFT and NEGF is attained.

The transmission function can be obtained from Green's function as:

$$T(E) = Tr\ (\Gamma_L G \Gamma_R G^{\dagger}) \quad (4.11)$$

Finally, the current can be obtained using the Landauer-Büttiker formula as [55]:

$$I = \frac{2e}{h} \int_{\mu_L}^{\mu_R} T(E)dE = \frac{2e}{h} \int_{\mu_L}^{\mu_R} (\mathrm{Tr}\,(\Gamma_L G \Gamma_R G^{\dagger})\,dE \tag{4.12}$$

Figure 4.3 below shows the steps required for an *I-V* calculation using the DFT-NEGF methodology. Initially, the system geometry is defined, and system is separated into scattering and electrode regions. After this, the independent self-consistent calculations for the electrodes are performed, and these calculations provide the effective potential and density of the electrode regions. From the self-consistent Hamiltonian of the electrodes, the self-energies, Σ_L, Σ_R, are calculated. These initial calculations are then used as input to the *I-V* calculation. Starting with an initial guess of the electron density, the Hamiltonian of the scattering region is constructed. Next, Green's function of the scattering region is calculated from the Hamiltonian and the electrode self-energies. Finally, using the Green's function, the electron density can be calculated, and the process is repeated until self-consistency is achieved [102].

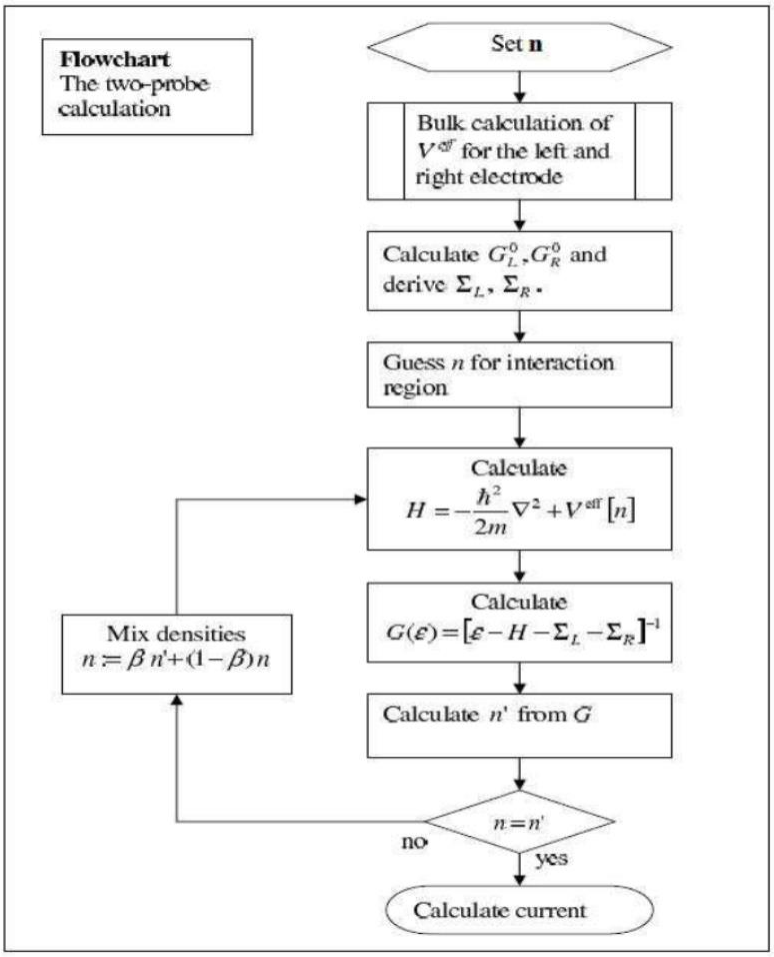

Figure 4. 3 Flowchart showing the steps required to perform an *I-V* calculation with DFT-NEGF (adapted from Ref. 102)

DFT-NEGF-based, TranSIESTA and TBtrans were used in this work for computing the electron transport properties and *I-V* characteristics of the molecular systems studied under an applied bias.

The TranSIESTA method is based on the NEGF technique that has been interfaced with the SIESTA electronic structure package in such a way that the density matrix of the system is calculated self-consistently when the system is subject to an external bias. In the typical TranSIESTA calculation setup, a molecular system is coupled to two electrodes with

different electrochemical potentials. The program uses SIESTA to obtain the Hamiltonian in a localized basis set, and the Hamiltonian, *H* is separated into left electrode, contact region, and right electrode. The electrode Hamiltonians are obtained from separate bulk calculations, whereas the Hamiltonian of the contact region is calculated self-consistently. The *trans* part calculates the non-equilibrium density matrix, *D*, from *H*, using an NEGF technique [103].

The TBtrans code is a tight-binding transport code based on the non-equilibrium Green's function method. It is primarily implemented for the support of TranSiesta (DFT+NEGF) as a backend for calculating electron transport, interpolated *I-V* curves, and transmission eigenvalues etc., for self-consistent DFT software under an applied bias [104].

4.2 Simulated Nanostructures and Modelling Methods

4.2.1 Nanostructures simulated

A myriad of studies have been conducted on modelling the electronic transport properties of molecular systems, with the BDT molecule being the model system used for investigating molecular transport junctions [55], [56], [57], [58], [59], owing to the stability of BDT single-molecule junctions [105], and presence of delocalized π-electrons [106]. Additionally, the presence of a small HOMO-LUMO gap compared to alkanedithiol chains, and possibility of functionalizing the BDT molecule makes it attractive for potential molecular electronic applications [107]. Specifically, the electronic and transport properties of a BDT molecule bridged between two gold electrodes has been extensively

studied by researchers [58], [59], and the consensus is that delocalized molecular orbitals near the Fermi energy are responsible for electron transport through the molecular junction [58].

Inspired by previous work simulating single BDT molecules sandwiched between bulk electrodes, we modelled molecular systems comprising of 1,4-benzenedithiol and 1,3,5-benzenetrithiol molecules interconnected with Au metal clusters. The molecules and metal clusters were connected together to form nanoscale networks with multiple metal-molecule nanojunctions. The metallic nanocluster used here is the planar Au_6 cluster, which is one of the stable isomers of Au [108], [109]. By connecting benzenedithiol or benzenetrithiol molecules and Au_6 clusters together, linear, and branched chains, respectively, comprising of multiple molecular junctions were created as shown in Figure 4.4. Linear chains of different lengths were defined by the number of gold cluster units they contained, as shown in Figure 4.4 (c-e). The Au-S bond length used was approximately 2.3 Å; the S-C bond length was 1.78 Å; the spacing between gold atoms in the left and right electrodes was 2.96 Å; and the bond lengths between gold atoms in the Au_6 cluster ranged from 2.9 Å to 3.05 Å, similar to previous works [110], [111].

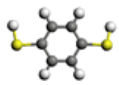

+

(a) Benzenedi(tri)thiol (b) Au metal cluster

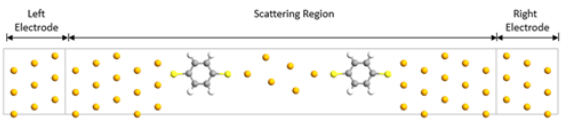

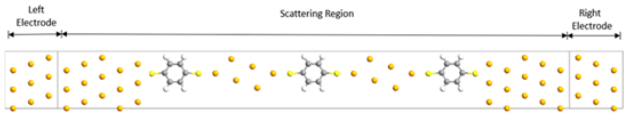

(c) 1-unit chain (d) 2-unit chain

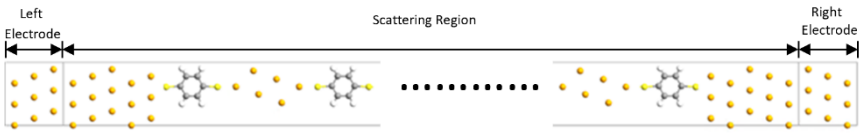

(e) N-unit chain

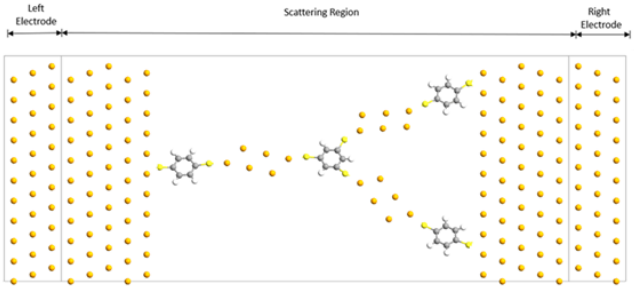

(f) Y-shaped network

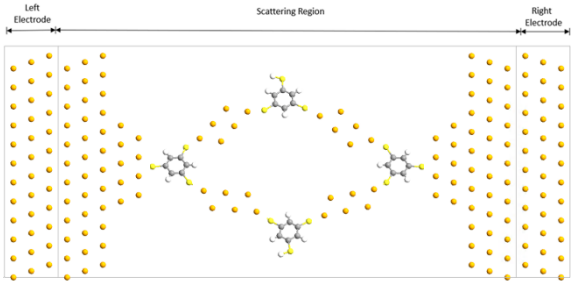

(g) Diamond-shaped network

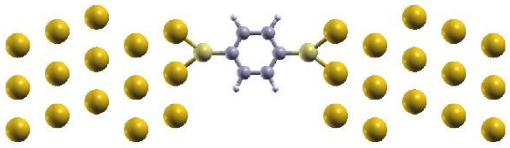

(h) Benzenedithiol molecule

Figure 4. 4 (a-b) GGA PW91-optimized building blocks and starting structures for (c-g) Benzenedithiol-Au_6 linear chains and branched networks of various lengths. Here, golden, yellow, white, and grey colors denote gold, sulfur, hydrogen and carbon atoms, respectively. In addition to the networks, the central scattering region also contains a transition region from the left and right electrodes, whose size was chosen to balance accuracy and computational time; (h) 1, 4-benzenedithiol molecule sandwiched between gold electrodes.

4.2.2 Modelling Methods

As mentioned earlier, the structures modelled comprised interconnected thiolated molecules (1, 4-benzenedithiol and 1, 3, 5-benzenetrithiol), and gold clusters containing 6 atoms (Au_6).

The GGA model, developed by Perdew and Wang (PW91) [112] available within the density functional theory (DFT) package DMol^3 [113], was used to optimize the molecules and the planar parallelogram-shaped Au metal clusters (Figure 4.4 (a, b)), which were subsequently connected using the Virtual Nanolab software to build all the linear chains and branched networks of various lengths.

The electronic and transport properties of metal-molecular networks were studied using various software packages. Molecular networks, comprising linear and branched chains of interconnected thiolated molecules and gold clusters, were built to resemble an electrode/(scattering region)/electrode configuration, as shown in Figure 4.4 (c-h).

SIESTA, a DFT-based software package was used to perform equilibrium electronic structure calculations on the molecular networks and generate information about their electronic DOS and molecular orbitals [114]; while the TranSIESTA module of the SIESTA-4.0 and 4.1 versions, which is based on the DFT-NEGF formalism [115], in conjunction with a tight-binding transport code, TBTrans, was used to compute electronic transport properties, such as the transmission spectra, transmission eigenvalues, and *I*-*V* characteristics of the networks under an applied finite bias.

For visualizing the generated electronic structure information, XCrySDen [116], a molecular structure visualization program, was used to display molecular orbital isosurfaces and electrostatic potentials of the nanoscale networks.

For the transport calculations, the system was divided into three regions, namely; the scattering region, which included linear or branched chains of interconnected thiolated molecules and gold clusters plus five layers of gold atoms on each side to serve as the

electrode extension or screening region; the semi-infinite (bulk-like) left electrode; and the semi-infinite (bulk-like) right electrode, as shown in Figure 4.4 (c-g).

The transport properties of the molecular networks were calculated by setting bias voltages between the electrodes. Troullier-Martin norm-conserving pseudopotentials [117] were used to replace the core electrons. The basis set used for Kohn-Sham orbitals expansions for the scattering region and electrodes, was the polarized double-zeta (DZP). The exchange correlation functional [118] for transport calculations was the generalized gradient approximation parameterized by Perdew, Burke and Erzenhof (PBE) [119]. The mesh density was chosen such that the energy of plane waves was less than 200 Ry. For generating the transmission functions of the linear chains, Y-shaped network, and diamond-shaped network, the number of energy points in the energy range, -3.0 to +3.0 eV, of the computed transmission function was 2000, 500, and 300, respectively.

For generating the *I-Vs.*, the density matrix mixing weight value for the self-consistent field cycle was 0.003 and the density matrix tolerance values ranged between 1.0×10^{-3} and 1.0×10^{-5}. The projected density of states (PDOS) information of the isolated molecular networks comprising of the scattering region without the electrode extensions, and the total DOS information of the molecular networks comprising of the entire scattering region, were generated by performing SIESTA calculations on the scattering region with the range of atoms corresponding to the isolated molecular networks and entire scattering region, respectively, specified in all cases. For generating the PDOS and local density of states (LDOS) information, the density matrix mixing weight value for the self-consistent field cycle was 0.01, and the broadening parameter used for plotting the PDOS was 0.01 eV. For generating molecular orbitals, the LDOS at energies corresponding to peaks in the

projected DOS plots, were visualized as isosurfaces, with isovalue, 0.0002. Electric potential, or voltage drops across the structures at various biases were computed using Transiesta. Grid files containing the electrostatic potential information were converted to cube files using the sisl application. Visualizations of the voltage drops as contour lines and contour planes were done using XCrysDen.

Computations were performed on supercomputer clusters made available through WestGrid (www.westgrid.ca), Compute Canada (www.computecanada.ca), and the SciNet HPC Consortium.

4.3 Results and Analysis

4.3.1 Density of States (DOS) of simulated nanostructures (LDOS, PDOS)

Density of states plots provide information about the number of states at different energy levels that electrons in a system are allowed to occupy. The DOS is a convolution of all the system's orbitals or states, as a function of their energy, where an artificial broadening is applied to each state.

The PDOS plot contains the total system orbitals projected onto the basis orbitals/functions of specific atoms in the molecular system between two energies such that the contributions of different atomic orbitals to the total DOS is captured. In this work, PDOS plots were used in order to compare the electronic structures of the metal-molecular networks coupled to gold electrodes with the isolated networks and gain a deeper understanding of the transport properties of our systems.

The LDOS can be described as the DOS weighted by the amplitude of the corresponding wavefunctions at different points in space and is a function of both energy and position. The total and projected density of states information of various linear and branched networks are shown and analyzed below:

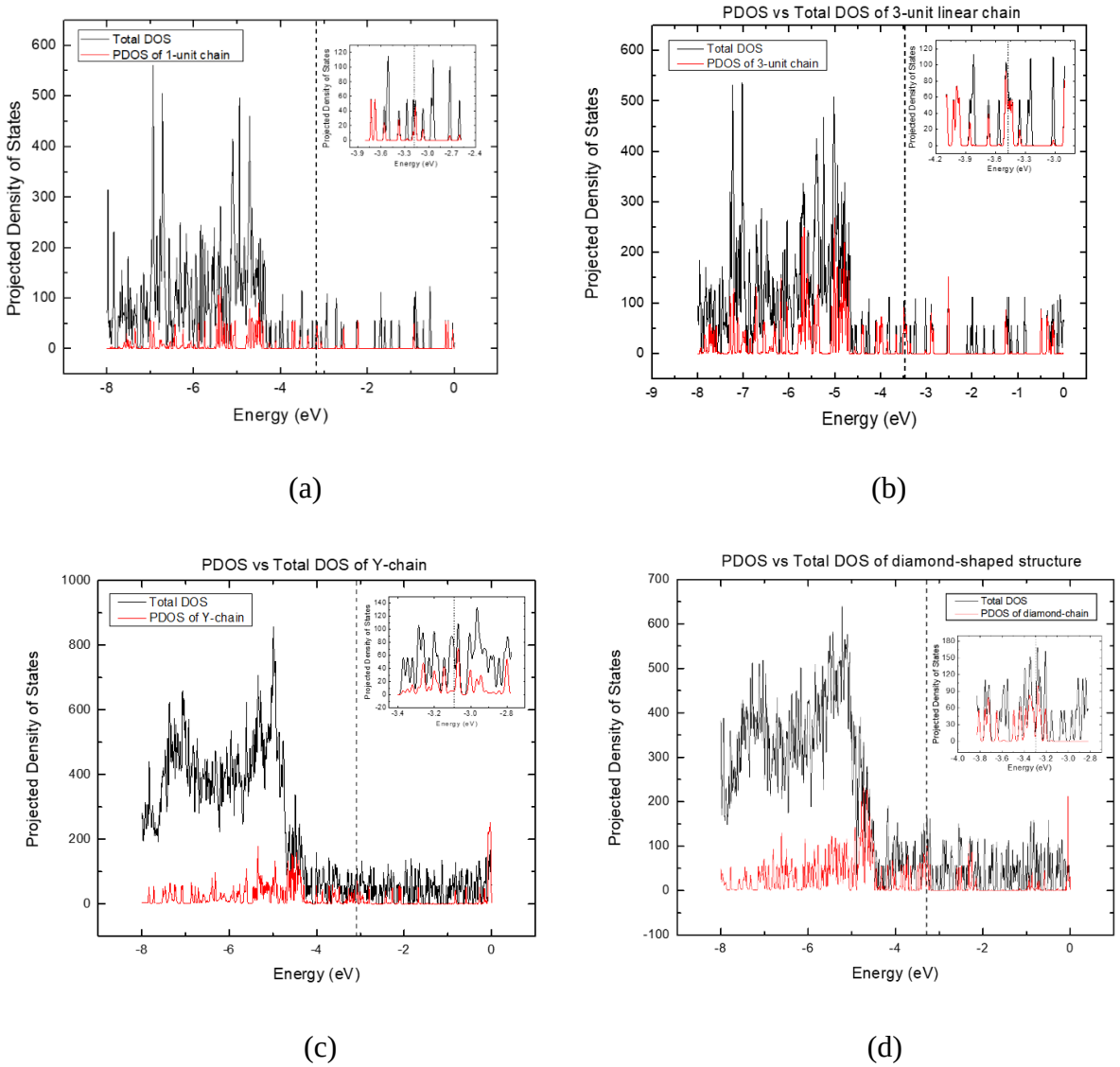

Figure 4. 5 DOS plot for the full system (black) and PDOS plot (red) of (a) 1-unit benzenedithiol-Au_6 linear chain; (b) 3-unit benzenedithiol-Au_6 linear chain; (c) Y-shaped benzenedithiol-Au_6 network; and (d) Diamond-shaped benzenedithiol-Au_6 network; insets – zoom-in of plots near the Fermi energy. Dashed line in the plots represents the Fermi energy.

PDOS plots of the isolated molecular networks without gold atom electrode extensions against the total DOS of the entire scattering region for both linear and branched molecular networks are shown in Figure 4.5 above.

Figure 4.5 (a) shows the total DOS of a 1-unit linear chain coupled to gold electrodes and the PDOS of an isolated 1-unit linear chain. The PDOS peaks just below and above the Fermi energy (represented by the vertical dashed line in the plot) can be seen at ~ -3.1916 eV and -3.1636 eV, and those peaks likely correspond to the HOMO and lowest unoccupied molecular orbital (LUMO) energies, respectively of the 1-unit linear chain. The various peaks in the PDOS plot correspond to molecular orbitals, which likely contribute to the transmission through the linear chain. Similarly, Figure 4.5 (b) shows the DOS plot of a 3-unit linear chain coupled to gold electrodes and the PDOS plot of an isolated 3-unit linear chain. The PDOS peaks just below and above the Fermi energy can be seen at ~ **-3.4959 eV** and **-3.4698** eV, and those peaks correspond to the HOMO and LUMO energies, respectively of the 3-unit linear chain. The various other peaks close to the Fermi energy in the PDOS plot of the 3-unit chain represent the other frontier molecular orbitals (HOMO-1, HOMO-2, LUMO+1, LUMO+2 etc.) of the linear chain.

Figure 4.5 (c) shows the total DOS of a Y-shaped benzenedithiol-Au_6 network coupled to gold electrodes and the PDOS of an isolated Y-shaped network. The PDOS peaks just below and above the Fermi energy (represented by the vertical dashed line in the plot) can be seen at ~ -3.1466 eV and -3.0706 eV, and those peaks likely correspond to the HOMO and LUMO energies, respectively of the Y-branched network. Similarly, Figure 4.5 (d) shows the DOS plot of a diamond-shaped benzenedithiol-Au_6 network coupled to gold

electrodes and the PDOS plot of an isolated diamond-shaped network. The PDOS peaks just below and above the Fermi energy can be seen at ~ **-3.3171 eV** and **-3.2760** eV, and those peaks correspond to the HOMO and LUMO energies, respectively of the diamond-shaped network.

4.3.2 Molecular orbital visualizations of the nanostructures

DFT-based studies of electron transport through molecules have shown that the conductance depends on the energetic alignment of the so-called frontier molecular orbitals (highest occupied molecular orbital (HOMO) and lowest unoccupied molecular orbital (LUMO)), with the Fermi level of the metal electrodes, typically mediated by tunneling transport [57], [120], [121]. The molecular orbitals are therefore an important factor to consider in understanding electron transport through molecular systems. In this work, molecular orbitals were obtained by visualizing the LDOS as isosurfaces at energies corresponding to peaks in the PDOS plots.

Table 4.1 shows the molecular orbitals calculated for 1- and 3-unit benzenedithiol-Au_6 linear chains.

Table 4. 1: Frontier molecular orbitals of 1- and 3-unit benzenedithiol-Au_6 linear chains.

1-unit benzenedithiol-Au_6 linear chain	**3-unit benzenedithiol-Au_6 linear chain**

 LUMO+3, Energy: -2.6029 eV	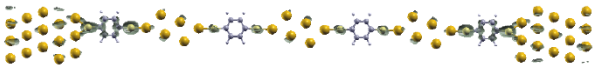 LUMO+3, Energy: -3.3566 eV
 LUMO+2, Energy: -2.7260 eV	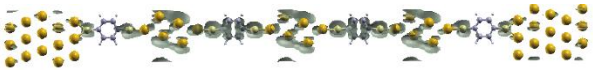 LUMO+2, Energy: -3.4318 eV
 LUMO+1, Energy: -3.0681 eV	 LUMO+1, Energy: -3.4514 eV
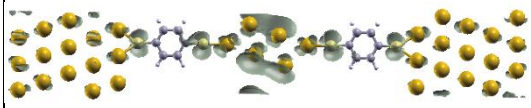 LUMO, Energy: -3.1636 eV	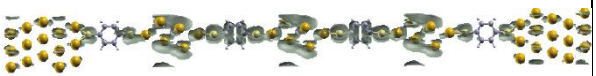 LUMO, Energy: -3.4698 eV
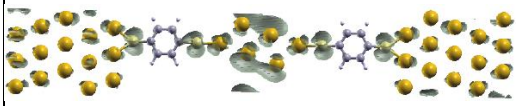 HOMO, Energy: -3.1916 eV	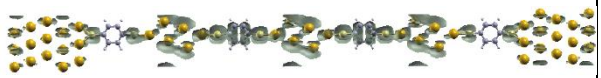 HOMO, Energy: -3.4959 eV
 HOMO-1, Energy: -3.3747 eV	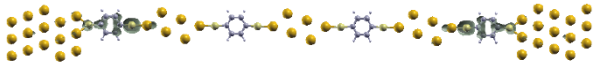 HOMO-1, Energy: -3.6688 eV
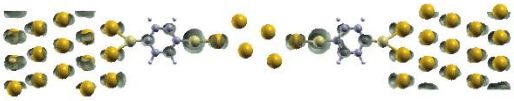 HOMO-2, Energy: -3.5613 eV	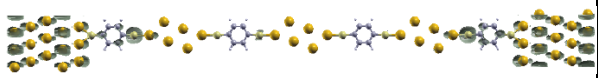 HOMO-2, Energy: -3.8579 eV
 HOMO-3, Energy: -3.6792 eV	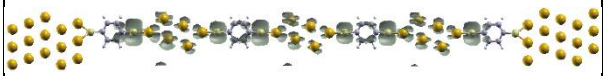 HOMO-3, Energy: -3.9649 eV

The spatial distributions of the molecular orbitals show a significant overlap in some energetically close orbitals, which can combine to form delocalized electron transport channels, whereas in other cases, the charge density is localized around certain atoms, thereby reducing electron transport across the linear chain. For example, HOMO, HOMO-1, HOMO-2, and HOMO-3 orbitals, in the 3-unit benzenedithiol-Au_6 linear chain will overlap to form an electron transport channel but the LUMO orbitals are more clustered around certain atoms and do not extend across the entire linear chain. Therefore, it is expected that the molecular networks will be highly conducting at certain energies and less conducting at others.

Moving on to molecular orbital visualizations for branched networks, Table 4.2 below shows the molecular orbitals of the larger branched benzenedithiol-Au_6 networks. The spatial distributions of the molecular orbitals show some overlap in a few energetically close orbitals, which can combine to form delocalized electron transport channels. For example, if the HOMO, HOMO-1, and HOMO-2 orbitals of the Y- and diamond-shaped benzenedithiol-Au_6 networks, are superimposed on each other, they will form a linked chain of molecular orbitals which extends across the entire branched network structure. In some cases, the position of the localized molecular orbitals in the branched networks shifts from one arm of the structure to another at different energies. For example, LUMO, and LUMO+1, in the Y-shaped benzenedithiol-Au_6 network. This could potentially be useful in switching applications to control current along certain branches of the networks.

Table 4. 2 : **Frontier molecular orbitals of Y- and diamond-shaped benzenedithiol-Au_6 networks.**

Y-shaped benzenedithiol-Au_6 network		**Diamond-shaped benzenedithiol-Au_6 network**	
HOMO	**LUMO**	**HOMO**	**LUMO**
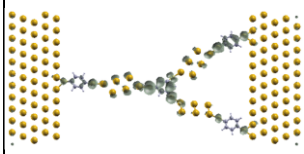 HOMO, Energy: -3.1466 eV	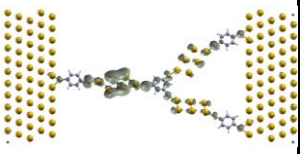 LUMO, Energy: -3.0706 eV	HOMO, Energy: -3.3171 eV 	LUMO, Energy: -3.2760 eV 
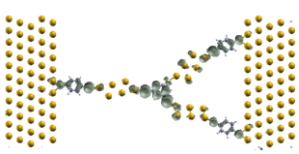 HOMO-1, Energy: -3.2012 eV	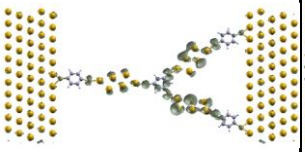 LUMO+1, Energy: -3.0027 eV	 HOMO-1, Energy: -3.3488 eV	 LUMO+1, Energy: -3.2550 eV
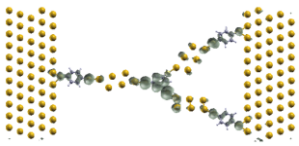 HOMO-2, Energy: -3.2306 eV	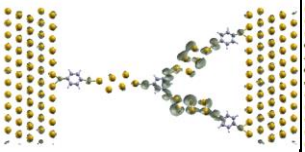 LUMO+2, Energy: -2.9669 eV	 HOMO-2, Energy: -3.3869 eV	 LUMO+2, Energy: -3.2086 eV
HOMO-3, Energy: -3.2615 eV 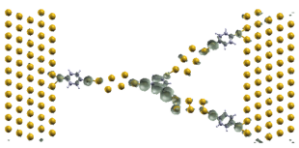	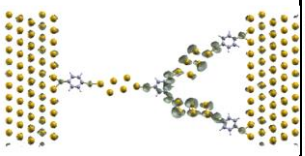 LUMO+3, Energy: -2.9440 eV	HOMO-3, Energy: -3.4363 eV 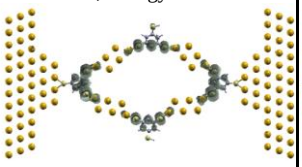	LUMO+3, Energy: -2.5909 eV 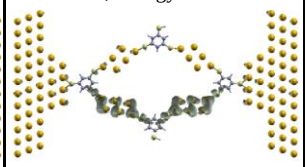

4.3.3 Transmission properties of nanostructures

The transmission spectra of molecular systems can provide information about the metal-molecular coupling, contact geometry, orbital delocalization and the energy difference between the frontier orbitals, etc. [56], [122], [123]. The transmission spectrum shows

various peaks for transmissive orbitals, and the height and width of the peaks reflect the transmissivity of that orbital.

Figure 4.6 (a) and (b) show the transmission spectra of 1- and 3-unit benzenedithiol-Au_6 linear chains. The transmission peaks below the fermi energy level likely correspond to delocalized molecular orbitals (e.g. HOMO, HOMO-1 etc.), which overlap with each other and extend across the entire linear chain, thereby providing effective conduction pathways; conversely, the presence of fewer transmission peaks above the fermi energy level can be attributed to the presence of localized molecular orbitals at higher energies (LUMO, LUMO+1 etc.) [124].

The broad peaks observed in the transmission spectra of both branched networks are likely due to a larger number of available overlapping molecular orbitals which together form conduction pathways for electron transport. For both linear and branched chains, their transmission spectra showed an increase in the width of transmission peaks near the Fermi energy, as the structures were extended, indicating enhanced transmission. This demonstrates the tunability of transmission through molecular networks by modifying their lengths and geometries.

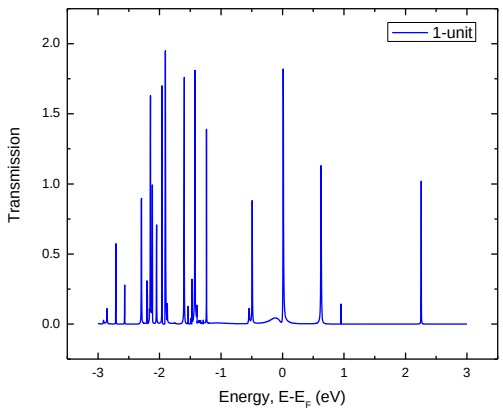

(a)

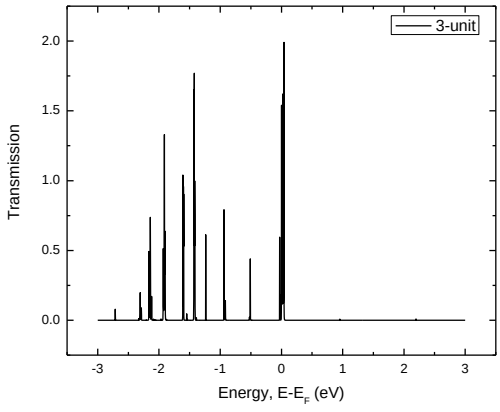

(b)

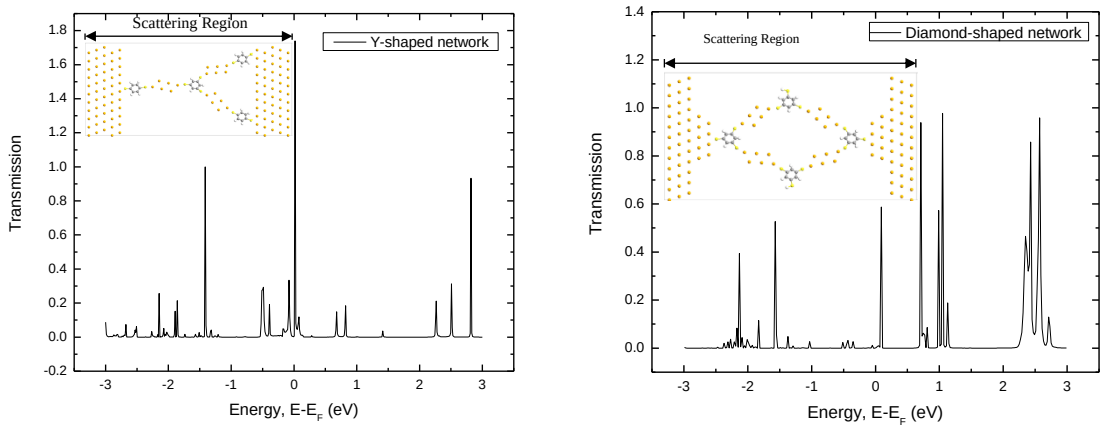

(c) (d)

Figure 4. 6 Electron transmission with respect to energy for various benzenedithiol-Au_6 networks (a) 1-unit benzenedithiol-Au_6 linear chain; (b) 3-unit benzenedithiol-Au_6 linear chain; (c) Y-shaped benzenedithiol-Au_6 network; and (d) Diamond-shaped benzenedithiol-Au_6 network.

4.3.4 *I-V* characteristics and voltage drops of simulated nanostructures

The *I-V* characteristics of molecular systems provide information about the metal-molecular coupling, contact geometry, and orbital delocalization, etc., [56], [122], [123], hence they are invaluable for studying the transport properties of molecular systems.

The calculated current-voltage (*I-V*) characteristics of a BDT molecule and benzenedithiol-Au_6 linear chains are plotted in Figure 4.7 (a-e). Nonlinear *I-V* characteristics with NDR are observed in the linear chains as bias magnitude is increased. NDR effects are seen to become more pronounced with increasing length of the linear chains, as seen from the *I-V* plots. This behavior can be correlated to the number of accessible orbitals at higher energies as the chains are extended, consistent with the transmission spectra of Figure 4.6 (a, b), and

similar to previous work on different length molecular structures [125], [126]. Resonant tunneling mechanisms [127], bias induced alignment of the molecular orbitals [128] and weak molecule-electrode coupling [129] have also been identified as possible sources of NDR in molecular systems connected to metallic electrodes, with the unique hybrid metal-molecular networks containing gold clusters studied here possibly amplifying these effects. As a comparison, the *I-V* characteristics of a metal-molecule-metal junction comprising of a BDT molecule sandwiched between symmetric bulk gold electrodes is shown in Figure 4.7 (a). The measured current was found to be in the μA range with less pronounced nonlinearity/NDR peaks, comparable to previous work [57], [115].

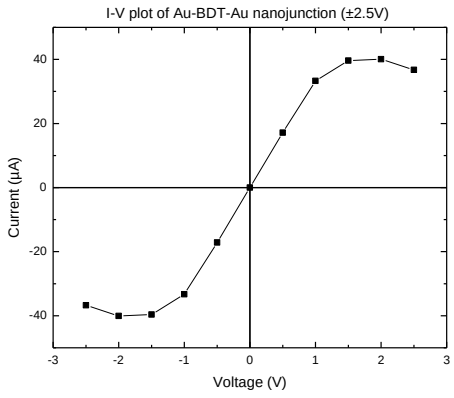

(a)

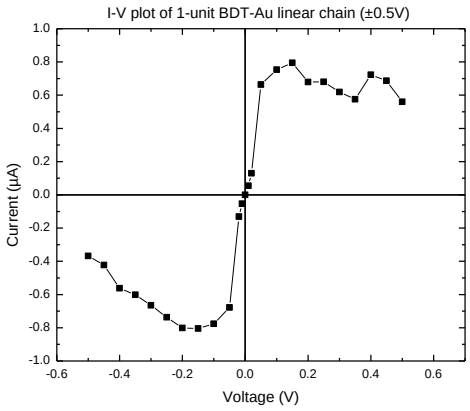

(b)

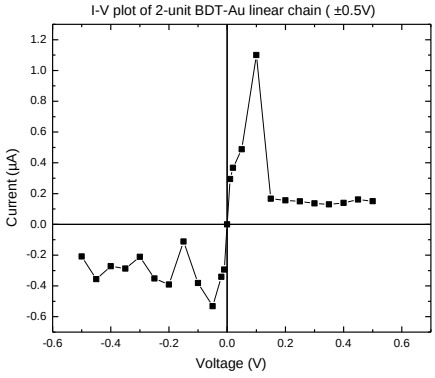

(c)

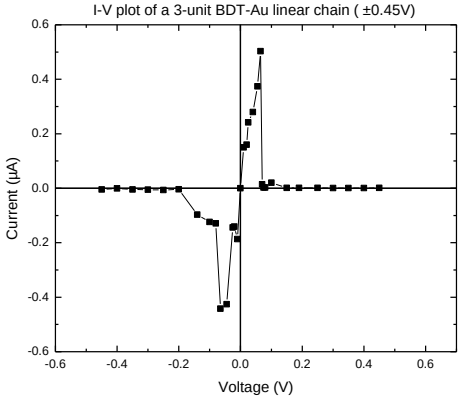

(d)

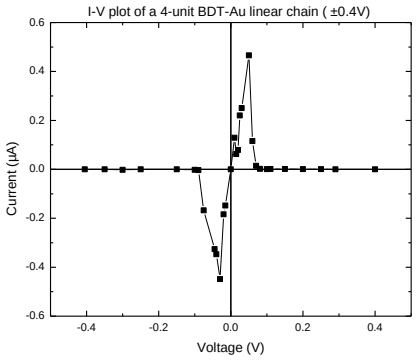

(e)

Figure 4. 7 *I-V* characteristics of various molecular systems studied (a) 1, 4-benzenedithiol molecule; (b) 1-unit benzenedithiol-Au_6 linear chain; (c) 2-unit benzenedithiol-Au_6 linear chain; (d) 3-unit benzenedithiol-Au_6 linear chain; and (e) 4-unit benzenedithiol-Au_6 linear chain.

The calculated *I-V* characteristics of Y- and diamond-shaped benzenedithiol-Au_6 networks are shown in Figures 4.8 (a) and (b), respectively. The Y-structure exhibits an asymmetric, nonlinear *I-V* characteristic with rectifying behavior and NDR over the operating voltage range (Figure 4.8 (a)). The Y-shaped network's *I-V* curve contains a distinct NDR peak near +0.05 V with a peak-to-valley ratio (PVR) of 2.3 and a significant rectification ratio that reaches 10.6 (0.25 V). On the other hand, the diamond-shaped structure exhibits non-ohmic *I-V* behavior (Figure 4.8 (b)) with sharp NDR features near +0.1 V and – 0.05 V and large PVCRs on the order of 200.

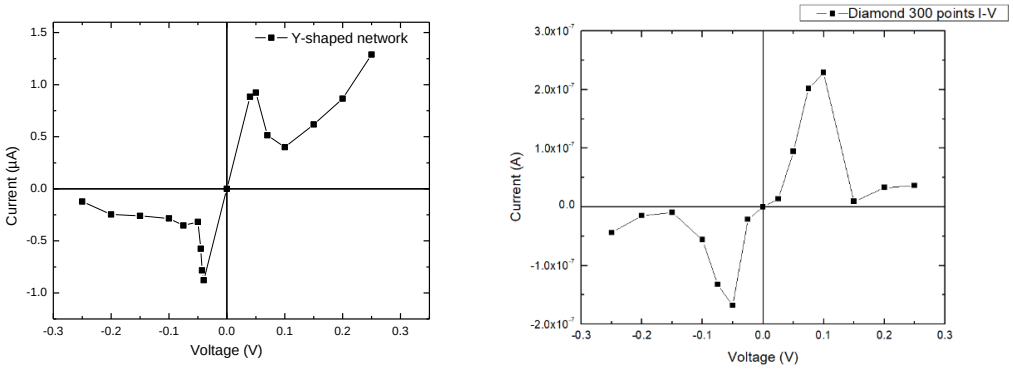

(a) (b)

Figure 4. 8 *I-V* characteristics of various branched benzenedithiol-Au_6 molecular networks (a) Y-shaped network; and (b) Diamond-shaped network.

To gain further insight into the charge transport characteristics, in Figure 4.9, we compare calculated voltage drops for a 1-unit linear chain and Y-shaped network: As expected for the symmetric linear chain in Fig. 4.9 (a), the voltage drop is essentially a mirror image upon switching polarity for a given magnitude of applied bias. In contrast, the Y-structure in Fig. 4.9 (b) shows a distinct difference in the potential drop depending on the sign of applied bias with an electrostatic barrier or pinning apparent near the intersection of the three branches. This asymmetry likely leads to the observed rectifying *I-V* characteristic of Fig. 4.8 (a), which, along with its simultaneous NDR, is reminiscent of an Esaki diode, or perhaps the metal-molecular analog of an interband resonant tunneling diode [130].

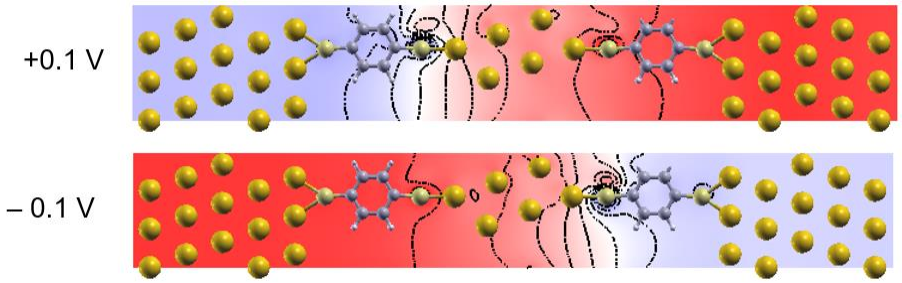

(a)

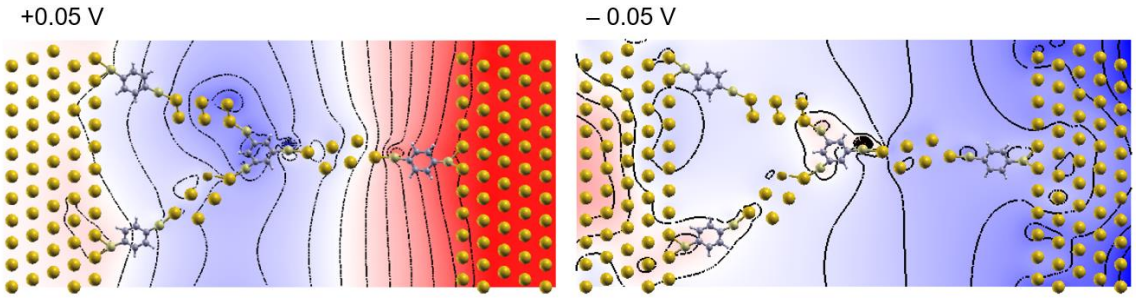

(b)

Figure 4. 9 Potential drop in scattering region between electrodes for (a) 1-unit benzenedithiol-Au_6 linear chain; and (b) Y-shaped benzenedithiol-Au_6 network. Applied biases indicated.

4.3.5 Differential conductance of simulated nanostructures

The differential conductance versus bias voltage plots of different molecular networks are shown in Figure 4.10 below. The plots exhibit significant fluctuations between some bias points as expected from the NDR behavior in the *I-V* characteristics.

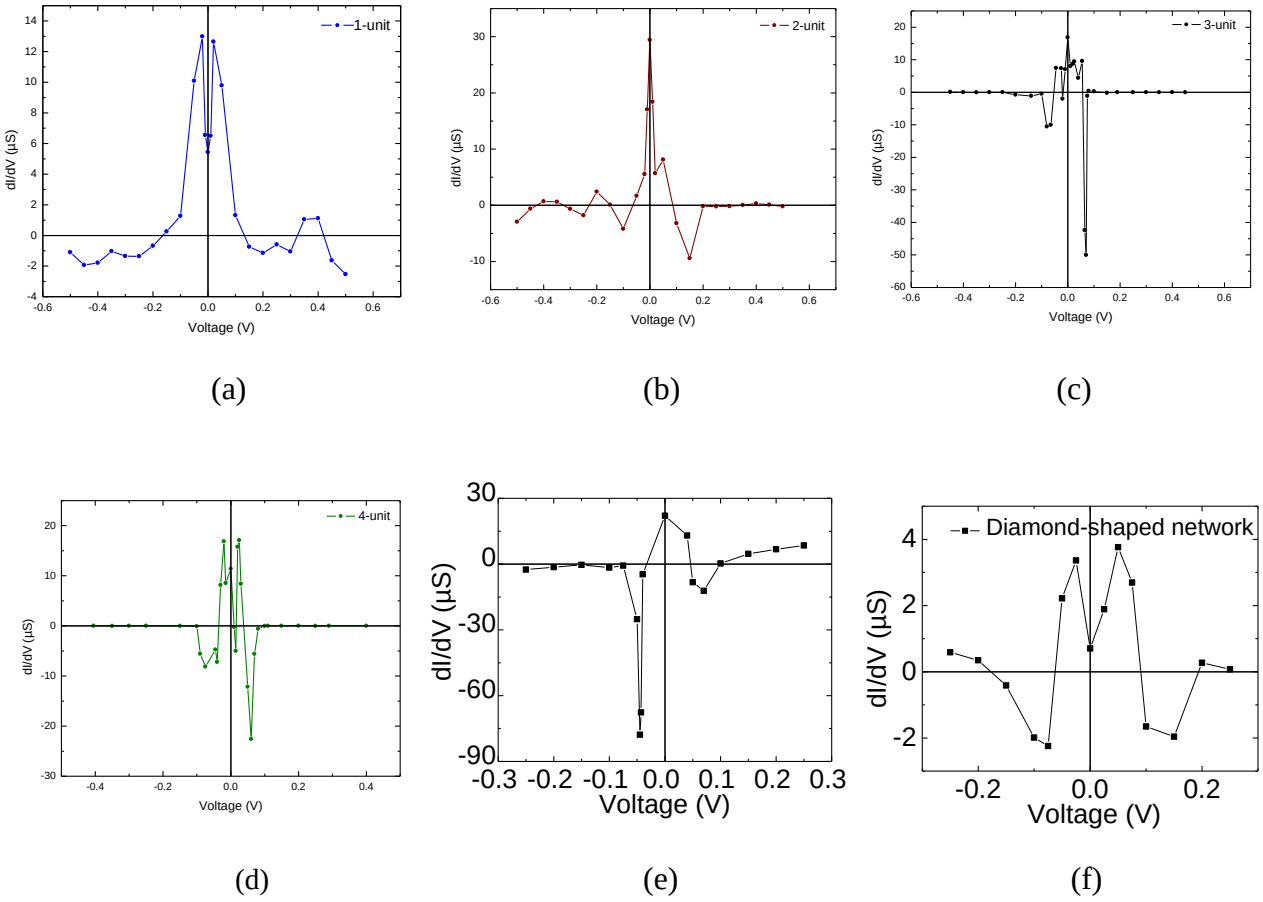

Figure 4. 10 Differential conductance vs. bias voltage plots of benzenedithiol-Au_6 molecular networks (a) 1-unit linear chain; (b) 2-unit linear chain; (c) 3-unit linear chain; (d) 4-unit linear chain; (e) Y-shaped branched network; and (f) Diamond-shaped branched network.

4.3.6 Peak-to-valley-ratios of simulated nanostructures

The peak-to-valley-ratio is the ratio between the peak current and valley current in a device. For applicability of the NDR effect in molecular devices such as analog-to-digital converters and oscillators, high PVR values, particularly in the low bias regime are desired. The molecular networks studied in this work meet these requirements, and thus could potentially be useful in future molecular devices.

For the linear chains, the NDR peaks became more pronounced as the chains were extended, hence, the PVRs increased exponentially with increasing length of the linear chains. Figure 4.11 shows a plot of the PVR against chain length of linear chains. As discussed in detail earlier, weak molecule-electrode coupling, bias induced (mis)alignment of molecular orbitals, and the addition of more unique hybrid metal-molecular junctions likely amplify the NDR behaviour as the linear chains are being extended.

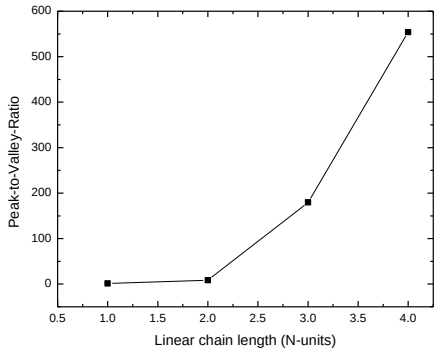

Figure 4. 11 Peak-to-valley current ratio vs. chain length of benzenedithiol-Au_6 linear chains. For the 1-, 2-, 3-, and 4-unit linear chains the ratios were calculated to be 1.38, 8.46, 179.64, and 554.10, respectively.

4.3.7 Comparison of simulated and experimental results

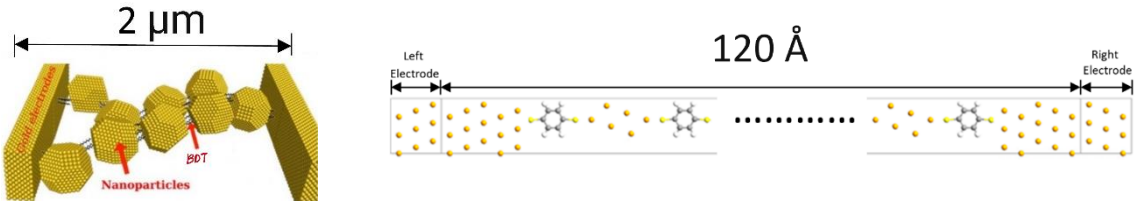

(a) (b)

Figure 4. 12 Schematic of Au-BDT junctions showing typical length scales of experimental and simulated measurements (a) average length of BDT-Au SAM deposited

between adjacent pairs of interdigitated electrode fingers is about 2 μm; (b) length of scattering region of 5-unit BDT-Au linear chain is about 120 Å (adapted from Ref. 50).

It is worth noting that *I-V* characteristics (e.g., NDR and rectification) similar to those obtained from TransSIESTA calculations on the metal-molecular networks, have been observed experimentally. The nonlinear *I-V*s are obtained at different operating voltages: ±0.3 V and ±5 V or 25V/μm and 2.5V/μm (using length scales in Figure 4.12) for the simulated and experimental measurements, respectively, hence, they can not be compared quantitatively. This, along with the underestimation of the band gap of the junction by DFT [131], are likely responsible for the variations in the measured currents (μA for simulations compared to the nA range for molecular devices in this study). Additionally, it is difficult to precisely evaluate the voltage drop variation in the self-assembled networks due to the large number of molecule/particle connections and variations in the network morphologies. However, similar effects associated with the metal-molecule coupling are accounted for in both modelling and experiments, and hence, the results can be compared qualitatively.

The simulated results confirm the experimental data, and vice versa, as regards to NDR and rectification. For example, an increase in the simulated NDR behaviour as the linear chains were extended (as more molecules were added) is analogous to the trend of increasing NDR effects in self-assembled metal-molecular networks with a higher concentration of molecules. This can be attributed to variations in the metal-molecule coupling at different molecular concentrations in the molecular networks: less coupling leads to areas with very low conductance. While the experiments account for this effect in terms of variations in the orientations of the BDT molecule (between lying down and upright orientations) at different molecular concentrations, the simulations account for it

in terms of variations in the interfacial bonding between the molecules and gold clusters as the linear chains are extended.

Similarly, rectification was measured both experimentally and theoretically in the metal-molecular networks. This could be attributed to resonant tunneling between molecular orbitals and the metal delocalized states, thereby leading to a conduction peak, at certain biases, and subsequent detuning of the gold-molecule interfacial states, leading to a decrease in the tunneling current, at biases of opposite polarities [132].

4.4 Emerging Circuit Applications

The metal-molecular networks studied in this work provide several possibilities for applications in nanoelectronics as molecular scale switches and logic circuits. Similar to the electron wave Y-branch switch, the Y-shaped benzenedithiol-Au_6 network has potential as a switching element.

The electron wave Y-branch switch uses a bias applied between the stem and either of the branches of the Y to cause the ballistic transport of electrons through various branches of the device [133].

As illustrated in Figure 4.13, an electric field can be used to deflect charge carriers between various arms of the Y-branch structure. In essence, since the position of the localized molecular orbitals in the branched networks shifts from one arm of the structure to another at different energies, this behaviour could potentially be useful in switching applications where we could control current flow along certain branches of the networks.

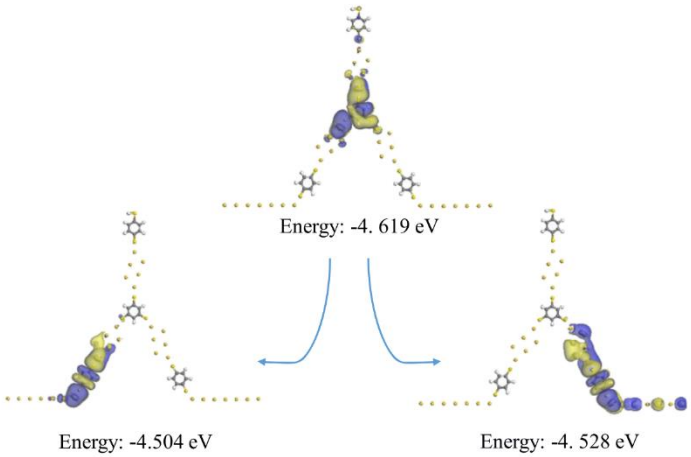

Figure 4. 13 Switching element based on Y-shaped benzenedithiol-Au_6 molecular network (adapted from Ref. 126).

4.5 Conclusion

DFT-NEGF studies were performed on several nanoscale hybrid molecular structures built from geometry optimized benzenedithiol molecules and Au_6 clusters including linear and branched molecular networks.

The linear and branched chains studied displayed nonlinear *I-V* characteristics in all cases with NDR effects which became more pronounced as the structures were extended. Additionally, the orbital spatial distributions were either localized around a few atoms or delocalized. In the case of the latter, energetically close molecular orbitals had significant overlap and they combined to form electron transport paths.

The transmission spectra of the linear chains and branched networks showed an increase in the width of transmission peaks near the Fermi energy, as the structures were extended, indicating enhanced transmission. Peak-to-valley current NDR ratios as large as ~ 500 and

rectification ratios of ~ 10 (0.25 V) were shown for linear and branched circuit elements, respectively, illustrating how charge transport through molecular-scale devices could be controlled with precision by modifying the structure and geometry of molecule-nanoparticle networks.

These results provide a blueprint for exploring applications of metallic nanoparticle-molecular networks in various nanoelectronic devices and circuits, including memory, logic, switching and sensing. We also demonstrated the potential use of a Y-shaped benzenedithiol-Au_6 cluster network as an electron-wave Y-branch switch.

Chapter 5 Conclusion and Future Work

5.1 Conclusion

5.1.1 Self-assembled metal-molecular networks with tunable metal NP: molecule ratios

Metal-molecular networks with tunable metal NP: molecule ratios and an intermediate number of molecules were fabricated using thiolate molecules and colloidal gold nanoparticles via the solution-based self-assembly method, which allows for the tailorability of the networks' topographies by varying the concentration of dithiol molecules used in the solution. The synthesis method employed in fabricating our molecular networks resulted in networked aggregates of gold nanoparticles interconnected by a few dithiol molecules, as confirmed by AFM images of the samples. The molecular networks synthesized could potentially serve as components in future molecular circuits.

AFM and optical microscopy also showed variations in the networks' topographies on varying the ratio of molecules to gold nanoparticles. Thus, the solution-based self-assembly approach is believed to be a promising route for implementing molecular circuits because of the ease of fabricating nanostructures with tunable properties using this method.

In most cases, linear current-voltage characteristics were measured on the nanostructured networks at low biases, however, nonlinear asymmetric I-V curves were occasionally observed in some samples. Another interesting occurrence was the observation of nonlinear *I-V*s at high biases in some samples which displayed linear *I-V*s at lower bias. The tunability

of the electrical properties of the molecular networks by modifying the ratios of molecules to gold nanoparticles was also demonstrated.

Conducting tip AFM measured two distinct resistance ranges of kΩ or MΩ indicating two types of connections between neighbouring gold particles. Additionally, AFM images of the networks showed defects regions or gaps at certain locations. A simplified linear resistor circuit model of the molecular network's structure was developed in LTspice to provide an approximate way to associate the network conductivity to its dimensions. The developed linear circuit model provides a good estimation of the network's conductance at low bias and is consistent with the measured data to a certain extent, however, the accuracy of the model could be further improved.

Self-assembled molecular networks hold potential as elements in future molecular integrated circuits by harnessing observed NDR, hysteresis and rectification effects. At present, we propose a hardware security device based on metal-molecular networks deposited on 8-pad substrates, which has demonstrated some robustness to common security threats.

5.1.2 Modelling metal-molecular networks

Density functional theory non-equilibrium Green's function studies were performed on several nanoscale metal-molecular structures built from geometry optimized benzenedithiol molecules and Au_6 clusters including linear and branched molecular networks. After optimizing the building blocks and building the molecular systems using DMol^3, and Virtual Nanolab, respectively, electronic and transport properties of the

molecular networks were studied using DFT-based software like Siesta, Transiesta and Tbtrans, as well as visualization tools like XCrySDen.

The linear and branched chains studied displayed nonlinear *I-V* characteristics in all cases with NDR effects which became more pronounced as the structures were extended. Additionally, the orbital spatial distributions were either localized around a few atoms or delocalized. In the case of the latter, energetically close molecular orbitals could overlap and combine to form electron transport paths. Peaks in the projected density of states plots correspond to the various molecular orbitals of the networks.

The transmission spectra of the linear chains and branched networks showed an increase in the width of transmission peaks near the Fermi energy, as the structures were extended, indicating enhanced transmission. Peak-to-valley current NDR ratios as large as ~ 500 and rectification ratios of ~ 10 (0.25 V) were shown for linear and branched circuit elements, respectively, illustrating how charge transport through molecular-scale devices could be controlled with precision by modifying the structure and geometry of molecule-nanoparticle networks.

Observed nonlinearities (e.g., NDR and rectification) in the *I-V*s of the metal-molecular structures studied highlight their potential for application as circuit elements in nanoelectronic devices and circuits, including memory, logic, switching and sensing.

5.2 Future work

5.2.1 Electronic transport

The fabrication of self-assembled metal-molecular networks with tunable molecule: AuNP ratios conducted in this study, can be extended by fabricating metal-molecular networks with other sizes of gold nanoparticles. For example, gold-benzenedithiol molecular networks can be fabricated using 5 nm, 10 nm, 50 nm gold nanoparticles, and the electrical and optical results can be compared with existing data for gold-benzenedithiol molecular networks fabricated with 30 nm AuNPs. A likely variation in the topography and conductivity of the metal-molecular networks will be observed, and the variations might provide a template for understanding how the size of the gold nanoparticles affects the morphology of the synthesized nanoscale networks. This might also provide some insight as to how the size gradient between metal nanoparticles and molecules in the networks affect the interconnectivity of the molecular networks.

Metal-molecular networks fabricated using 10 nm colloidal gold nanoparticles and nonanedithiol were electrically characterized in this work, and the preliminary results showed both linear and nonlinear *I-V* characteristics with the current values typically decreasing with increasing proportion of molecular contacts (increasing molecule: AuNP) in the network. The measured currents at low bias for gold-nonanedithiol samples typically fell in the pA – nA range.

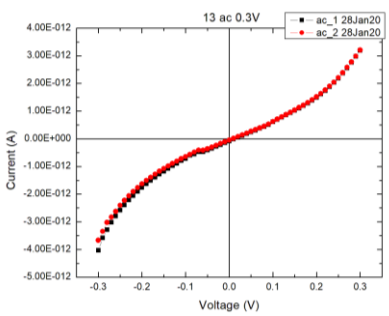

(a)

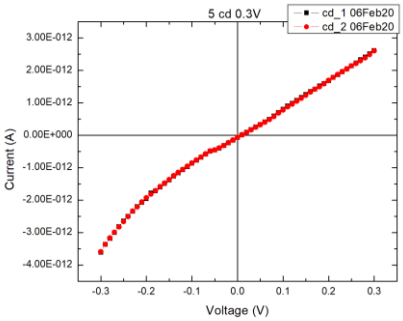

(b)

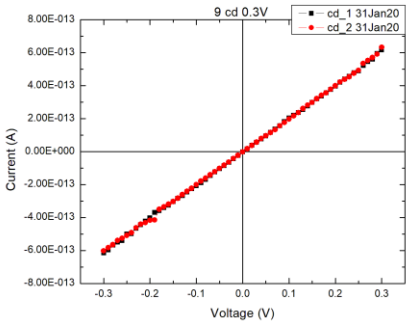

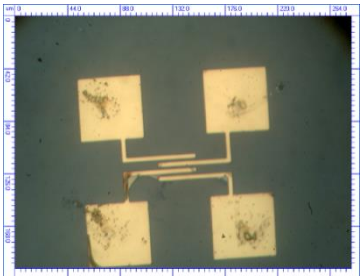

(c) (d)

Figure 5. 1 *I-V* plots of gold-nonanedithiol molecular networks with various molecule: AuNP ratios (a) 1:1; (b) 5:1; (c) 50:1; (d) Optical image of gold-nonanedithiol molecular network with molecule: AuNP = 50:1.

For control samples made using 10 nm gold nanoparticles only, the measured currents at low bias typically fell in the pA range, and both linear and nonlinear *I-V*s were observed. Figure 5.2 below shows the *I-V* plot and corresponding optical image of a control sample made using 10 nm gold nanoparticles.

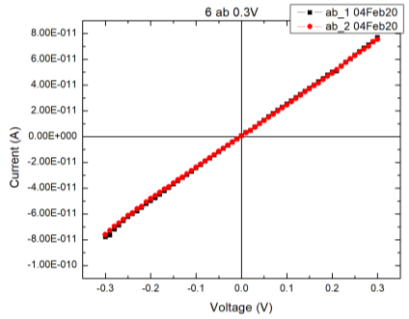

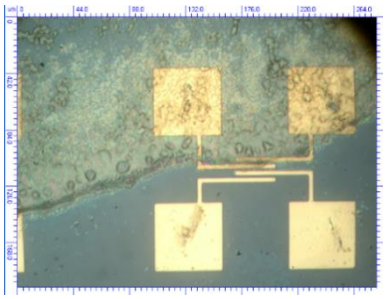

(a) (b)

Figure 5. 2 (a) *I-V* plot of a control sample; (b) Optical image of a control sample.

The structural characterization of the gold-nonanedithiol metal-molecular networks with smaller sizes of colloidal gold nanoparticles (10 nm) could be beneficial for understanding their electrical properties.

To complement this, the use of other molecules apart from dithiols such as graphene, and thiols for fabricating metal-molecular networks could be an interesting study. This could be extended even further by fabricating hybrid networks with graphene, CNTs [72], thiolate molecules and gold nanoparticles. Thiol-linked gold nanoparticle networks will likely form at certain sites of the graphene and introduce interesting electrical properties that could potentially be tuned by modifying the concentration of gold nanoparticles.

Mixed metal-molecular networks or networks formed using mixtures of different thiolate molecules and gold nanoparticles could make for an interesting study. For example, metal-molecular networks could be made using gold nanoparticles, nonanedithiol and hexanedithiol molecules. In this case, the networks would likely have hybrid properties like varying conductances at different sites due to the variation in the interaction between gold nanoparticles and the constituent molecules.

The behaviour of metal-molecular networks at cryogenic temperatures is also worth investigating. Although the conduction mechanism in alkane(di)thiol molecules and SAMs coupled to gold electrodes is believed to be via temperature independent conduction mechanisms like non-resonant tunneling [60], it would be interesting to see how electron

transport in the molecular networks varies at low temperatures compared to standard room temperature measurements conducted in this study.

5.2.2 Modelling

As shown in Chapter 3, the metal-molecular networks studied in this work sometimes displayed nonlinear *I*-*V* characteristics, hence the linear resistor circuit model used to simulate the networks might not provide a complete description of the networks, particularly at higher bias. The LTSpice resistor circuit can be modified to include nonlinear circuit elements in order to provide a more precise simulation of the molecular networks. For example, resonant tunneling diodes could be used to model the NDR behaviour observed in samples, diodes could be used for modelling observed rectification, and finally, transistors could be included for modelling the observed switching behaviour. Additionally, DFT-based calculations can be performed on molecular networks with benzenedithiol molecules and carbon-based building blocks, such as graphene nanoflakes. Figure 5.3 below shows examples of such molecular networks. The structures shown can be treated as unit cells which are repeated to build larger networks. Multi-terminal networks (e.g., the Y-shaped and diamond-shaped networks) made of benzenedithiol molecules and graphene nanoflakes are also worth investigating. The electronic and transport properties of these molecular networks could be interesting for future carbon-based nanoelectronics applications.

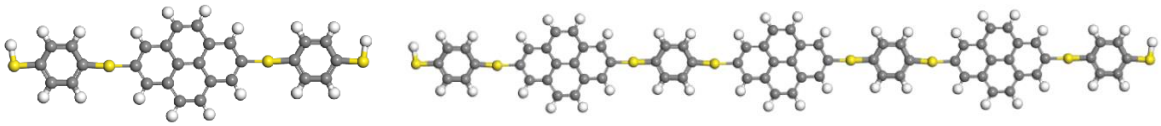

(a) (b)

Figure 5. 3 Graphene-BDT molecular networks (a) 1-unit graphene-BDT linear chain; (b) 3-unit graphene-BDT linear chain.

5.2.3 Device Applications

Understanding electron transport through molecules and molecular networks facilitates their application as basic circuit elements. Several molecules have demonstrated interesting electrical properties which could make them applicable as nanoscale electronic circuit elements. For example, several molecules [134], [135] have demonstrated potential use as resonant tunneling diodes (RTDs). In most cases, an RTD has two potential barriers and a quantum well, and electrons tunnel through the barriers when the kinetic energy of the incoming electrons aligns with the unoccupied energy levels. The nanoscale size requirements of these elements are met by many molecules/molecular networks.

Molecular capacitors are another interesting application of molecules as electronic circuit elements. It has been demonstrated that certain molecules, such as porphyrins, can store electric charge when powered by a bias voltage [136].

Molecular wires are another important part of electronic circuits, which are essential for the interconnection of various electronic components over a substrate. Both saturated chain and conjugated chain molecules can serve as molecular wires, with conjugated molecules being preferred because they are efficient for the long-range transport of electrons [137].

The use of molecules and molecular networks as basic components in circuits provides new pathways for fabricating novel devices with tailorable functionalities. Consequently,

the self-assembled gold nanoparticle molecular networks studied in this work could find applications in several types of nanoscale devices, for computing, memory, switching, sensing, and logic purposes.

Several experiments involving gated molecules have demonstrated gate modulation of the *I-V* characteristics, which indicates the possibility of using molecules as electronic transistors [16], [34]. By extending this idea, transistor arrays made using carbon nanotubes have been demonstrated for logic applications [138]. The metal-molecular networks studied in this work could be combined with CNTs to bridge the pre-formed source/drain electrodes in the complementary logic devices, since they displayed switching behaviour.

Another type of application for our self-assembled metal-molecular networks is in nano-floating gate transistor memory (NFGTM) devices. Transistor-type memory devices are advantageous over resistor- and capacitor-type devices because of their mechanism of operation: the gate field and channel conductance are modulated by the stored charges either in a charge trapping or ferroelectric layer, thereby introducing reversible shifts in the threshold voltage of the device. In these devices, charge carriers can be trapped and released from the charge trapping sites to achieve programming and erasing operations [139], [140].

Graphene NFGTM devices using gate dielectrics embedded with nanometer-sized metallic or semiconducting nanoparticles are considered as promising candidates for realizing nonvolatile memories. In these devices, the levels and sites of charge trapping can be controlled precisely by varying the nanoparticle species, sizes, and density [139]. Our metal-molecular networks are also excellent candidates for these devices due to the

tunability of the molecule: gold nanoparticle ratios and possible charge trapping behaviour observed in the networks at certain biases [67].

Figure 5.4 below shows a schematic illustrating the method of fabrication of the NFGTM arrays as well as a photograph of the graphene NFGTM array [139].

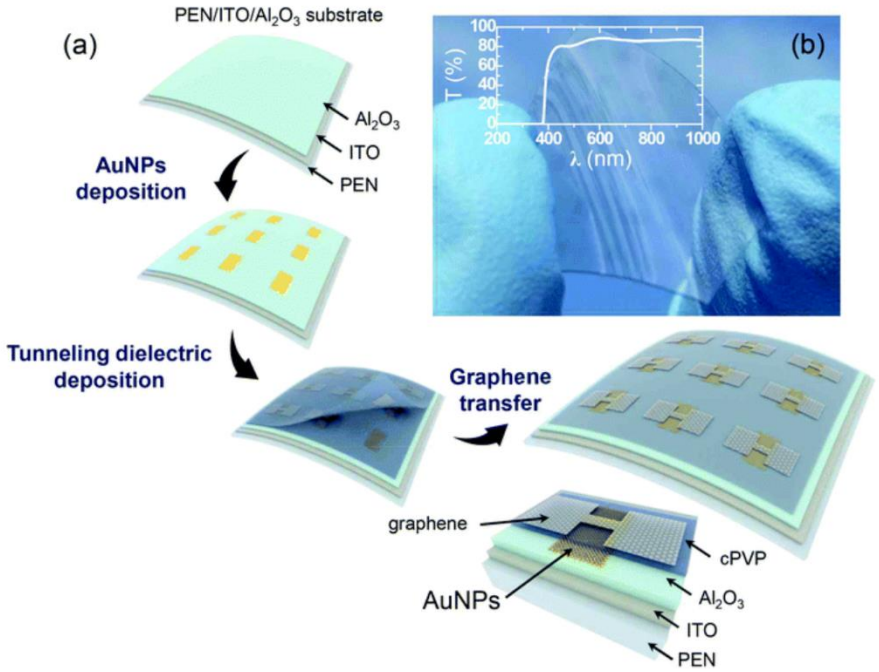

Figure 5. 4 (a) A schematic diagram showing the fabrication of a transparent and flexible graphene nano-floating gate transistor memory (NFGTM) on a flexible plastic substrate; (b) A photograph of the graphene NFGTM array. The inset shows the optical transmittance of a NFGTM array on a substrate (adapted from Ref. 139).

Finally, the metal-molecular networks studied in this work could be used as biosensors. Since the electrical and optical behaviour of the molecular networks have been extensively characterized, any factors which could affect those properties could be effectively monitored. Also, gold nanoparticles have large surface areas which are beneficial for the

immobilization of biological molecules. Biosensors based on thiol SAM-modified gold surfaces/nanoparticles have been successfully demonstrated [141], [142].

Bibliography

[1] C. P. Poole and F. J. Owens, Introduction to nanotechnology, Hoboken, NJ: J. Wiley, 2003.

[2] 1.-1. Boyle and E. E. B. O. E. Collection, *The [s]ceptical chymist, or, Chymico-physical doubts & paradoxes: touching the spagyrist's principles commonly call'd hypostatical, [a]s they are wont to be propos'd and defended by the generality of alchymists : whereunto is præmis'd part of another discourse relating to the same subject,* vol. 1609:14., 1661.

[3] M. Faraday, "The Bakerian Lecture: Experimental Relations of Gold (and Other Metals) to Light," *Philosophical transactions of the Royal Society of London,* vol. 147, pp. 145-181, 1857.

[4] R. P. Feynman, "There's plenty of room at the bottom [data storage]," *Journal of microelectromechanical systems,* vol. 1, pp. 60-66, 1992.

[5] W. F. Brinkman, D. E. Haggan and W. W. Troutman, "A history of the invention of the transistor and where it will lead us," *IEEE journal of solid-state circuits,* vol. 32, pp. 1858-1865, 1997.

[6] C.-T. Sah, "Evolution of the MOS transistor-from conception to VLSI," *Proceedings of the IEEE,* vol. 76, pp. 1280-1326, 1988.

[7] K. Mistry, C. Allen, C. Auth, B. Beattie, D. Bergstrom, M. Bost, M. Brazier, M. Buehler, A. Cappellani, R. Chau, C.-H. Choi, G. Ding, K. Fischer, T. Ghani, R. Grover, W. Han, D. Hanken, M. Hattendorf, J. He, J. Hicks, R. Huessner, D. Ingerly, P. Jain, R. James, L. Jong, S. Joshi, C. Kenyon, K. Kuhn, K. Lee, H. Liu, J. Maiz, B. McIntyre, P. Moon, J. Neirynck, S. Pae, C. Parker, D. Parsons, C. Prasad, L. Pipes, M. Prince, P. Ranade, T. Reynolds, J. Sandford, L. Shifren, J. Sebastian, J. Seiple, D. Simon, S. Sivakumar, P. Smith, C. Thomas, T. Troeger, P. Vandervoorn, S. Williams and K. Zawadzki, "A 45nm Logic Technology with High-k+Metal Gate Transistors, Strained Silicon, 9 Cu Interconnect Layers, 193nm Dry Patterning, and 100% Pb-free Packaging," in *2007 IEEE International Electron Devices Meeting,* 2007.

[8] N. Xu, B. Ho, F. Andrieu, L. Smith, B.-Y. Nguyen, O. Weber, T. Poiroux, O. Faynot and T.-J. K. Liu, "Carrier-Mobility Enhancement via Strain Engineering in Future Thin-Body MOSFETs," *IEEE electron device letters,* vol. 33, pp. 318-320, 2012.

[9] C. .. Jan, U. Bhattacharya, R. Brain, S. .. Choi, G. Curello, G. Gupta, W. Hafez, M. Jang, M. Kang, K. Komeyli, T. Leo, N. Nidhi, L. Pan, J. Park, K. Phoa, A. Rahman, C. Staus, H. Tashiro, C. Tsai, P. Vandervoorn, L. Yang, J. .. Yeh and P. Bai, "A 22nm SoC platform technology featuring 3-D tri-gate and high-k/metal gate, optimized for ultra low power, high performance and high density SoC applications," 2012.

[10] S. E. Thompson and S. Parthasarathy, "Moore's law: the future of Si microelectronics," *Materials today (Kidlington, England),* vol. 9, pp. 20-25, 2006.

[11] J. Wu, Y.-L. Shen, K. Reinhardt, H. Szu and B. Dong, "A Nanotechnology Enhancement to Moore's Law," *Applied computational intelligence and soft computing,* vol. 2013, pp. 1-13, 2013.

[12] P. Gargini, "The International Technology Roadmap for Semiconductors (ITRS): "Past, present and future"," 2000.

[13] "International Roadmap for Devices and Systems," *IEEE,* 2020.

[14] R. Busi, Swapna, K. Babu and Y. Rao, "Carbon Nanotubes Field Effect Transistors : A Review 1".

[15] W. Lu, P. Xie and C. M. Lieber, "Nanowire Transistor Performance Limits and Applications," *IEEE transactions on electron devices,* vol. 55, pp. 2859-2876, 2008.

[16] C. Dekker, S. J. Tans and A. R. M. Verschueren, "Room-temperature transistor based on a single carbon nanotube," *Nature (London),* vol. 393, pp. 49-52, 1998.

[17] Y.-H. Jeong and D. M. Kim, Nanowire field effect transistors: principles and applications, 2014 ed., D. M. Kim and Y. Jeong, Eds., New York: Springer, 2014;2013;.

[18] M. Fu, D. Pan, Y. Yang, T. Shi, Z. Zhang, J. Zhao, H. Q. Xu and Q. Chen, "Electrical characteristics of field-effect transistors based on indium arsenide nanowire thinner than 10 nm," *Applied physics letters,* vol. 105, p. 143101, 2014.

[19] A. Peschot, C. Qian and T.-J. K. Liu, "Nanoelectromechanical Switches for Low-Power Digital Computing," *Micromachines (Basel),* vol. 6, pp. 1046-1065, 2015.

[20] J. E. Jang, S. N. Cha, Y. Choi, G. A. J. Amaratunga, D. J. Kang, D. G. Hasko, J. E. Jung and J. M. Kim, "Nanoelectromechanical switches with vertically aligned carbon nanotubes," *Applied physics letters,* vol. 87, pp. 163114-163114-3, 2005.

[21] W. Lu and C. M. Lieber, "Nanoelectronics from the bottom up," *Nature materials,* vol. 6, pp. 841-850, 2007.

[22] D. Goldhaber-Gordon, M. S. Montemerlo, J. C. Love, G. J. Opiteck and J. C. Ellenbogen, "Overview of nanoelectronic devices," *Proceedings of the IEEE,* vol. 85, pp. 521-540, 1997.

[23] M. Z. Ahsan, "Single Electron Transistor (SET): Operation and Application Perspectives," August 2016.

[24] K. S. Makarenko, Z. Liu, M. P. de Jong, F. A. Zwanenburg, J. Huskens and W. G. van der Wiel, "Bottom-Up Single-Electron Transistors," *Advanced materials (Weinheim),* vol. 29, pp. 1702920-n/a, 2017.

[25] J. C. Cuevas and E. Scheer, Molecular electronics: an introduction to theory and experiment, vol. 1;1.;, Hackensack, NJ;Singapore;: World Scientific, 2010.

[26] M. A. N. N. B. and K. U. H. N. H., "TUNNELING THROUGH FATTY ACID SALT MONOLAYERS," *Journal of applied physics,* vol. 42, pp. 4398-4405, 1971.

[27] A. Aviram and M. A. Ratner, "Molecular rectifiers," *Chemical physics letters,* vol. 29, pp. 277-283, 1974.

[28] A. S. MARTIN, SAMBLES and G. J. ASHWELL, "MOLECULAR RECTIFIER," *Physical review letters,* vol. 70, pp. 218-221, 1993.

[29] B. Capozzi, J. Xia, O. Adak, E. J. Dell, Z.-F. Liu, J. C. Taylor, J. B. Neaton, L. M. Campos and L. Venkataraman, "Single-molecule diodes with high rectification ratios through environmental control," *Nature nanotechnology,* vol. 10, pp. 522-U101, 2015.

[30] M. Sano and H. Taube, "Molecular hysteresis," *Journal of the American Chemical Society,* vol. 113, pp. 2327-2328, 1991.

[31] F. L. Carter, "The molecular device computer: Point of departure for large scale cellular automata," *Physica. D,* vol. 10, pp. 175-194, 1984.

[32] Y. Chen, G.-Y. Jung, D. A. A. Ohlberg, X. Li, D. R. Stewart, J. O. Jeppesen, K. A. Nielsen, J. F. Stoddart and R. S. Williams, "Nanoscale molecular-switch crossbar circuits," *Nanotechnology,* vol. 14, pp. 462-468, 2003.

[33] A. R. Champagne, A. N. Pasupathy and D. C. Ralph, "Mechanically Adjustable and Electrically Gated Single-Molecule Transistors," *Nano letters,* vol. 5, pp. 305-308, 2005;2004;.

[34] H. Song, Y. Kim, Y. Kim, Y. H. Jang, H. Jeong, M. A. Reed and T. Lee, "Observation of molecular orbital gating," *Nature,* vol. 462, p. 1039—1043, December 2009.

[35] H. Takahashi, N. Ikematsu, Y. Hattori and M. Kitamura, "Formation of a monolayer on a gold surface with high thermal stability using benzenedithiol," *Japanese Journal of Applied Physics,* vol. 59, p. SDDA03, 2019;2020;.

[36] V. Ganesh, S. K. Pal, S. Kumar and V. Lakshminarayanan, "Self-assembled monolayers (SAMs) of alkoxycyanobiphenyl thiols on gold—A study of electron transfer reaction using cyclic voltammetry and electrochemical impedance spectroscopy," *Journal of colloid and interface science,* vol. 296, pp. 195-203, 2006.

[37] P. Maksymovych, O. Voznyy, D. B. Dougherty, D. C. Sorescu, J. T. Yates, T. (. S. Oak Ridge National Lab. (ORNL) and P. (. S. National Energy Technology Lab. (NETL), "Gold adatom as a key structural component in self-assembled monolayers of organosulfur molecules on Au(1 1 1)," *Progress in surface science,* vol. 85, pp. 206-240, 2010.

[38] A. Ulman, "Formation and Structure of Self-Assembled Monolayers," *Chemical reviews,* vol. 96, pp. 1533-1554, 1996.

[39] M. Singh, N. Kaur and E. Comini, "The role of self-assembled monolayers in electronic devices," *Journal of materials chemistry. C, Materials for optical and electronic devices,* vol. 8, pp. 3938-3955, 2020.

[40] A. Galal, N. F. Atta and E. H. El-Ads, "Probing cysteine self-assembled monolayers over gold nanoparticles – Towards selective electrochemical sensors," *Talanta (Oxford),* vol. 93, pp. 264-273, 2012.

[41] V. Santhanam, J. Liu, R. Agarwal and R. P. Andres, "Self-Assembly of Uniform Monolayer Arrays of Nanoparticles," *Langmuir,* vol. 19, pp. 7881-7887, 2003.

[42] S. E. Herrera, F. G. Davia, F. J. Williams and E. J. Calvo, "Metal Nanoparticle Enhancement of Electron Transfer to Tethered Redox Centers through Self-Assembled Molecular Films," *Langmuir,* vol. 35, pp. 6297-6303, 2019.

[43] V. Y. Kutsenko, Y. Y. Lopatina, L. Bossard-Giannesini, O. A. Marchenko, O. Pluchery and S. V. Snegir, "Alkylthiol self-assembled monolayers on Au(111) with tailored tail groups for attaching gold nanoparticles," *Nanotechnology,* vol. 28, pp. 235603-235603, 2017.

[44] S. Nayak, N. Horst, H. Zhang, W. Wang, S. Mallapragada, A. Travesset, D. Vaknin and I. (. S. A. P. S. (. Argonne National Lab. (ANL), "Ordered Networks of Gold Nanoparticles Crosslinked by Dithiol-Oligomers," *Particle & particle systems characterization,* vol. 35, pp. 1800097-n/a, 2018.

[45] A. Hofmann, P. Schmiel, B. Stein and C. Graf, "Controlled Formation of Gold Nanoparticle Dimers Using Multivalent Thiol Ligands," *Langmuir,* vol. 27, pp. 15165-15175, 2011.

[46] M. Ratner, "A brief history of molecular electronics," *Nature nanotechnology,* vol. 8, pp. 378-381, 2013.

[47] D. Stiévenard, "Scanning Tunneling Microscopy," in *Nanoscience: Nanotechnologies and Nanophysics*, C. Dupas, P. Houdy and M. Lahmani, Eds., Berlin, Heidelberg: Springer Berlin Heidelberg, 2007, p. 69–89.

[48] M. C. Petty, Molecular electronics: from principles to practice, Chichester, England;Hoboken, NJ;: John Wiley & Sons, 2007;2008;.

[49] E. Lörtscher, J. W. Ciszek, J. Tour and H. Riel, "Reversible and Controllable Switching of a Single-Molecule Junction," *Small (Weinheim an der Bergstrasse, Germany),* vol. 2, pp. 973-977, 2006.

[50] S. H. M. Jafri, H. Lofas, T. Blom, A. Wallner, A. Grigoriev, R. Ahuja, H. Ottosson and K. Leifer, "Nano-fabrication of molecular electronic junctions by targeted modification of metal-molecule bonds," *Scientific reports,* vol. 5, pp. 14431-14431, 2015.

[51] T. W. Kelley, E. Granstrom and C. D. Frisbie, "Conducting Probe Atomic Force Microscopy: A Characterization Tool for Molecular Electronics," *Advanced materials (Weinheim),* vol. 11, pp. 261-264, 1999.

[52] C. Kergueris, J. P. Bourgoin, S. Palacin, D. Esteve, C. Urbina, M. Magoga and C. Joachim, "Electron transport through a metal-molecule-metal junction," *Physical review. B, Condensed matter and materials physics,* vol. 59, pp. 12505-12513, 1999.

[53] S. Piccinin, "Theoretical modeling of electronic transport in molecular devices," 2006.

[54] S. Rahmanian Koshkaki, "An overview of Density-Functional-Theory (DFT) for students," December 2015.

[55] M. Smeu, R. A. Wolkow and G. A. DiLabio, "Theoretical investigation of electron transport modulation through benzenedithiol by substituent groups," *The Journal of chemical physics,* vol. 129, pp. 034707-034707-8, 2008.

[56] Y. Komoto, S. Fujii, H. Nakamura, T. Tada, T. Nishino and M. Kiguchi, "Resolving metal-molecule interfaces at single-molecule junctions," *Scientific reports,* vol. 6, pp. 26606-26606, 2016.

[57] D. Q. Andrews, R. Cohen, R. P. Van Duyne and M. A. Ratner, "Single molecule electron transport junctions: Charging and geometric effects on conductance," *The Journal of chemical physics,* vol. 125, pp. 174718-174718, 2006.

[58] M. D. Ganji and F. Nourozi, "Density functional non-equilibrium Green's function (DFT-NEGF) study of the smallest nano-molecular switch," *Physica. E, Low-dimensional systems & nanostructures,* vol. 40, pp. 2606-2613, 2008.

[59] R.-W. Yan, X. Jin, S.-Y. Guan, X.-G. Zhang, R. Pang, Z.-Q. Tian, D.-Y. Wu and B.-W. Mao, "Theoretical Study of Quantum Conductance of Conjugated and Nonconjugated Molecular Wire Junctions," *Journal of physical chemistry. C,* vol. 120, pp. 11820-11830, 2016.

[60] W. Y. Wang, T. Lee and M. A. Reed, "Mechanism of electron conduction in self-assembled alkanethiol monolayer devices," *Physical review. B,* vol. 68, 2003.

[61] D. P. Wang, D. E. Feldman, B. R. Perkins, A. J. Yin, G. H. Wang, J. M. Xu and A. Zaslavsky, "Hopping conduction in disordered carbon nanotubes," *Solid state communications,* vol. 142, pp. 287-291, 2007;2006;.

[62] X. Zhang, L. Yang and H. Liu, "High-temperature conduction behavior of carbon nanotube fiber from 25 °C to 1100 °C," *Applied physics letters,* vol. 112, p. 164103, 2018.

[63] W.-T. Hwang, Y. Jang, M. Song, D. Xiang and T. Lee, "Large-area molecular monolayer-based electronic junctions with transferred top electrodes," *Japanese Journal of Applied Physics,* vol. 59, p. SD0803, 2020.

[64] T.-W. Kim, G. Wang, H. Song, N.-J. Choi, H. Lee and T. Lee, "Charge Transport of Alkanethiol Self-Assembled Monolayers in Micro-Via Hole Devices," *Journal of Nanoscience and Nanotechnology,* vol. 6, pp. 3487-3490, November 2006.

[65] A. Wan, C. S. Suchand Sangeeth, L. Wang, L. Yuan, L. Jiang and C. A. Nijhuis, "Arrays of high quality SAM-based junctions and their application in molecular diode based logic," *Nanoscale,* vol. 7, pp. 19547-19556, 2015.

[66] C. Li, I. Pobelov, T. Wandlowski, A. Bagrets, A. Arnold and F. Evers, "Charge Transport in Single Au | Alkanedithiol | Au Junctions: Coordination Geometries and Conformational Degrees of Freedom," *Journal of the American Chemical Society,* vol. 130, pp. 318-326, 2008.

[67] A. Venkataraman, E. V. Amadi, T. S. M. Zaborniak, P. Zhang and C. Papadopoulos, "Negative Differential Resistance and Hysteresis in Self-Assembled Nanoscale Networks with Tunable Molecule-to-Nanoparticle Ratios," *physica status solidi (b),* vol. 257, p. 2000019, 2020.

[68] E. Amadi, V. Anusha, T. Zaborniak and C. Papadopoulos, "Nanoelectronic circuit elements based on metal-molecular networks," in *ACS Spring Meeting 2021*, 2021.

[69] A. Venkataraman, E. Amadi, P. Zhang and C. Papadopoulos, "Random key generation using self-assembled nanoparticle-molecular networks," in *ACS Spring Meeting 2021*, 2021.

[70] E. V. Amadi, A. Venkataraman, T. S. M. Zaborniak and C. Papadopoulos, "Nanoelectronic Circuit Elements Based on Nanoscale Metal-Molecular Networks," *Journal of Computational Electronics,* 2021.

[71] A. Venkataraman, E. V. Amadi and C. Papadopoulos, "Hardware security using self-assembled nanoelectronic networks," *Small,* 2021.

[72] A. Venkataraman, E. V. Amadi, Y. Chen and C. Papadopoulos, "Carbon Nanotube Assembly and Integration for Applications," *Nanoscale research letters,* vol. 14, pp. 220-220, 2019.

[73] A. Venkataraman, E. V. Amadi and C. Papadopoulos, "Nanoscale self-assembly : concepts, applications, and challenges," *IOP Publishing,* 2021.

[74] C. S. Weisbecker, M. V. Merritt and G. M. Whitesides, "Molecular Self-Assembly of Aliphatic Thiols on Gold Colloids," *Langmuir,* vol. 12, pp. 3763-3772, 1996.

[75] I. Khivrich, T. Dadosh, D. Mahalu, V. Frydman, J. Sperling, Y. Gordin, R. Krahne, I. Bar-Joseph and A. Yacoby, "Measurement of the conductance of single conjugated molecules," *Nature,* vol. 436, pp. 677-680, 2005.

[76] P. Zhang, A. Venkataraman and C. Papadopoulos, "Self-assembled gold nanoparticle–molecular electronic networks," *physica status solidi (b),* vol. 254, p. 1700061, 2017.

[77] S. W. Joo, S. W. Han and K. Kim, "Adsorption of 1,4-Benzenedithiol on Gold and Silver Surfaces: Surface-Enhanced Raman Scattering Study," *Journal of colloid and interface science,* vol. 240, pp. 391-399, 2001.

[78] J. K. Lim, Y. Kim, O. Kwon and S.-W. Joo, "Adsorption of 1,3-Benzenedithiol and 1,3-Benzenedimethanethiol on Gold Surfaces," *ChemPhysChem,* vol. 9, pp. 1781-1787, 2008.

[79] M. Sano, "Molecular hysteresis," *Advances in colloid and interface science,* Vols. 71-2, pp. 93-110, 1997.

[80] J. PALOHEIMO, P. KUIVALAINEN, H. STUBB, E. VUORIMAA and P. YLILAHTI, "MOLECULAR FIELD-EFFECT TRANSISTORS USING CONDUCTING POLYMER LANGMUIR-BLODGETT-FILMS," *Applied physics letters,* vol. 56, pp. 1157-1159, 1990.

[81] J. C. Jernigan, K. O. Wilbourn and R. W. Murray, "A benzimidazobenzophenanthroline polymer molecular transistor fabricated using club sandwich electrodes," *Journal of electroanalytical chemistry and interfacial electrochemistry,* vol. 222, pp. 193-200, 1987.

[82] H. Song, M. A. Reed and T. Lee, "Single-Molecule Devices: Single Molecule Electronic Devices (Adv. Mater. 14/2011)," *Advanced materials (Weinheim),* vol. 23, pp. 1576-1576, 2011.

[83] T. Zhang, D. Guérin, F. Alibart, D. Vuillaume, K. Lmimouni, S. Lenfant, A. Yassin, M. Oçafrain, P. Blanchard and J. Roncali, "Negative Differential Resistance, Memory, and Reconfigurable Logic Functions Based on Monolayer Devices Derived from Gold Nanoparticles Functionalized with Electropolymerizable TEDOT Units," *The Journal of Physical Chemistry C,* vol. 121, pp. 10131-10139, 2017.

[84] J. Zheng, J. Zhang, Z. Wang, L. Zhong, Y. Sun, Z. Liang, Y. Li, L. Jiang, X. Chen and L. Chi, "Programmable Negative Differential Resistance Effects Based on

Self-Assembled Au@PPy Core–Shell Nanoparticle Arrays," *Advanced Materials,* vol. 30, p. 1802731, 2018.

[85] J. G. Simmons, R. R. Verderber and N. F. Mott, "New conduction and reversible memory phenomena in thin insulating films," *Proceedings of the Royal Society of London. Series A. Mathematical and Physical Sciences,* vol. 301, pp. 77-102, 1967.

[86] N. Crivillers, M. Paradinas, M. Mas-Torrent, S. T. Bromley, C. Rovira, C. Ocal and J. Veciana, "Negative differential resistance (NDR) in similar molecules with distinct redox behaviour," *Chemical communications (Cambridge, England),* vol. 47, pp. 4664-4666, 2011.

[87] L. Bassham, A. Rukhin, J. Soto, J. Nechvatal, M. Smid, S. Leigh, M. Levenson, M. Vangel, N. Heckert and D. Banks, *A Statistical Test Suite for Random and Pseudorandom Number Generators for Cryptographic Applications,* Special Publication (NIST SP), National Institute of Standards and Technology, Gaithersburg, MD, 2010.

[88] Z. Hu, J. M. M. L. Comeras, H. Park, J. Tang, A. Afzali, G. S. Tulevski, J. B. Hannon, M. Liehr and S.-J. Han, "Physically unclonable cryptographic primitives using self-assembled carbon nanotubes," *Nature nanotechnology,* vol. 11, pp. 559-565, 2016.

[89] B. Waggener, "Pulse code modulation techniques : with applications in communications and data recording," 1995.

[90] E. Burzurí, D. Granados and E. M. Pérez, "Physically Unclonable Functions Based on Single-Walled Carbon Nanotubes: A Scalable and Inexpensive Method toward Unique Identifiers," *ACS Applied Nano Materials,* vol. 2, pp. 1796-1801, 2019.

[91] S. Luo, M. Song, X. Li, Y. Zhang, J. Hong, X. Yang, X. Zou, N. Xu and L. You, "Reconfigurable Skyrmion Logic Gates," *Nano Letters,* vol. 18, pp. 1180-1184, 2018.

[92] J.-C. Li and X. Gong, "Diode rectification and negative differential resistance of dipyrimidinyl–diphenyl molecular junctions," *Organic Electronics,* vol. 14, pp. 2451-2458, 2013.

[93] T. Hofer and S. Visser, "Editorial: Quantum Mechanical/Molecular Mechanical Approaches for the Investigation of Chemical Systems – Recent Developments and Advanced Applications," *Frontiers in Chemistry,* vol. 6, p. 357, September 2018.

[94] J. Licker, McGraw-Hill Concise Encyclopedia of Chemistry, McGraw-Hill, 2004.

[95] D. A. T. Gary L. Miessler, Inorganic Chemistry, Pearson Education International, 2013.

[96] R. J. Ouellette and J. D. Rawn, "1 - Structure and Bonding in Organic Compounds," in *Organic Chemistry*, R. J. Ouellette and J. D. Rawn, Eds., Boston, Elsevier, 2014, pp. 1-39.

[97] R. A. Latour, "3.14 Molecular Simulation Methods to Investigate Protein Adsorption Behavior at the Atomic Level☆," in *Comprehensive Biomaterials II*, P. Ducheyne, Ed., Oxford, Elsevier, 2017, pp. 268-294.

[98] K. Ohno, K. Esfarjani and Y. Kawazoe, "Ab Initio Methods," in *Computational Materials Science: From Ab Initio to Monte Carlo Methods*, Berlin, Heidelberg: Springer Berlin Heidelberg, 2018, p. 7–197.

[99] A. Szabo and N. S. Ostlund, Modern Quantum Chemistry: Introduction to Advanced Electronic Structure Theory, Dover Publications, New York, 1996.

[100] K. I. Ramachandran, G. Deepa, K. Namboori and S. E. Collection, Computational chemistry and molecular modeling: principles and applications, Berlin: Springer, 2008.

[101] J. M. Soler, E. Artacho, J. D. Gale, A. García, J. Junquera, P. Ordejón and D. Sánchez-Portal, "The SIESTA method for ab initio order-N materials simulation," *Journal of physics. Condensed matter*, vol. 14, pp. 2745-2779, 2002;2001;.

[102] K. Stokbro, J. Taylor, M. Brandbyge and H. Guo, "Ab-initio Non-Equilibrium Green's Function Formalism for Calculating Electron Transport in Molecular Devices," in *Introducing Molecular Electronics*, G. Cuniberti, K. Richter and G. Fagas, Eds., Berlin, Heidelberg: Springer Berlin Heidelberg, 2005, p. 117–151.

[103] K. U. R. T. STOKBRO, J. E. R. E. M. Y. TAYLOR, M. A. D. S. BRANDBYGE and P. A. B. L. O. ORDEJÓN, "TranSIESTA: A Spice for Molecular Electronics," *Annals of the New York Academy of Sciences*, vol. 1006, pp. 212-226, 2003.

[104] N. Papior, N. Lorente, T. Frederiksen, A. García and M. Brandbyge, "Improvements on non-equilibrium and transport Green function techniques: The next-generation transiesta," *Computer Physics Communications*, vol. 212, pp. 8-24, 2017.

[105] M. Tsutsui, M. Taniguchi and T. Kawai, "Local Heating in Metal−Molecule−Metal Junctions," *Nano letters*, vol. 8, pp. 3293-3297, 2008.

[106] Y. Kim, T. Pietsch, A. Erbe, W. Belzig and E. Scheer, "Benzenedithiol: A Broad-Range Single-Channel Molecular Conductor," *Nano letters*, vol. 11, pp. 3734-3738, 2011.

[107] Xiao, Xu and N. J. Tao, "Measurement of Single Molecule Conductance: Benzenedithiol and Benzenedimethanethiol," *Nano Letters*, vol. 4, pp. 267-271, 2004.

[108] A. Deka and R. C. Deka, "A density functional study on equilibrium geometries, stabilities and electronic properties of Au5Li binary clusters," *Applied nanoscience*, vol. 2, pp. 359-364, 2012.

[109] A. Deka and R. C. Deka, "Structural and electronic properties of stable Aun (n=2–13) clusters: A density functional study," *Journal of molecular structure. Theochem*, vol. 870, pp. 83-93, 2008.

[110] H. Qian, W. T. Eckenhoff, Y. Zhu, T. Pintauer and R. Jin, "Total Structure Determination of Thiolate-Protected Au38 Nanoparticles," *Journal of the American Chemical Society*, vol. 132, pp. 8280-8281, 2010.

[111] A. TLAHUICE and I. L. GARZON, "Structural, electronic, optical, and chiroptical properties of small thiolated gold clusters: the case of Au6 and Au8 cores protected with dimer [Au2(SR)3] and trimer [Au3(SR)4] motifs," *Physical chemistry chemical physics : PCCP*, vol. 14, pp. 7321-7329, 2012.

[112] W. A. N. G. Y. and J. P. PERDEW, "CORRELATION HOLE OF THE SPIN-POLARIZED ELECTRON-GAS, WITH EXACT SMALL-WAVE-VECTOR AND HIGH-DENSITY SCALING," *Physical review. B, Condensed matter and materials physics,* vol. 44, pp. 13298-13307, 1991.

[113] B. Delley, "From molecules to solids with the DMol3 approach," *The Journal of chemical physics,* vol. 113, pp. 7756-7764, 2000.

[114] E. Artacho, E. Anglada, O. Diéguez, J. D. Gale, A. García, J. Junquera, R. M. Martin, P. Ordejón, J. M. Pruneda, D. Sánchez-Portal and J. M. Soler, "The SIESTA method; developments and applicability," *Journal of physics. Condensed matter,* vol. 20, pp. 64208-64208, 2008.

[115] K. STOKBRO, J. TAYLOR, M. BRANDBYGE, J. .. MOZOS and P. ORDEJON, "Theoretical study of the nonlinear conductance of di-thiol benzene coupled to Au(111) surfaces via thiol and thiolate bonds," Amsterdam, 2003.

[116] A. Kokalj, "XCrySDen—a new program for displaying crystalline structures and electron densities," *Journal of molecular graphics & modelling,* vol. 17, pp. 176-179, 1999.

[117] N. TROULLIER and J. L. MARTINS, "EFFICIENT PSEUDOPOTENTIALS FOR PLANE-WAVE CALCULATIONS," *Physical review. B,* vol. 43, pp. 1993-2006, 1991.

[118] W. Kohn and L. J. Sham, "Self-Consistent Equations Including Exchange and Correlation Effects," *Physical review,* vol. 140, pp. A1133-A1138, 1965.

[119] J. P. Perdew, K. Burke and M. Ernzerhof, "Generalized gradient approximation made simple (vol 77, pg 3865, 1996)," *Physical review letters,* vol. 78, pp. 1396-1396, 1997.

[120] V. Diez-Cabanes, S. R. Gonzalez, S. Osella, D. Cornil, C. Dyck and J. Cornil, "Energy Level Alignment at Interfaces Between Au (111) and Thiolated Oligophenylenes of Increasing Chain Size: Theoretical Evidence of Pinning Effects," *Advanced theory and simulations,* vol. 1, pp. 1700020-n/a, 2018.

[121] A. Pramanik and P. Sarkar, "Theoretical studies on the carrier tunability of oxidized oligothiophenes," *Physical chemistry chemical physics : PCCP,* vol. 17, pp. 2673-2679, 2015.

[122] T. Tada and K. Yoshizawa, "Molecular design of electron transport with orbital rule: toward conductance-decay free molecular junctions," *Physical chemistry chemical physics : PCCP,* vol. 17, pp. 3299-3211, 2015.

[123] K. S. Thygesen, "Impact of exchange-correlation effects on the IV characteristics of a molecular junction," *Physical review letters,* vol. 100, pp. 166804-166804, 2008.

[124] H. Cheraghchi and K. Esfarjani, "Negative differential resistance in molecular junctions: Application to graphene ribbon junctions," *Physical review. B,* vol. 78, 2008.

[125] A. Venkataraman, P. Zhang and C. Papadopoulos, "Electronic transport in metal-molecular nanoelectronic networks: A density functional theory study," *AIP advances,* vol. 9, pp. 35122-035122-12, 2019.

[126] J. Fan, N. N. Gathitu, Y. Chang and J. Zhang, "Effect of length on the position of negative differential resistance and realization of multifunction in fused oligothiophenes based molecular device," *The Journal of chemical physics,* vol. 138, pp. 74307-74307, 2013.

[127] H. Wan, Y. Xu and G. Zhou, "Dual conductance, negative differential resistance, and rectifying behavior in a molecular device modulated by side groups," *The Journal of chemical physics,* vol. 136, pp. 184704-184704-6, 2012.

[128] J. Cornil, Y. Karzazi and J. L. Brédas, "Negative Differential Resistance in Phenylene Ethynylene Oligomers," *Journal of the American Chemical Society,* vol. 124, pp. 3516-3517, 2002.

[129] X. Shi, X. Zheng, Z. Dai, Y. Wang and Z. Zeng, "Changes of Coupling between the Electrodes and the Molecule under External Bias Bring Negative Differential Resistance," *The journal of physical chemistry. B,* vol. 109, pp. 3334-3339, 2005.

[130] M. SWEENY and X. U. JINGMING, "Resonant interband tunnel diodes," *Applied physics letters,* vol. 54, pp. 546-548, 1989.

[131] A. Z. Thong, M. S. P. Shaffer and A. P. Horsfield, "Rectification and negative differential resistance via orbital level pinning," *Scientific reports,* vol. 8, pp. 9120-8, 2018.

[132] D. M. Cardamone and G. Kirczenow, "Single-molecule device prototypes for protein-based nanoelectronics: Negative differential resistance and current rectification in oligopeptides," *Physical review. B,* vol. 77, 2008;2007;.

[133] E. Forsberg, "The Electron Waveguide Y-Branch Switch: A Review and Arguments for Its Use as a Base for Reversible Logic," in *Proceedings of the 2nd Conference on Computing Frontiers*, New York, NY, USA, 2005.

[134] J. Chen, M. A. Reed, A. M. Rawlett and J. M. Tour, "Large On-Off Ratios and Negative Differential Resistance in a Molecular Electronic Device," *Science,* vol. 286, p. 1550–1552, 1999.

[135] R. R. Pandey, N. Bruque, K. Alam and R. K. Lake, "Carbon nanotube - molecular resonant tunneling diode," *Physica status solidi. A, Applications and materials science,* vol. 203, pp. R5-R7, 2006.

[136] J. Lindsey and D. F. Bocian, "Molecules for charge-based information storage.," *Accounts of chemical research,* vol. 44 8, pp. 638-50, 2011.

[137] N. Tao, "Electron transport in molecular junctions," *Nature nanotechnology,* vol. 1, pp. 173-81, December 2006.

[138] A. Javey, Q. Wang, A. Ural, Y. Li and H. Dai, "Carbon Nanotube Transistor Arrays for Multistage Complementary Logic and Ring Oscillators," *Nano Letters,* vol. 2, pp. 929-932, 2002.

[139] S. Jang, E. Hwang and J. H. Cho, "Graphene nano-floating gate transistor memory on plastic," *Nanoscale,* vol. 6, no. 24, pp. 15286-15292, 2014.

[140] S.-J. Kim and J.-S. Lee, "Flexible Organic Transistor Memory Devices," *Nano Letters,* vol. 10, pp. 2884-2890, 2010.

[141] M. Frasconi, F. Mazzei and T. Ferri, "Protein immobilization at gold-thiol surfaces and potential for biosensing," *Analytical and bioanalytical chemistry,* vol. 398, pp. 1545-64, April 2010.

[142] S. Gaffar, R. Nurmalasari, Yohan and Y. W. Hartati, "Voltammetric DNA Biosensor using Gold Electrode Modified by Self Assembled Monolayer of Thiol for Detection of Mycobacterium Tuberculosis," *Procedia Technology,* vol. 27, pp. 74-80, 2017.

Appendix A

NIST test results for 27-bit keys.

Statistical Test / **Bit Stream (27 bits)**	Frequency	Block Frequency	Cumulative Sums test-Forward	Cumulative Sums test-Reverse	Runs	Serial test	Approximate Entropy
010101001010001010010101101	0.563703	0.964295	0.664066	0.968556	0.000731	0.004012	0.001396
010111001010001110010101101	0.847390	0.772760	0.999692	0.968556	0.081584	0.219036	0.208829
010101001101001010011101001	0.847390	0.964295	0.968556	0.999692	0.011990	0.042932	0.036278
010101101010101011010101101	0.563703	0.964295	0.968556	0.841231	0.000032	0.000240	0.000014
010111001010101011010101101	0.563703	0.772760	0.968556	0.841231	0.000731	0.004012	0.001396
011101001001001010010101001	0.563703	0.964295	0.841231	0.664066	0.009375	0.037020	0.023271
010101101010001011010001100	0.563703	0.964295	0.968556	0.841231	0.027219	0.188876	0.153850
010101001010101010010101101	0.847390	0.964295	0.968556	0.999692	0.000050	0.000279	0.000079
011111001111011110111011001	0.034264	0.275709	0.041843	0.041843	0.732462	0.090048	0.093776
011110001010011100010001101	0.847390	0.964295	0.968556	0.841231	0.841596	0.963640	0.962232
011010001010011100010010101	0.563703	0.964295	0.841231	0.841231	0.068964	0.188876	0.153850
111111011111011110111011001	0.003892	0.134686	0.004151	0.007785	0.353468	0.006257	0.011274
010101001010001010010101001	0.335924	0.964295	0.495894	0.664066	0.000354	0.002983	0.000154
010111001010001110010101101	0.847390	0.772760	0.999692	0.968556	0.081584	0.219036	0.208829
010101001101001010011101001	0.847390	0.964295	0.968556	0.999692	0.011990	0.042932	0.036278